TUNING OF ELECTRONIC STRUCTURE AND STEREOCHEMISTRY IN THE PYRIDINE AMIDE COMPLEXES OF MANGANESE(III), IRON(III), COBALT(III), AND COPPER(II)

A Thesis Submitted
In Partial Fulfilment of the Requirements
for the Degree of
DOCTOR OF PHILOSOPHY

by

MANABENDRA RAY

to the

DEPARTMENT OF CHEMISTRY
INDIAN INSTITUTE OF TECHNOLOGY KANPUR
SEPTEMBER, 1992

Dedicated to my
parents & sister

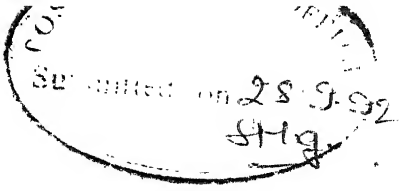

STATEMENT

I hereby declare that the matter embodied in this thesis is the result of investigations carried out by me in the Department of Chemistry, Indian Institute of Technology, Kanpur, India under the supervision of Dr. R. N. Mukherjee.

In keeping with the general practice of reporting scientific observations, due acknowledgements have been made wherever the work described is based on the findings of other investigators.

Manabendra Ray

Kanpur

September, 1992

DEPARTMENT OF CHEMISTRY
INDIAN INSTITUTE OF TECHNOLOGY, KANPUR
INDIA

CERTIFICATE - I

This is to certify that Mr. Manabendra Ray has satisfactorily completed all the courses required for the Ph.D. degree program.

These courses include:

CHM 605	Principles of Organic Chemistry
CHM 645	Principles of Inorganic Chemistry
CHM 625	Principles of Physical Chemistry
CHM 624	Modern Physical Methods in Chemistry
CHM 646	Bio Inorganic Chemistry
CHM 668	Advanced Inorganic Chemistry II
CHM 800	General Seminar
CHM 801	Special Seminar
CHM 900	Post-Graduate Research

Mr. Manabendra Ray successfully completed his Ph.D. qualifying examination in March 1990.

(S. S. Katiyar)
Head
Department of Chemistry
I.I.T. Kanpur

(Y. D. Vankar)
Convenor
Departmental Post Graduate
Committee
Department of Chemistry
I.I.T. Kanpur

CERTIFICATE - II

It is certified that the work contained in the thesis entitled " **Tuning of Electronic Structure and Stereochemistry in the Pyridine Amide Complexes of Manganese(III), Iron(III), Cobalt(III), and Copper(II)**", by **Mr. Manabendra Ray**, has been carried out under my supervision and that this work has not been submitted elsewhere for a degree.

R.N. Mukherjee

(Dr. R.N. Mukherjee)
Thesis Supervisor
Chemistry
I.I.T. Kanpur

September, 1992

ACKNOWLEDGEMENTS

I take this opportunity to place on record my deep sense of gratitude to my thesis supervisor, Dr. R. N. Mukherjee, for suggesting the research problem and for his guidance. It is his stimulating encouragement which kept me inspired throughout the course of this work. I am highly indebted to him for useful suggestions and criticisms during the work and for going through the entire manuscript.

I express my sincere thanks to the faculty members of this department, especially to Dr. P. K. Bharadwaj, Dr. S. Manogaran, Dr. J. Iqbal, Prof. S. Sarkar, Prof. P. K. Ghosh, Prof. S. Ranganathan, and Prof. N. Satyamurthy for their help and suggestions.

I like to thank my senior labmate Dr. K. Ramesh who helped me in the initial stages. Thanks are also due to Dr. N. Gupta, Mr. S. Mahapatra, and Dr. Z. Shirin for their help and co-operation in and outside the laboratory. I also like to thank Mr. T. K. Lal, Mr. S. Mukerjee, Mr. R. Ghose, Mr. A. K. Barik, and Ms. P. Das for their help in the various stages of my thesis work.

I wish to thank Prof. S. Mitra and Mr. B. T. Kansara, Chemical Physics Group, Tata Institute of Fundamental Research (TIFR), Bombay for their help in getting done all variable temperature magnetic susceptibility measurements. I am also thankful to Dr. A. K. Nigam and Mr. R. S. Sannabhadti (TIFR, Bombay) for Mössbauer measurements, and Dr. Raja Roy (CDRI, Lucknow) for 400 MHz ^{1}H NMR measurements. I would also like to thank Prof. R. M. Buchanan (University of Louisville, Kentucky,

USA) for solving the X-ray structure of one of our compounds.

I extend my sincere thanks to Mr. A. Bhabsar, Mr. Nayab Ahmed, Mr. D. K. Kannaujia and Mr. N. Jayaraman for helping me in recording NMR, EPR, and IR spectra. I thank Mr. Sairam and Mr. P.R. Subramanium for their kind cooperation in glass blowing.

I thank Mr. L. P. Tripathi, Mr. B.N. Shukla, Mr. V. Katiyar, and Mr. K. K. Bajpai of this department for all the help I got from them at different times. I also thank Mr. V. K. Gupta for tracing most of the figures.

I thank my friends Subrata, Indrani, Joykrishnada, Kapuri, Bhaskar, Samar, Dinu, Ravikant, Raghunathan, Pandian, Ramsharan, Bishma, Sanjay, Tarakeshwar, Kashi, Gagan, Ramaraj, and other friends in the department and in Hall IV (D block) who made my stay at IIT Kanpur, a most eventful one. I would also like to take this opportunity to thank Mrs. Mukherjee for making my stay here homely and lively.

I am inbebted to my parents, my aunt Ms. Niveditapuri Devi, Ms. Sandhya Saha, and my other family members who constantly encouraged me with their inspiration and support. I am grateful to my respected teachers Mr. Narayan Pal, Dr. Dilip K. Sarkar, Dr. Rajat K. Ghosh, Dr. Pinaki Bandyopadhyay, Dr. Parag S. Ray, Prof. Santosh K. Majumdar, and Dr. Ranjit K. Sarkar who have helped to develop however little scientific sense I have.

Manabendra Ray

SYNOPSIS

The thesis entitled "Tuning of Electronic Structure and Stereochemistry in the Pyridine Amide Complexes of Manganese(III), Iron(III), Cobalt(III), and Copper(II)", has been divided into five chapters.

Chapter 1 (Introduction) describes the known chelate chemistry utilizing deprotonated amide ligands. This chapter also describes the scope of the present work which stems from the following facts: (i) only a few reports have appeared in the literature on non-porphyrin Mn(III) complexes of tetradentate N_4 ligands and the effect of axial ligands in the stabilization of Mn(IV) state, (ii) spin-state regulation by axial ligands is a common feature in the case of heme-proteins as well as iron(III) complexes of synthetic porphyrins; moreover, spin-state change by axial ligands in the family of non-heme bleomycin-Fe(III) amide complexes is a fascinating phenomenon; examples of six-coordinate Fe(III) amide complexes of N_4 ligands with monodentate axial ligands are not known, (iii) thorough absorption spectral analysis to correlate the effect of axial ligand donor atom types on the spectral and redox behavior for the Co(III) complexes of the type $[Co(L)X_2]^{1-}$ (L= deprotonated dianionic bisamide ligand, X= monodentate uninegative axial ligands) is not available in the literature, (iv) tuning of electronic structural preferences in Cu(II) complexes via stereochemical consequences of ligand dispositions around Cu(II) center and its effect on electrochemical properties are important in order to ascertain the factors required in stabilizing Cu(I) and Cu(II) forms of copper proteins. Each of these problems has been dealt with in

subsequent chapters.

Chapter 2 describes the synthesis and characterization of high-spin manganese(III) complexes of the type [Mn(bpb)X] [X=Cl^-, N_3^-, or SCN^-; H_2(bpb) =1,2-bis(2-pyridinecarboxamido)benzene]. The complexes display in N,N-dimethylformamide (DMF) solutions ligand-to-metal charge-transfer transitions as well as ligand-field transitions. In DMF solution the complexes exhibit a quasi reversible Mn^{III}-Mn^{II} couple. The complexes [Mn(bpb)Cl] and [Mn(bpb)(N_3)] display an additional quasireversible Mn^{IV}-Mn^{III} couple which shows the systematic shift of formal potentials under the influence of axial ligands. The complex [Mn(bpb)N_3] and its ring methyl- and/or chloro- substituted derivatives exhibit well-resolved ^1H NMR spectra in d_6-DMSO solution. The ligand proton resonances are shifted from the usual diamagnetic region due to the presence of paramagnetic high-spin Mn(III) centre. A possible electron spin delocalization mechanism has been proposed.

Chapter 3 describes the syntheses and characterization of a novel family of six-coordinate iron(III) complexes using deprotonated bpb(2-) and bpc(2-) [H_2(bpc) = 4,5-dichloro-1,2-bis(2-pyridinecarboxamido) benzene] ligands. When the axial ligands are pyridine(C_5H_5N) or CN^- the resulting complexes are low-spin. However, when the axial ligands are Cl^- or $MeCO_2^-$ the complexes are high-spin. The spin-state properties of these complexes have been confirmed by temperature-dependent (40-300 K) magnetic susceptibility measurments as well as by Mössbauer spectral measurements. The EPR spectrum of low-spin [Fe(bpb)-

$(C_5H_5N)_2]ClO_4$ has been thoroughly analysed. Additionally, the complex $(Et_4N)[Fe(bpc)(O_2CMe)_2].CHCl_3$ has been structurally characterized by single crystal X-ray diffraction. The redox chemistry of the acetate and cyanide complexes reveals the enhanced stabilization of the iron(III) state by these deprotonated bis(picolinamide) ligands. The EPR spectra of chemically and electrochemically generated $1e^-$ oxidized species of the cyanide complex confirms that the oxidation is of primarily ligand oxidation origin.

In chapter 4, a series of diamagnetic cobalt(III) complexes of bpb(2-) and bpc(2-) ligands with axial ligands (Cl^-, N_3^-, SCN^-, NO_2^- or $MeCO_2^-$) has been synthesized. The trans-geometry of the complexes has been revealed by their ^1H NMR spectrum. The brown or green crystalline complexes display dominant ligand-to-metal charge-transfer transitions. In the low-energy region ligand field transitions are observed. From an analysis of the d-d transition(s) ligand field parameters of the in-plane and axial ligands have been determined. In acetonitrile solution the complexes exhibit an irreversible Co^{III}-Co^{II} couple and a quasireversible Co^{II}-Co^{I} couple. When X = NCS^-, the Co^{II}-Co^{I} couple is irreversible. These complexes display an additional quasireversible oxidative response of primarily ligand oxidation origin. When X = NO_2^- and SCN^-, this couple is irreversible. A linear spectroelectrochemical relationship has been obtained between the ligand field strength of the axial ligands and the cathodic peak potential for the Co^{III}-Co^{II} couple.

Chapter 5 describes the synthesis and properties of three copper(II) complexes [Cu(bpb).H_2O], [$Cu(pb)_2$.H_2O] and [$Cu(ptb)_2$.H_2O] [H(pb) = 2-pyridinecarboxamidobenzene; H(ptb)= 2-pyridinecarboxamido-2,4,5-trichlorobenzene]. The deprotonated ligands pb(2-) and ptb(2-) exert a measurable degree of geometric control of the coordination spheres for these copper(II) complexes. The EPR and absorption spectra of these complexes have been measured in order to elucidate the structure and nature of the bonding between the copper and the ligands. The positions of d-d absorption(s) of [$Cu(pb)_2$.H_2O] and [$Cu(ptb)_2$.H_2O] are consistent with a grossly pseudo-tetrahedral arrangement about the copper atoms. The dihedral angle for [$Cu(pb)_2$.H_2O] between the two chelate rings is estimated from EPR data to be ~ 55°. The redox thermodynamics of the complexes has been examined by cyclic voltammetry. With replacement of the tetradentate bpb(2-) ligand with the bidentate pb(2-) and ptb(2-) ligands of similar donor set, a marked positive shift (~ 0.6-0.7 V) was observed in the $E_{1/2}$ values. The electronic structural preferences in these copper(II) complexes have been examined using semi-empirical molecular orbital calculations at the extended Hückel level.

CONTENTS

CHAPTER 1

INTRODUCTION

1.1 Purpose of the Present Investigation

The primary concern of this thesis work is twofold. First, to synthesize a new class of selected transition metal complexes (only those metal ions are chosen which have well defined redox states) utilizing deprotonated bis(picolinamide) ligand and its various ring substituted derivatives, (1) as planar tetra-

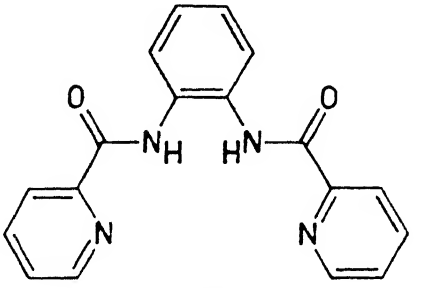

(1)

dentate N_4 open chain in-plane ligands. The ligation at the axial position(s) would be provided by monodentate neutral or uninegative ligands and thus would generate complexes of structural types trans-$[Mn^{III}N_4X]$, trans-$[Fe^{III}N_4X_2]^{1+/1-}$, and trans-$[Co^{III}N_4X_2]^{1-}$. Secondly, a rational study of the tuning of the electron density at the metal centers caused by changes in the axial ligands.

Another aspect which has also been considered in this thesis is the effect of ligand flexibility on the stereochemistry of a group of three copper(II) complexes using the ligands (1),(2a), and (2b).

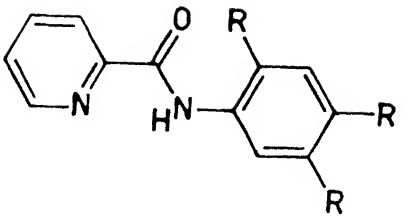

R = H, (2a)
R = Cl, (2b)

In what follows, we consider briefly the various aspects of metal-amide chemistry and summarize (Tables 1.1-1.4) the known chelate chemistry utilizing a wide variety of selected amide ligands.

1.2 General Considerations[1-5]

Amide bonds or groups provide the linkage between adjacent amino acid residues in proteins. When condensation of two amino acids yields a dipeptide, the resulting amide bond is often referred to as a peptide bond (or group).

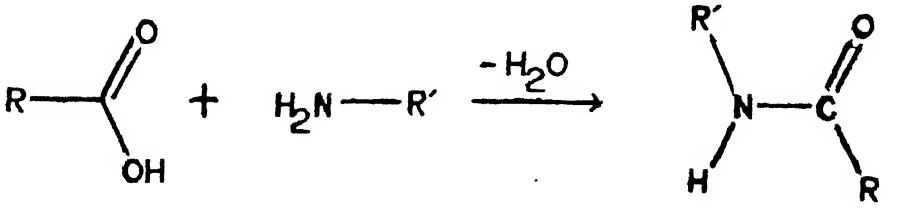

Greater appreciation of protein structure has increased interest in the metal ion binding capabilities of the amide group, so abundant in nature.

An amide group offers two potential binding atoms, the oxygen and nitrogen, for complexation of protons and metal ions. Scheme I summarizes the proton equilibria studies on amide unit.[1]

Table 1.1 : Selected Ligands and their Complexes Containing Amides from Amino Acid residues.

Ligand Types	Comments	References
Dipeptides		
(3)	Ni(III) complex with deprotonated ligand. Absorption spectra,EPR, and kinetic study.	6
Tripeptide		
(4) and other tripeptides	Ni(III) complex with deprotonated ligands. Absorption spectra, electrochemistry, EPR, kinetic study.	7
	Ni(III) complex with deprotonated ligands. Oxidation of I^-, kinetic study.	8
	X-ray structure of dimeric Cu(II) complex with glycylglycylglycine.	9
	Cu(III) complex with deprotonated ligands. Absorption spectra, EPR, electrochemistry, and electron transfer reaction kinetics with $Fe(CN)_6^{4-}$.	10
	Cu(III), Cu(II) complexes with deprotonated ligands. Variation of electrode potentials with number of deprotonated amides.	11
	Cu(II) complexes with deprotonated ligands. Ligand field strength of deprotonated amide.	12
Mixed Ligand		
(5)	Ni(III) complex with deprotonated ligand. Absorption spectra, EPR, electrochemistry, kinetic studies.	7
(6) and other related ligands.	Cu(III) and Ni(III) complexes with deprotonated ligands. Electrochemistry, EPR.	13

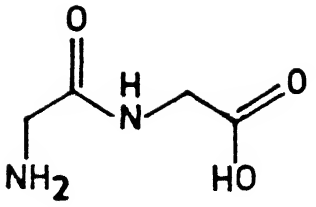
O
H
N
O
NH2
HO

(3)

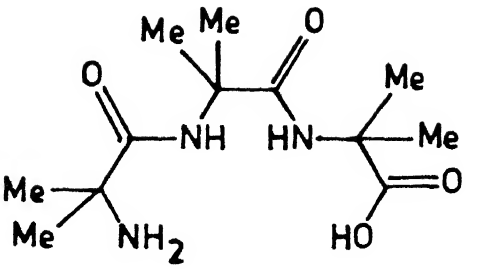
Me
Me
O
O
Me
NH
HN
Me
Me
O
Me
NH2
HO

(4)

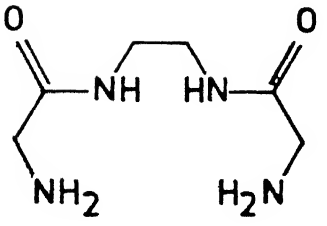
O
O
NH
HN
NH2
H2N

(5)

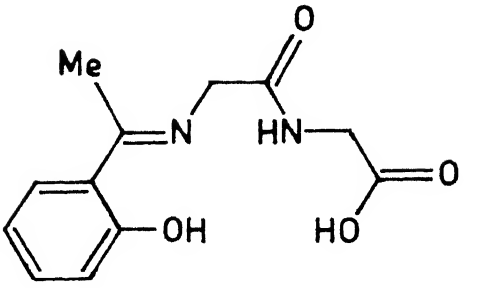
O
Me
N
HN
O
OH
HO

(6)

Table 1.2 : Selected Ligands and their Complexes Containing Amido-phenol and Amido-alkoxo unit.

Ligand Types	Comments	References
Tridentate		
(7a) and its ring-substituted derivatives	Ligand synthesis, Mn(IV), Mn(V) complexes with deprotonated ligand. Absorption spectra, EPR, electrochemistry, and magnetism.	14
(7b) & (7c)	Co(IV) complexes with deprotonated ligands.	15
	Cu(III) complexes with deprotonated ligands.	16
	Fe(IV),and Fe(V) complexes with deprotonated ligands. Absorption spectra, Mössbauer spectra, and electrochemistry.	17
Tetradentate		
(8a) & (8b)	Ligand synthesis,deprotonated Os(IV) complexes. X-ray structure, electrochemistry, ^{1}H,and ^{13}C NMR.	18
	Deprotonated Co(III), and Co(IV) complexes. X-ray structure, Absorption spectra, EPR, and electrochemistry.	19
	Deprotonated Os(IV) complexes, and its oxidative degradation product. X-ray structure, and ^{1}H NMR.	20
	Deprotonated Ru(IV) complex. X-ray structure, magnetism, and epoxidation catalytic activity.	21
	Deprotonated nitrido Os(VI) complex. X-ray structure.	22

Cont.

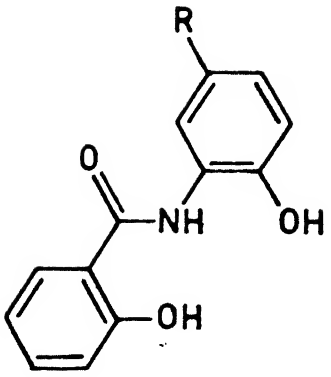

R = H , (7a)

= Me , (7b)

= Cl , (7c)

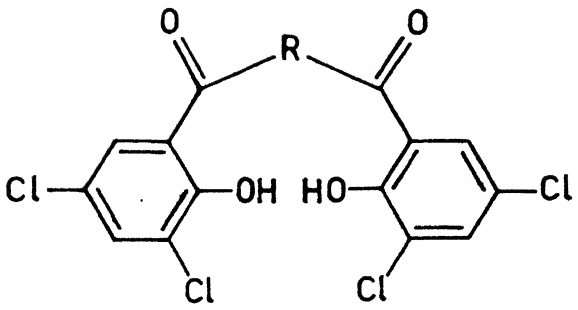

R = 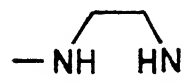 , (8a)

= 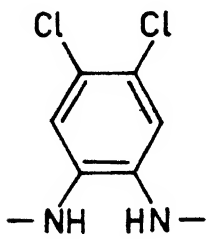 , (8b)

Ligand Types	Comments	References
(9)	Ligand synthesis, square planar, Cu(III), Co(III) complexes with deprotonated ligands. X-ray structure, ^{1}H NMR.	23-25
	Mn(III), oxo-Mn(V) complexes with deprotonated ligand. X-ray structure, ^{1}H NMR.	26
(10)	Ligand synthesis, square planar, Cu(III) complex with deprotonated ligand.	24,25
Hexadentate		
(11)	Ligand synthesis, Mn(IV) complex with deprotonated ligands. X-ray structure, EPR, electrochemistry, and magnetism.	27,28

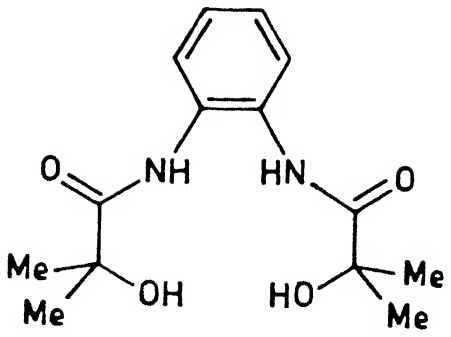
O
NH
HN
O
Me
OH
HO
Me
Me
Me

(9)

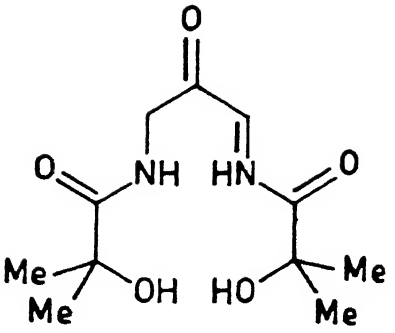
O
O
NH
HN
O
Me
OH
HO
Me
Me
Me

(10)

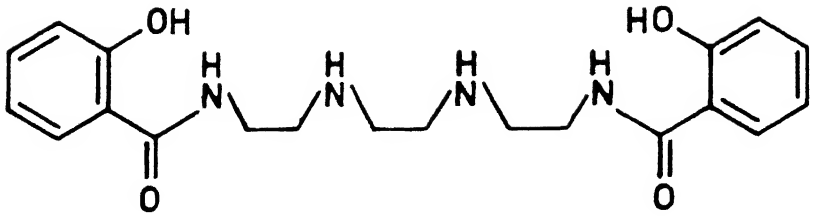
OH
HO
H
N
H
N
H
N
H
N
O
O

(11)

Table 1.3 : Selected Tetradentate Cyclic All Amide Ligands and their Complexes.

Ligand Types	Comments	References
(12)	Oxo-Cr(V) complex with deprotonated ligands. X-ray structure, IR, and EPR.	29
	Oxo-Mn(V) complex with deprotonated ligands. X-ray structure, IR, and ^{1}H NMR, electrochemistry, and resonance Raman.	30,31
	Ligand synthesis, Co(III) complex with deprotonated ligands, and its chemically oxidized product. X-ray structure,and EPR.	32
(13)	Co(III) high-spin complex with deprotonated ligands. X-ray structure, ^{1}H NMR.	33
	Oxo-chromium(V) complex with deprotonated ligand. X-ray structure, IR, EPR, and absorption spectra.	29
	Fe(IV) complex with deprotonated ligands. X-ray structure, Mössbauer, and electrochemistry.	34
(14)	Ligand synthesis, Cu(II), Cu(III) complexes with deprotonated ligand. EPR, electrochemistry, stability constant.	35,36

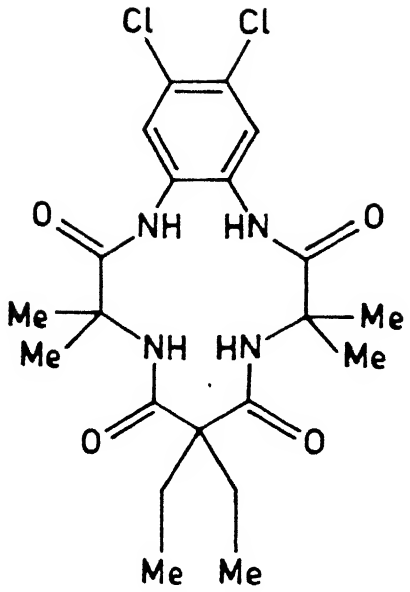
Cl
Cl
O
NH
HN
O
Me
Me
Me
Me
NH
HN
O
O
Me
Me

(12)

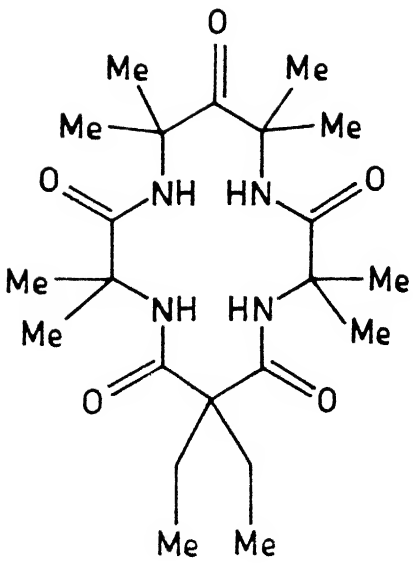
O
Me
Me
Me
Me
O
NH
HN
O
Me
Me
NH
HN
Me
Me
O
O
Me
Me

(13)

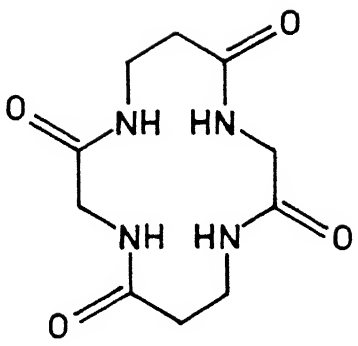
O
O
NH
HN
NH
HN
O
O

(14)

Table 1.4 : Selected Ligands and their Complexes with Pyridine-carboxamide unit.

Ligand Types	Comments	References
Bidentate		
(15a)	Ligand synthesis, Ni(II) & Cu(II) complexes with protonated and deprotonated ligand. IR, absorption spectra, and magnetism.	37
	X-ray structure of ligand.	38
	X-ray structure of Ni(II) complexes with protonated and deprotonated ligand.	39,40
(15b)	Ligand synthesis, Co(II), Ni(II) & Cu(II) complexes with protonated ligand. Pd(II) and Cu(II) complexes with deprotonated ligand. IR, absorption spectra, and magnetism.	41
Tridentate		
(16a)	Ligand synthesis, Co(III), Cu(II), and Ni(II) complexes with protonated as well as deprotonated ligand. Absorption spectra, and magnetism.	42-45
(16b)	Ligand synthesis, Co(III), Cu(II), and Ni(II) complexes with protonated as well as deprotonated ligand. Absorption spectra, and magnetism.	42-45
(17)	Ligand synthesis, Cu(II) complex with deprotonated ligand. Absorption spectra.	46
(18a) & (18b)	Ligand synthesis, Cu(II) complex with deprotonated ligand. X-ray structure, absorption spectra, EPR, and electrochemistry. Metal- bleomycin interaction modeling.	47

Cont.

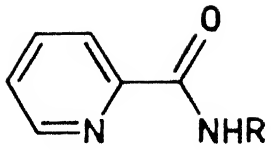

R = H, (15a)
= Me, (15b)

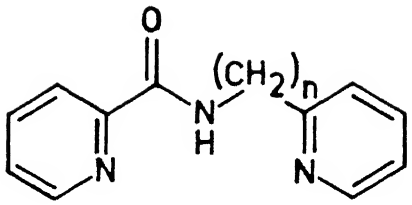

n = 1, (16a)
= 2, (16b)

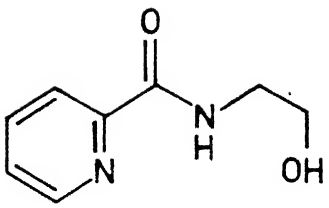

(17)

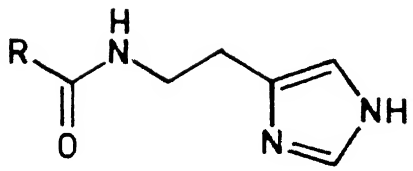

R = 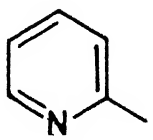 , (18a)

= 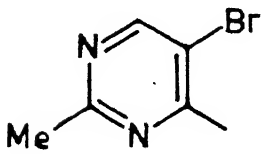 , (18b)

Ligand Types	Comments	References
	Low-spin Fe(III) complex with deprotonated ligand. X-ray structure, absorption spectra, electrochemistry, ^{1}H NMR, EPR, Mössbauer spectra, and magnetism. Metal- bleomycin interaction modeling.	48
	Co(III) complex with deprotonated ligand. X-ray structure, absorption spectra, electrochemistry, ^{1}H, and ^{13}C NMR. Metal- bleomycin interaction modeling.	49
Tetradentate		
(19a) and its phenyl substituted derivative **(19b)**	Ligand synthesis, VO^{2+} complexes with deprotonated ligands. X-ray structure, IR, electrochemistry, EPR, and magnetism.	50,51
(20a)	Ligand Syntheses, ^{1}H NMR.	52
and its various bridge substituted derivatives **(20b)** to **(20d)***	Mn(II), Co(II), Cu(II), Ni(II), Zn(II), Pd(II) complexes with protonated as well as deprotonated ligands. IR, diffuse reflectance spectra, and magnetism.	53,54
	X-ray structure of Ni(II) complex with deprotonated ligand.	55
	X-ray structure of Cu(II) complex with deprotonated ligand with.	56

* The Ligands **(1)** and **(20d)** are identical.

Cont.

Ligand Types	Comments	References
	Os(III), di-oxo Os(VI) complexes with deprotonated ligand. X-ray structure, and electrochemistry.	57
	Mn(III) complexes with deprotonated ligands. IR, magnetism, and epoxidation catalytic activity.	58
	Nitrido-Cr(V), and Cr(III) complexes with deprotonated ligand. X-ray structure, absorption spectra, and electrochemistry.	59
	Rh(III), Ir(III) complexes with deprotonated ligands. X-ray structure, absorption spectra electrochemistry, and ^{1}H NMR.	60
	Cr(III), Mn(III) complexes with deprotonated ligands X-ray structure, absorption spectra electrochemistry of Cr(III) complexes.	61
	Co(III) complexes with deprotonated ligands. X-ray structure, absorption spectra electrochemistry, and ^{1}H NMR.	62
	Os(V), Os(IV), Os(III) complexes with deprotonated ligands. X-ray structure, absorption spectra electrochemistry.	63
Pentadentate		
(21a) and its substituted derivatives (21b) & (21c)	Cu(II), Fe(II), and Fe(III) complexes with protonated ligands. Deprotonation occurs on pH change. EPR, electrochemistry.	64
(22)	Ligand synthesis, Cu(II) complex with deprotonated ligand. X-ray structure, absorption spectra, EPR, electrochemistry, and DNA cleavage experiments. Bleomycin modeling.	65.66

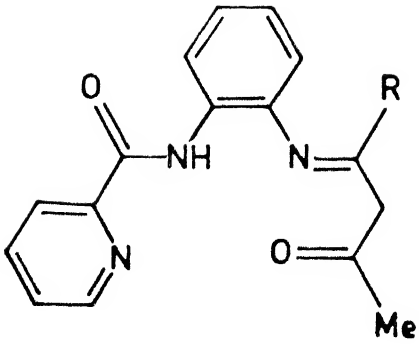

R = Me , (19a)

= C_6H_5 , (19b)

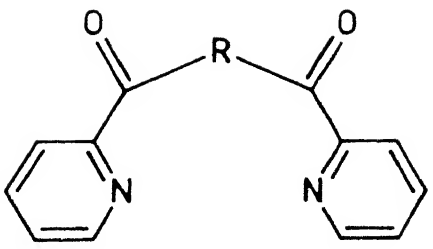

R = 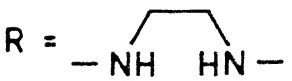 , (20a)

= 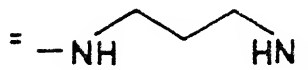 , (20b)

= 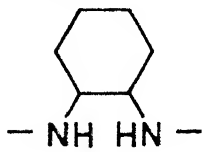 , (20c)

= 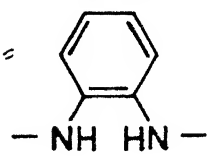 , (20d)

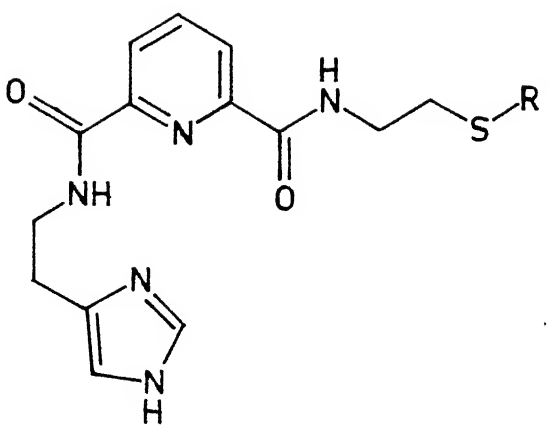

R = H , (21a)

= Me , (21b)

= MB , (21c)

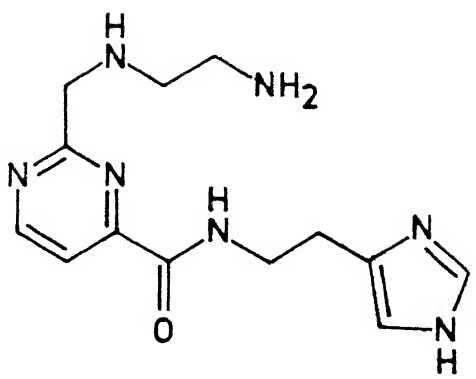

(22)

Ligand Types	Comments	References
(23a) to **(23f)**	Fe(II), Cu(II) complexes with protonated ligands. Deprotonation on pH change. Absorption spectra, EPR, electrochemistry, O_2 binding.	64,67-70

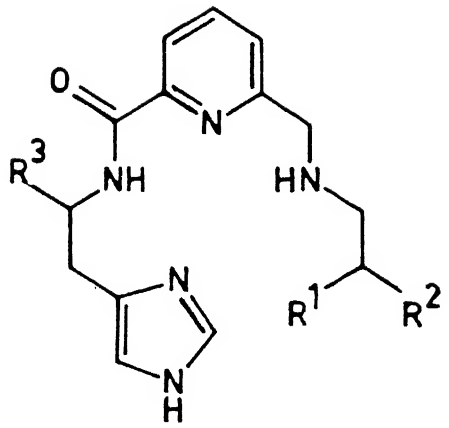

R_1	R_2	R_3	
$-NH_2$	$-COOMe$	H	(23a)
$-NH_2$	$-COOH$	$-CONH_2$	(23b)
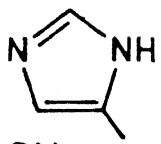	H	H	(23c)
$-SMe$	H	H	(23d)
$-SCH_2C_6H_5OMe$	H	H	(23e)
$-SH$	H	H	(23f)

Scheme I

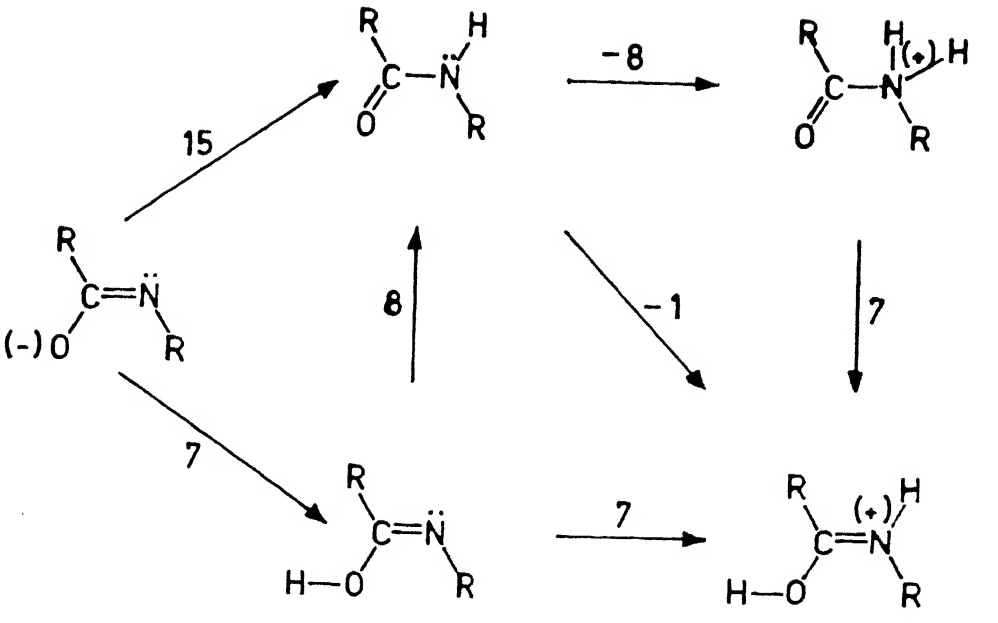

Beginning on the left, the deprotonated amide anion protonates at the nitrogen with log K_a = 15 to give the neutral amide at the top center of Scheme I. In acid solution O-protonation occurs with log K_a = -1 and N-protonation with log K_a = -8; these cationic species occur at the right side of Scheme I. This amide group protonation anticipates the results for metal ion complexation. The information obtained from the above discussion of proton equilibria can be summarized as follows:

(a) the deprotonated amide binds with the metal via amide nitrogen atom whereas neutral amide binds via oxygen atom.

(b) the deprotonated amide binds more strongly (log K_a = 15) with metal than neutral amide (log K_a = -1).

The high pK_a (≈ 15) value of nitrogen bound hydrogen implies that alkali and alkaline earth metal ions will not affect its removal. Transition-metal ions promise to be more effective in substituting the nitrogen bound amide hydrogen, but they suffer competition with metal ion hydrolysis and precipitation in

neutral and basic solutions.

To bring out full metal ion binding capabilities of amides, the chelate ring formation can be utilized. A metal ion needs a primary ligating site or anchor in order to chelate to the amide oxygen and, by substitution of a hydrogen, to the amide nitrogen. By providing an anchor for the metal ion and the possibility of chelation with the amide bond, the primary binding site reduces the importance of metal ion hydrolysis and permits the substitution of amide hydrogen easier.

1.2.1 Dipeptides, Tripeptides, and Mixed peptide Ligands

Condensation of two or more amino acids gives rise to ligands where terminal groups act as anchors, and in alkaline solution form metal complexes with deprotonated amide groups. A significant amount of work on these type of ligation has been done mainly by Margerum and coworkers.[1-5] Table 1.1 summarizes a selected listing of known chemistry.

Two important findings in these investigations are as follows. First, high σ-donation property of deprotonated amide can stabilize the higher oxidation state of a metal. Margerum and coworkers[11] showed the gradual decrease in the Cu(III)/Cu(II) reduction potential with increase in the number of deprotonated amide groups with large number of tripeptides/tetrapeptides. Billo[12] has also shown the crystal field strength of deprotonated amide is greater than ammine and acetate. Secondly, as the deprotonation occurs in aqueous solution at higher pH(≈10) the complexation is limited to copper, nickel, zinc, palladium, and cobalt. Manganese and iron complexes with these type of ligands

are not known.

1.2.2 Amido-phenol and Amido-alkoxo Ligands

This is an important class of ligands containing phenol/alkoxide donor in addition to amide group. The combining effect of deprotonated phenol/alkoxide and amide enhances the higher oxidation state stabilizing capacity of the ligand. As a result a large number of metal complexes with metal in higher oxidation states has been prepared. Selected examples are summarized in Table 1.2.

The strong affinity of phenoxide to iron(III) permits the use of a strong base (NaOMe) in the complexation reaction in nonaqueous media.[17] The strong in-plane ligand field of the amido-alkoxo ligands facilitate the stabilization of rare square planar cobalt(III) complexes.[23-26]

1.2.3 Cyclic All-amide Ligands

A number of research groups have studied the chemistry of macrocyclic transition-metal complexes with one, two, or three amido-N ligands.[4] In all these cases, the amide unit is part of a macrocycle in which one or more neutral Lewis base ligands, such as, amines act as an anchor. On the other hand, cyclic all amide ligands posseses no such anchoring group. Reasonably, before the contributions of Collins and coworkers[29-34] only one such complex was reported by Margerum and coworkers.[35-36] Collins and coworkers used Bu^nLi as a base in anhydrous nonaqueous medium prior to addition of metal ions.[34] A brief summary of the results using these ligands are presented in Table 1.3.

1.2.4 Pyridinecarboxamide Ligands

In these diverse group of ligands understandably pyridine acts as an anchoring group, as a result, base requirement becomes less stringent. Earlier works, mainly by Yamasaki and coworkers,[37,41-44] were limited to divalent copper, nickel, paladium, and cobalt. It was Mascharak and coworkers in their metal-bleomycin interaction modeling first structurally characterized the iron(III) amide complex with pyridine carboxamide unit.[48] Martel and coworkers reported the formation of amide complexes of iron in solution.[71-73]

An interesting point to note that, as the number of amide group per molecule is less than that encountered in earlier cases (Sections 1.2.1 and 1.2.3) as well as the absence of strong σ-donating supporting groups (phenoxide/alkoxide in Section 1.2.2) these ligands become less suitable for stabilizing higher oxidation states of the first transition series metal ions.

1.2.4 Summary

The discussions in the previous sections reveal the following facts:

(i) Though enormous amount of work has been done on Copper and Nickel with amide ligands, Manganese, Iron, Cobalt complexes with deprotonated amide ligands are only of recent origin. The competition between deprotonation and metal hydrolysis possibly play a tricky role in synthesizing these complexes.

(ii) Thorough studies on the effect of axial ligands for a group of isostructural complexes on various spectroscopic and

electrochemical properties have not been done. Synthetic manipulations of axial as well as equatorial ligands to vary the electron density at the metal center have not been done and hence would be of great interest.

(iii) Stereochemical consequences of ligand dispositions around the metal center using amide ligands have not been studied.

1.3 Scope of the Present Work

The information which has been provided in the previous sections provides a basis to appreciate the scope and limitations of the ligands chosen in the present work. The choice of a new organic molecule capable of acting as a potential ligand to metal ions deserves an attention on its own merit but the ultimate challenge lies in the fruitful use of those organic molecules to develop new interesting chemistry of greater importance to chemists in general and inorganic chemists in particular.

In this thesis work, we bacame interested in the use of the ligand system (1) primarily bacause of two reasons. First, this ligand system provides four nitrogen coordination in a grossly planar situation. If deprotonated, two amide nitrogens could provide two negative charges and hence the possibility of an effective delocalization network. This brings about a situation reminiscent of well known porphyrin ligation. Secondly, these ligands give us an unique opportunity to synthesize metal complexes having two different types of nitrogen coordination in the equatorial plane of an open chain system. The above situation in turn affords different metal-N bond distances at parity of N_4 equatorial coordination. Additionaly, axial positions could be

manipulated at one's own will. The specific types of transition-metal complexes we have dealt with in Chapters 2-4 are as follows:

(i) Synthesis of Mn(III) complexes of the type trans-$[MnN_4X]$ (X = Cl^-, N_3^-, and SCN^-) and the effect of axial ligands in the stabilization of Mn(IV) state (Chapter 2).

(ii) Synthesis of Fe(III) complexes of the type trans-$[FeN_4X_2]^{1-}$ (X = Cl^-, $MeCO_2^-$, and CN^-) and trans-$[FeN_4(L)_2]^{1+}$ (L = pyridine) to explore the effect of axial ligands on the spin state of Fe(III) (Chapter 3).

(iii) Synthesis of Co(III) complexes of the type trans-$[CoN_4X_2]^{1-}$ (X = Cl^-, N_3^-, SCN^-, $MeCO_2^-$, and NO_2^-) to explore the possibility of correlating ligand field spectral parameters with Co^{III}-Co^{II} reduction potentials (Chapter 4).

In chapter 5 the tuning of electronic structural preferences via stereochemical consequences of ligand around metal center and its effect on electrochemical properties have been dealt with the Cu(II) ion as a probe.

CHAPTER 2

In Chapter 1 we have seen that organic amide groups stabilize high oxidation states of metal ions when coordinated with the deprotonated nitrogen. High-valent oxo-iron-porphyrin species have been proposed as active intermediates in the catalytic cycle of catalases,[74-78] peroxidases,[74-78] cytochrome P-450,[76-82] and cytochrome c oxidase.[76-84] While oxoiron(IV)-porphyrin complexes have been studied extensively[85-91] as simple active-site models for these biological systems, those of chromium[92-95] and manganese[96-101] have proven fruitful in terms of redox and/or oxygen-atom transfer[102] chemistry. In sharp contrast, manganese(III) complexes of tetradentate $\mathbf{N_4}$ non-porphyrin ligands are very few. A summary of known complexes has been given in Table 2.1.

Che and Cheng[58] demonstrated the epoxidation of cyclohexene, styrene, and toluene in acetonitrile using the manganese(III) complexes [Mn(bpb)X] (X= Cl^- or N_3^-) in the presence of iodosylbenzene. They proposed[58] the involvement of a high-valent oxo-manganese intermediate in the epoxidation of these organic substrates, without throwing any light on the solution properties (UV-visible spectra, electrochemistry etc.) of these complexes. We have therefore undertaken a systematic study of manganese(III)-bpb complexes to gain further information on their syntheses and detailed characterization. In this chapter we have tried to prove the generality of the synthetic procedure and more importantly, to unravel the solution properties of the manganese(III) complexes [Mn(bpb)X] (X= Cl^-, N_3^-, or SCN^-) by use of UV-visible spectroscopy, solution electrical conductivity, effective magnetic moment in solution, ^1H NMR spectroscopy, and electrochemistry.

Table 2.1 : Selected Manganese(III) Complexes of Tetradentate N_4 Non-porphyrin Ligands

Complexes	Comments	References
$[Mn(24)X_2]^{1+}$ X=Cl^-,Br^-,NCS^-	Hexacoordinated, high-spin, equatorial N_4 coordination. Magnetic moment,absorption spectra,electrochemistry.	103,104
$[Mn(25)X_2]^+$ X=Cl^-,Br^-,NCS^-,N_3^-	Hexacoordinated, high-spin, equatorial N_4 coordination. Magnetic moment, solid-state reflectance spectra.	105
[Mn(26)X].MeCN X=Cl^-,Br^-,SCN^-,N_3^-	Pentacoordinated, high-spin, equatorial N_4 coordination. Magnetic moment, absorption spectra.	106
$[Mn(27)X_2]^+$ X= Br^-,Cl^-	Hexacoordinated, high-spin, equatorial N_4 coordination. Magnetic moment, absorption spectra	107
$[Mn(L)Cl]^{2+}$ L = **(28a)** or **(28b)**	Pentacoordinated, high-spin, equatorial N_4 coordination. Magnetic moment, absorption spectra, ^1H NMR, EPR, and electrochemistry.	108

[a] Structure of the ligands are given in the next page.

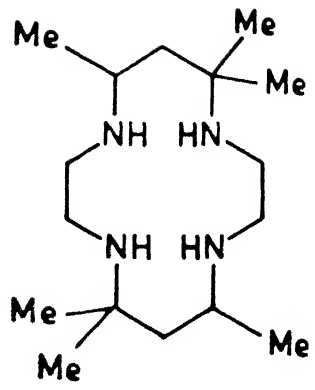

(24)

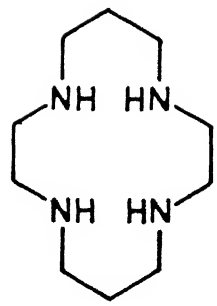

(25)

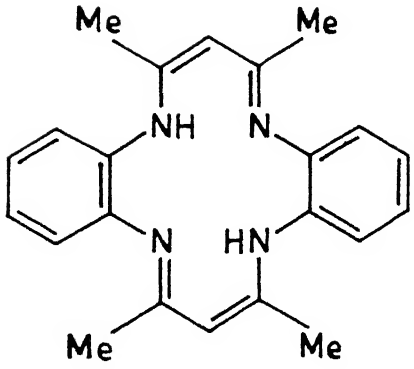

(26)

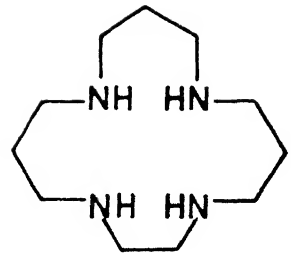

(27)

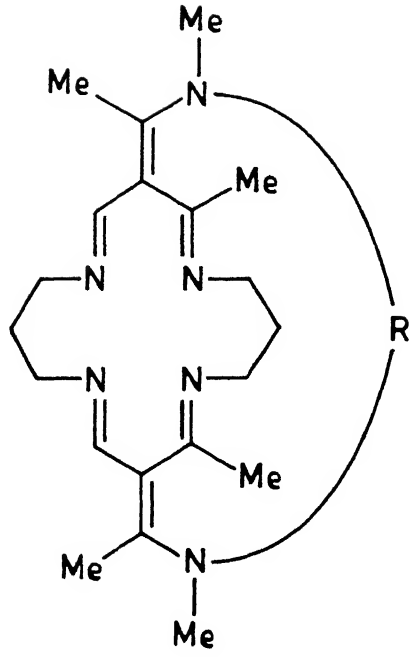

R = $(CH_2)_6$, (28a)

= m-xylylene , (28b)

2.1 Experimental Section

2.1.1 Solvents and Reagents

Solvents and reagents were obtained from commercial sources and used without further purification unless otherwise stated. Methanol was distilled from $Mg(OCH_3)_2$. Diethyl ether was dried first with anhydrous $CaCl_2$ and then refluxed with and distilled over sodium. Pyridine was distilled over and kept in presence of solid KOH. N,N-Dimethylformamide (DMF) was purified first by azeotropic distillation with benzene followed by shaking with alumina (neutral) and finally vacuum distillation. Chloroform was made acid free by washing with saturated sodium bicarbonate solution, then by washing five to six times with water followed by keeping over anhydrous calcium chloride for 24h and distilled. Dimethyl sulphate was purified[109] by washing with an equal volume of ice-water, followed by saturated sodium bicarbonate solution, drying over calcium oxide and finally vacuum distilled. Tetra-n-butylammonium perchlorate (TBAP) was prepared from tetra-n-butylammonium bromide and 70% aqueous perchloric acid. This was recrystallized from ethanol and dried in vacuo. The $Mn(O_2CMe)_3.2H_2O$ was prepared as previously described.[110] The tetra-n-butylammonium azide and tetra-n-butylammonium thiocyanate were prepared by metathesis of NaN_3 and KSCN with tetra-n-butyl ammonium chloride in acetone. Picolinic acid, tri-phenyl phosphite, methyl substituted pyridines and 4,5 dichloro 1,2-diamino benzene were brought from Aldrich Chemical Co. Dinitrogen was purified by bubbling it through an alkaline dithionite reducing solution.

2.1.2 Measurements

IR spectra were recorded in KBr disks with the help of a Perkin Elmer M-580 or M-1320 IR spectrophotometer. Electronic spectra were measured with a Perkin-Elmer Lambda 2 spectrophotometer. The ^1H NMR spectra of ligands were recorded in $CDCl_3$ on a Brüker WP-80 (80 MHz) instrument and for Mn(III) complexes in d_6-DMSO on a Brüker WM-400(400 MHz) spectrometer. The 400 MHz NMR facility was provided by CDRI, Lucknow. Solution magnetic susceptibility measurements were made by the usual NMR method[111] with a PMX-60 JEOL (60 MHz) spectrometer and made use of the paramagnetic shift of the methyl protons of DMF/acetonitrile and the $SiMe_4$ reference as the measured NMR parameter using the Equation 2.1

$$\text{Mass susceptibility } X_M = \frac{3\,\Delta f}{2\,\pi\, f\, m} + X_o + \frac{X_o(d_o - d_s)}{m} \qquad (2.1)$$

where Δf is the frequency separation between the two TMS or solvent peaks in Hz, f is the frequency at which the proton resonances are being studied in Hz, m is the mass of substance contained in 1 mL of solution, X_o is the mass susceptibility of the solvent, d_o is the density of the solvent and d_s that of solution. Final term involved in Equation 2.1 is negligible for the highly paramagnetic substances.

The temperature of the NMR probe was determined[112] using CH_3OH proton signals using Equation 2.2

$$T = 435.5 - 1.193\,(\Delta f) - 29.3\,(\Delta f \times 10^{-2})^2 \qquad (2.2)$$

where Δf is the frequency difference between the peak positions

of $-CH_3$ and $-OH$ protons, in Hz. Solvent susceptibilities[113] and diamagnetic corrections[114] were taken from literature tabulations. Solution electrical conductivity measurements were made with an Elico (Hyderabad, India) Type CM-82 T conductivity bridge.

X-Band EPR spectrum were recorded with a Varian E-109 C spectrometer fitted with a quartz dewar for measurements at liquid dinitrogen temperature. The spectrum were calibrated with the help of DPPH (g = 2.0037).

Cyclic voltammetric measurements were performed by using the PAR Model 370-4 electrochemistry system incorporating the following: Model 174A polarographic analyzer; Model 175 universal programmer; Model RE-0074 X-Y recorder. Potentials are reported at ≈25°C relative to an aqueous saturated calomel reference electrode (SCE) and are uncorrected for junction potentials. The complex to supporting electrolyte , TBAP, ratio was kept at ~ 1:150 throughout the measurements. A PAR G0021 glassy carbon electrode was used as the working electrode. In DMF solutions at a scan rate of 50 mV s^{-1} the above condition was found to give best performance with glassy carbon electrode for the $[Fe(\eta^5\text{-}C_5H_5)_2]^+/[Fe(\eta^5\text{-}C_5H_5)_2]$ couple. The system was calibrated against ferrocene, $[Fe(\eta^5\text{-}C_5H_5)_2]$,[115] and tris(2,2´-bipyridine)iron(II) perchlorate, $[Fe(bipy)_3](ClO_4)_2$.[116] At a glassy carbon electrode the E_f and the peak-to-peak separation (ΔE_p) values are + 0.49 V and 80 mV respectively. E_f is taken as the average of cathodic (E_{pc}) and anodic (E_{pa}) peak potentials (Equation 2.3):

$$E_f = 0.5(E_{pc} + E_{pa}) \qquad (2.3)$$

A sealed all-glass cell was used; measurements were made under an atmosphere of dry dinitrogen. The auxiliary electrode, which consisted of a platinum flag sealed in soft glass, and the reference electrode were separated from the working solution by means of fritted bridge filled with the same solvent and supporting electrolyte. Uncompensated solution resistance in the cell configuration was minimized by placing the tip of the reference electrode as close to the working electrode as possible.

Coulometric experiments were carried out using the Model 173 Potentiostat/ Galvanostat and a platinum-wire-gauze electrode was used as a working electrode. Number of electron (n) passed through the complex was determined from the ratio of Q/Q´, where Q is the coulomb count at the end of electrolysis and Q´ is the calculated coulomb count for one-electron transfer. The solutions were ~1.0 mM in complex and 0.2 M in supporting electrolyte, TBAP.

2.2 Syntheses of Ligands

The ligand 1,2-bis(2-pyridinecarboxamido)benzene (H_2(bpb))[52] and 4,5-dichloro-1,2-bis(2-pyridinecarboxamido)benzene(H_2(bpc))[61] were prepared following the reported procedure. The outline of their syntheses is given below. The 3-methyl (H_2(3-Mebpb)), 4-methyl (H_2(4-Mebpb)), and 3,5-di-methyl (H_2(3,5-Dimebpb)) substituted ligands were synthesized as shown in Scheme II. The substituted pyridine N-oxides,[117,118] cyanides,[119-121] and susequently their hydrolysis to carboxylic acids[119] were prepared by modifying reported procedures, the detailed

Scheme I

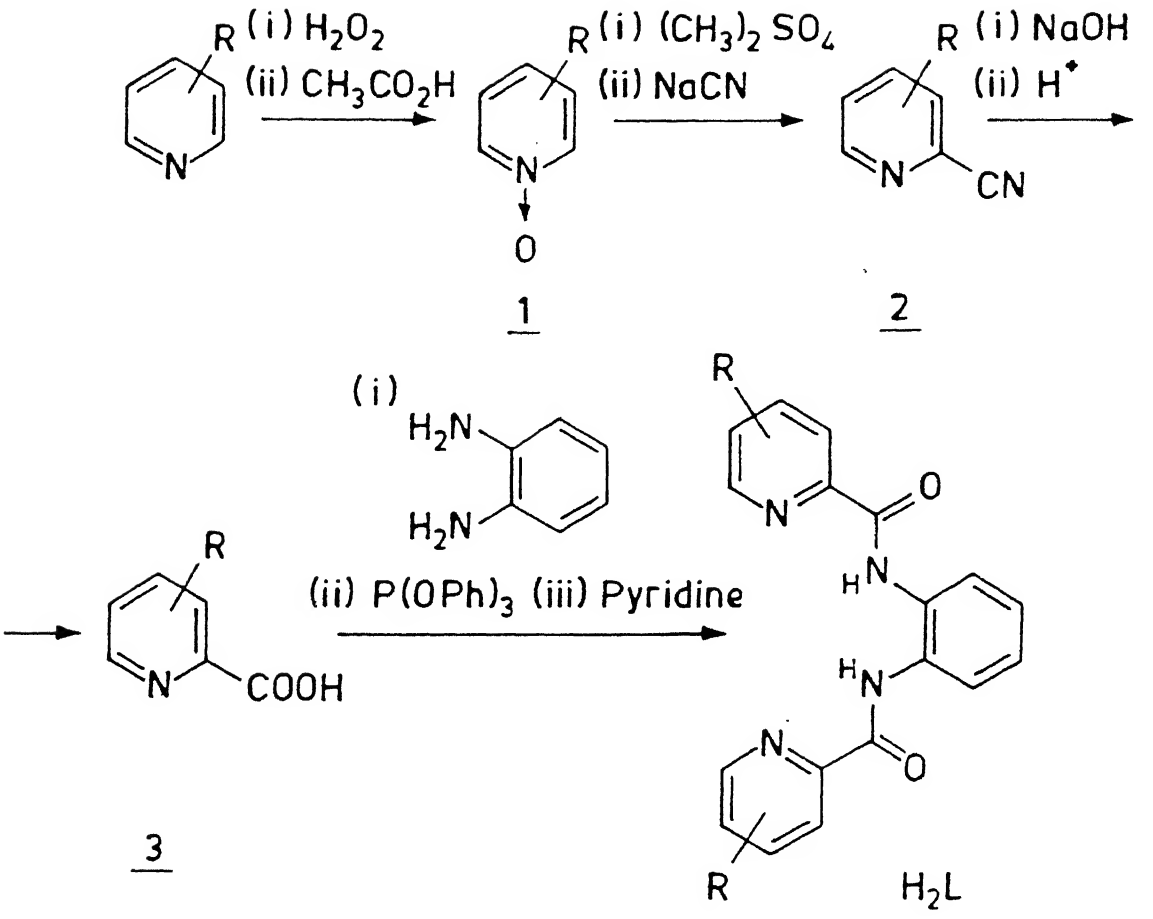

R = 3-Me : H_2L = H_2(3-Mebpb)

R = 4-Me : H_2L = H_2(4-Mebpb)

R = 3,5-$(Me)_2$: H_2L = H_2(3,5-Dimebpb)

syntheses are given below. Purity at each step was checked by ^1H NMR and/or melting point.

2.2.1 Substituted Pyridine N-Oxides

The 3-methyl and 4-methyl substituted pyridine N-oxides were prepared following a modified procedure[118] and 3,5-dimethyl sustituted one was prepared following a reported procedure.[117] The details of a representative one is given below.

2.2.1.1 3-Methyl Pyridine N-Oxide

A mixture of 3-Methyl pyridine (46.6 g, 0.50 mol), glacial acetic acid(300 mL) and 30% H_2O_2(50 mL) was heated at 70-80°C for 3h. An additional 35 mL of 30% H_2O_2 was added and heated on a water bath for 9h at 70-80°C. The resulting mixture was then concentrated to a volume of 100 mL in a rotary evaporator. Water(100mL) was added and again evaporated to 100 mL. This procedure was repeated until smell of acetic acid became faint. The resultant oil was evaporated in a vaccum pump(15mm of Hg) as much as possible to remove traces of 3-Methyl pyridine and water. The residual oil was taken up in 250 mL of $CHCl_3$ and shaken with an aqueous paste of K_2CO_3 to remove traces of acetic acid. The solution kept for sometime until evolution of CO_2 stopped. The solid CH_3COOK formed was filtered and anhydrous $MgSO_4$ was added to remove remaining water. The solution thus obtained was filtered after 6h and $CHCl_3$ was evaporated under vaccum. The crude product thus obtained was distilled at 146-149°C (15 mm of Hg) to get a colourless oil (yield, 40 g, ≈ 70%).

^1H NMR ($CDCl_3$): δ 2.30(s, 3 H), 7.00-7.38 (m, 2 H),

8.10(m, 2 H)

2.2.1.2 Methyl Pyridine N-Oxide

This was prepared in the same manner as in case of 3-methyl derivative. The crude oil obtained from 46.6 g of 4-methyl pyridine was vaccum dried (3 mm of Hg) for 1h. Solid product thus obtained was recrystallized from benzene (yield, 35 g, ≈ 65%) affording white crystals (m.p.184 °C ;reported 185-186°C).[118]

^{1}H NMR ($CDCl_3$): δ 2.37(s, 3 H), 7.12(d, 2 H), 8.16(d, 2 H)

2.2.1.3 3,5 Dimethyl Pyridine N-Oxide

This was prepared following a reported[117] procedure. From 40.0 g of 3,5-dimethylpyridine white crystallline product was obtained (yield, 32.2 g, ≈ 70%). The compound was very moisture sensitive so melting point was not checked.

^{1}H NMR ($CDCl_3$): δ 2.28(s, 3 H), 7.00(d, 2 H), 8.00(d, 2 H).

2.2.2 Substituted 2-Cyanopyridines

These were prepared modifying a reported procedure.[121] The details of a representative one is described below.

2.2.2.1 3-Methyl 2-Cyanopyridine

The 3-methyl pyridine N-oxide (30.0 g, 0.28 mol) was placed in a 100 mL three-necked round-bottom flask equipped with a thermometer and a condenser. Dimethyl sulphate (17.4 mL,0.18 mol) was added dropwise with stirring at an ice-cold condition. Then the mixture was warmed gradually to about 50°C on water bath to give a molten salt. Next an additional ammount of dimethyl sulphate (8.7 mL, 0.09 mol) was added dropwise and the mixture

warmed to 90°C for 2h with stirring. It was then cooled to room temperature and kept under vaccum (3 mm of Hg) for 2h. The N-methyl ammonium salt thus isolated was dissolved in 40 mL of water under dinitrogen atmosphere. This solution was added to a cold solution (-5°C) of NaCN (55.0 g, 1.12 mol) in 16 mL of water under dinitrogen. The mixture was stirred at 0 to 5°C for 3 h and kept at ~ 5°C overnight. The precipitate/oil thus obtained was extracted six times with dichloromethane and solvent was evaporated to obtain semi-solid crude cyanide. This was dried with Na_2SO_4 and crystallized from hot n-hexane to get white plate-like 3-methyl 2-cyanopyridine crystals (Yield, 9.2 g, ≈ 30%; m.p. 84°C ; reported 85-87°)[119,121]. IR data : $\nu_{C\equiv N}$ 2220 cm^{-1}.

^1H NMR ($CDCL_3$): δ 2.55(s, 3H), 7.55(q, 1 H), 7.85(d, 1 H), 8.70(d, 1 H).

2.2.2.2 4-Methyl 2-Cyanopyridine

From 30.0 g of 4-methyl pyridine N-oxide white crystals of 10.0 g product was obtained (yield, ≈ 30 %; m.p. 88°C; reported 87-89°C).[119,120] IR data: $\nu_{C\equiv N}$ 2240 cm^{-1}.

^1H NMR ($CDCl_3$): δ 2.37(s, 3 H), 7.25(d, 1 H), 7.43(s, 1 H), 8.50(d, 1 H).

2.2.2.3 3,5-Dimethyl 2-Cyanopyridine

From 30.0 g of the corresponding N-oxide 10.5 g white crystalline product was obtained (yield,≈ 30 %; m.p. 55°C; reported 56-58°C).[119] IR data: $\nu_{C\equiv N}$ 2210 cm^{-1}.

^1H NMR ($CDCL_3$): δ 2.40(s, 3 H), 2.53(s, 3 H), 7.53(s, 1 H), 8.43(s, 1 H).

2.2.3 Substituted Pyridine-2-carboxylic Acids

The base-catalyzed hydrolysis of the cyanopyridines to their corresponding carboxylic acids were carried out following a reported[119] procedure. The details are given below.

Sustituted cyanopyridines (9.0 g, 76.2 mmol) were heated under reflux with 70 mL of 3N sodium hydroxide for 15 h. The resulting cooled solution was acidified to pH ~ 3 with 1N HCl and the aqueous solution was evaporated to dryness. The solid extracted with ethanol and evaporated to dryness. Finally, it was recrystallized from benzene/n-hexane to get white crystalline powder in 60-70 % yield.

2.2.3.1 3-Methyl Pyridine-2-carboxylic Acid

From 9.0 g of 3-methyl 2-cyanopyridine 7.1 g product was obtained (yield 68%; m.p. 115°C; reported 117-118°C).[119]
IR data: $\nu_{C=O}$ 1650 cm^{-1} .

^1H NMR ($CDCl_3$) : δ 2.81(s, 3 H), 7.56(dd, 1 H), 7.81(d, 1 H)
8.56(d, 1 H)

2.2.3.2 4-Methyl Pyridine 2-carboxylic Acid

From 9.0 g corresponding cyanopyridine 7.4 g of the product was obtained (yield 71%: m.p. 131°C; reported 133-134°C)[119]. IR data: $\nu_{C=O}$ 1650 cm^{-1} .

^1H NMR ($CDCl_3$): δ 2.50(s, 3 H), 7.43(d, 1 H), 8.12(s, 1 H)
8.59(d, 1 H)

2.2.3.3 3,5-Dimethylpyridine 2-carboxylic Acid

From 9.0 g of the corresponding cyanopyridine 6 g of the pr-

oduct was obtained (yield 59%: m.p. 147°C; reported 146-148°C).[119] IR data: $\nu_{C=O}$ 1645 cm^{-1} .

^1H NMR ($CDCl_3$) : δ 2.44(s, 3 H), 2.75(s, 3 H), 7.59(s, 1 H) 8.34(s, 1 H)

2.2.4 1,2-Bis(2-pyridinecarboxamido)benzene (H_2(bpb))

To a stirred solution of pyridine 2-carboxylic acid (9.74 g, 0.08 mol) in pyridine (32 mL), a solution of 1,2 diamino benzene (4.27 g, 0.04 mol) in pyridine (8 mL) was added dropwise. The solution stirred for 15 min and triphenyl phosphite (24.52 g, 0.08 mol) was added dropwise. The solution warmed at 100°C for 4h and kept open in the air for 24 h. The ligand precipitated as white needles. It was filtered and recrystallized from chloroform/n-hexane as white crystals (yield 7 g, 60 %). Melting point 162°C. IR data: ν_{N-H} 3320 and $\nu_{C=O}$ 1680 cm^{-1} .

^1H NMR ($CDCl_3$): δ 7.44(m, 4 H), 7.97(m, 4 H), 8.37(d, 2 H), 8.67(d, 2 H), 10.37(s, 2H)

2.2.5 4,5-Dichloro-1,2-bis(2-pyridinecarboxamido)benzene (H_2(bpc))

This was prepared following a similar procedure as described above; however, in this case 4,5 dichloro 1,2-diaminobenzene was used as starting material and the final product was obtained in 70% yield. Melting point 280°C. IR data: ν_{N-H} 3320 and $\nu_{C=O}$ 1700 cm^{-1} .

^1H NMR (CD_2Cl_2): δ 7.53(m, 2 H), 7.96(m, 2 H), 8.12(s, 2 H), 8.31(d, 2 H), 8.59(d, 2 H), 10.25(s, 2H).

2.2.6 Substituted Ligands

All the substituted ligands were prepared following a modified procedure.[52] The detailed procedure for a representative one is given below.

2.2.6.1 1,2-Bis(3-methyl-2-pyridinecarboxamido)benzene (H_2(3-Mebpb))

To a solution of 3-methyl pyridine 2-carboxylic acid (2.0 g, 14.3 mmol) and o-phenylenediamine (0.8 g, 7.4 mmol) in 15 mL of pyridine, triphenyl phosphite (4.46 g, 14.3 mmol) was added dropwise and the mixture was stirred at 100°C for 5h on a water bath. Pyridine was removed using a rotary evaporator and the residual oil was taken up in $CHCl_3$. The $CHCl_3$ was extracted three times with water followed by $NaHCO_3$ solution and finally with water. The resulting $CHCl_3$ solution was dried over anhydrous $MgSO_4$. The $CHCl_3$ solution was concentrated and added to a large volume of cold diethyl ether. It was stirred for 2 h and then filtered. The solid product was recrystallized from $CHCl_3$/n-hexane. The ammount of recrystallized product was 1.2 g (yield 50%). Melting point 152°C. IR data: γ_{N-H} 3320 and $\gamma_{C=O}$ 1670 cm^{-1}.

^1H NMR ($CDCL_3$) : δ 2.81(s, 6 H), 7.37(m, 4 H), 7.71(d, 2 H)
7.93(dd, 2 H), 8.44(d, 2 H), 10.47(s, 2H)

2.2.6.2 1,2-Bis(4-methyl-2-pyridinecarboxamido)benzene (H_2(4-Mebpb))

Starting with 2 g of 4-methyl pyridinecarboxylic acid, 1.4 g of the product was obtained (yield, 55 %). Melting point 168°C. IR data : γ_{N-H} 3330 and $\gamma_{C=O}$ 1680 cm^{-1} .

^1H NMR ($CDCl_3$): δ 2.50(s, 6 H), 7.31(m, 4 H), 7.97(dd, 2 H),

8.18(s, 2 H), 8.50(d, 2 H), 10.31(s, 2 H).

2.2.6.3 1,2-Bis(3,5-dimethyl-2-pyridinecarboxamido)benzene (H_2(3,5-Dimebpb))

Starting with 2 g of 3,5-dimethyl 2-cyanopyridine the product obtained was 1.0 g (yield 40%). Melting point 160 °C. IR data: ν_{N-H} 3320 and $\nu_{C=O}$ 1690 cm^{-1} .

^1H NMR ($CDCl_3$) : δ 2.34(s, 6 H), 2.75(s, 6 H), 7.22(dd, 2 H), 7.40(s, 2 H), 7.84(dd, 2 H), 8.18(s, 2 H), 10.47(s, 2H).

2.3 Synthesis of the Mn(III) complexes

The Mn(III) complexes of general formula [Mn(L)X] where L(2-) = deprotonated bis amide ligand (eg. bpb(2-), bpc(2-)) were prepared following similar procedures as outlined in the literature.[58] The details of two are given below. Analytical results are presented in Table 2.2.

2.3.1 [Mn(bpb)Cl]

To a mixture of H_2(bpb) (0.16 g, 0.5 mmol) and $Mn(O_2CMe)_3.2H_2O$ (0.13 g, 0.5 mmol) in methanol (15 mL) was added solid LiCl (0.30 g, 5 mmol). The mixture was stirred at 298 K magnetically for 15 min and then was heated to reflux for 1 h. It was then cooled and the precipitated brown microcrystalline complex was filtered off, washed with small amount of methanol and was dried in vacuo (yield ~ 70%). This simple procedure affords the complex in a good yield and purity.

Table 2.2: Microanalytical Data[a] of Manganese(III) Complexes

Complex	Empirical Formula	% C	% H	% N
[Mn(bpb)Cl]	$C_{18}H_{12}N_4O_2ClMn$	53.50 (53.15)	3.10 (2.95)	13.70 (13.80)
[Mn(bpb)(N_3)]	$C_{18}H_{12}N_7O_2Mn$	52.50 (52.30)	3.10 (2.90)	24.10 (23.75)
[Mn(bpb)(NCS)]	$C_{19}H_{12}N_5O_2SMn$	52.80 (53.15)	3.10 (2.80)	16.50 (16.30)
[Mn(3-Mebpb)(N_3)]	$C_{21}H_{16}N_7O_2Mn$	54.10 (54.40)	4.00 (3.65)	21.90 (22.21)
[Mn(4-Mebpb)(N_3)]	$C_{21}H_{16}N_7O_2Mn$	54.50 (54.40)	4.20 (3.65)	22.20 (22.21)
[Mn(3,5-Dimebpb)(N_3)]	$C_{23}H_{20}N_7O_2Mn$	55.90 (56.30)	4.40 (4.29)	20.20 (20.88)
[Mn(bpc)(N_3)]	$C_{18}H_{10}N_7O_2Cl_2Mn$	44.20 (44.84)	2.50 (2.09)	20.10 (20.33)

[a] Values in parantheses are calculated ones

2.3.2 [Mn(bpb)(N_3)]

A solution of Na[N_3] (0.04 g, 0.61 mmol) in methanol (15 mL) was treated with H_2(bpb) (0.16 g, 0.5 mmol) and $Mn(OAc)_3.2H_2O$ (130 mg, 0.5 mmol) and the mixture was stirred at 298 K magnetically for 15 min and then was heated to reflux for 1 h. After allowing to cool the brown microcrystalline complex which formed was filtered off, washed with small amount of methanol and was dried in vacuo (yield ~ 65%).

2.3.3 Zn(bpb).H_2O

This was prepared following similar procedures as outlined in the literature.[53]

An ethanolic solution of H_2(bpb) was added to an aqueous solution of zinc(II) acetate dihydrate in 1:1 mole ratio and the mixture was warmed on a water bath for 15 min. The yellow solution thus generated was filtered and kept in the air for two days. The yellow plates that had collected was filtered and washed with a little aqueous-ethanol and dried in vacuo (yield 80%). The purity was checked by elemental analysis (Table 2.2) as well as by ^{1}H NMR spectral analysis in d_6-DMSO (Figure 2.1).

^{1}H NMR (d_6-DMSO):δ6.87 (dd, 2 H), 7.81 (m, 2 H), 8.40 (m, 4 H), 9.06 (d, 2H).

2.4 Results and Discussion

2.4.1 Syntheses and Selected Properties

The substituted pyridine 2-carboxylic acids were prepared following modified reported procedures (Section 2.2). In the case of cyanopyridines $\nu_{C\equiv N}$ observed at ~ 2220 cm^{-1} (Section 2.2)

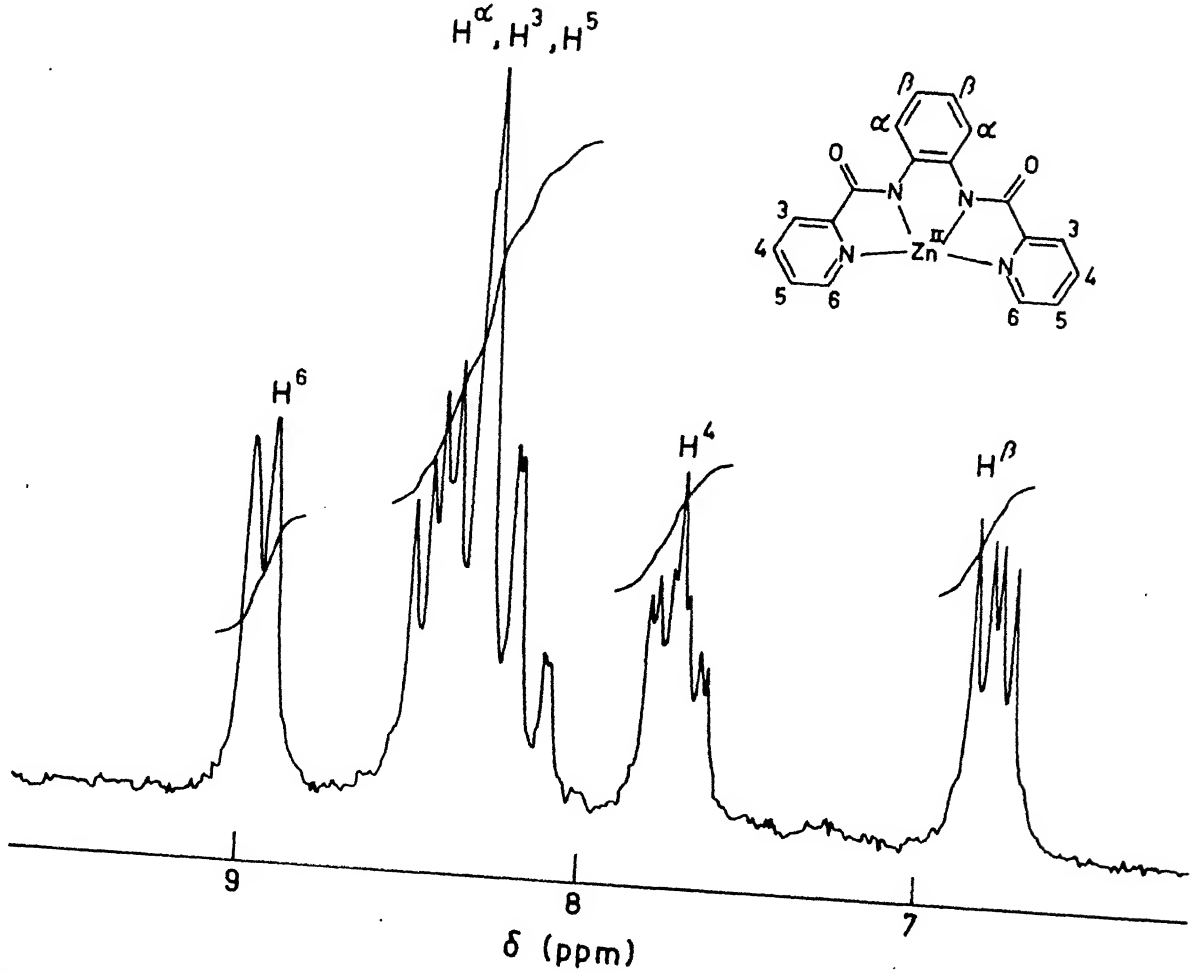

Figure 2.1 Partial ^1H NMR of $[Zn(bpb)].H_2O$ in d_6DMSO solution.

confirms the presence of -C≡N functionality.

The ligands were prepared by condensation between corresponding amines and pyridine 2-carboxylic acids in the presence of triphenyl phosphite which acts as water scavenger. One sharp band in the IR spectra at ~ 3330 cm^{-1} (Section 2.2.6) for ν_{N-H} indicates the formation of amide bonds. The $\nu_{C=O}$ in the ligands shows a sharp intense absorption at ~ 1680 cm^{-1} (Section 2.2.6) as reported for analogous ligands.[52] The ^1H NMR spectra of the ligands show one broad absorption at ~ 10.3 ppm for the N-H proton. Purity of the ligands were checked by ^1H NMR spectral measurements (Section 2.2.6). A representative ^1H NMR spectrum of a substituted ligand is shown in Figure 2.2.

The complexes [Mn(L)X] where L(2-) = bisamide ligands (e.g., bpb(2-), bpc(2-) etc.) and X = Cl^-, N_3^-, and SCN^- were readily prepared using '$Mn(OAC)_3.2H_2O$' and Li^+, Na^+ or K^+ salts of the anions in methanol. The manganese (III) complexes were isolated as brown crystalline solids in good yields (60-80 %). The synthesis and IR spectra of Cl^- and N_3^- complexes of bpb(2-) were reported previously[58]. The IR spectra of all the complexes show the absense of ν_{N-H} band and to lower energy shifts of ν_{amideI} bands indicate the complexation of the ligands in deprotonated forms and the metal coordination via amide nitrogen (Table 2.3) as reported by Vagg and coworkers[53,54] for similar amide complexes. The IR spectra of azido complexes show strong absorptions at ~ 2040 cm^{-1} due to the presence of N_3^-.[122] The SCN^- complex shows an intense IR absorption for $\nu_{C=N}$ at 2050 cm^{-1}. However, the $\nu_{C=S}$ stretching mode of SCN^- is apparently obscured by ligand absorptions. The latter has been shown to be

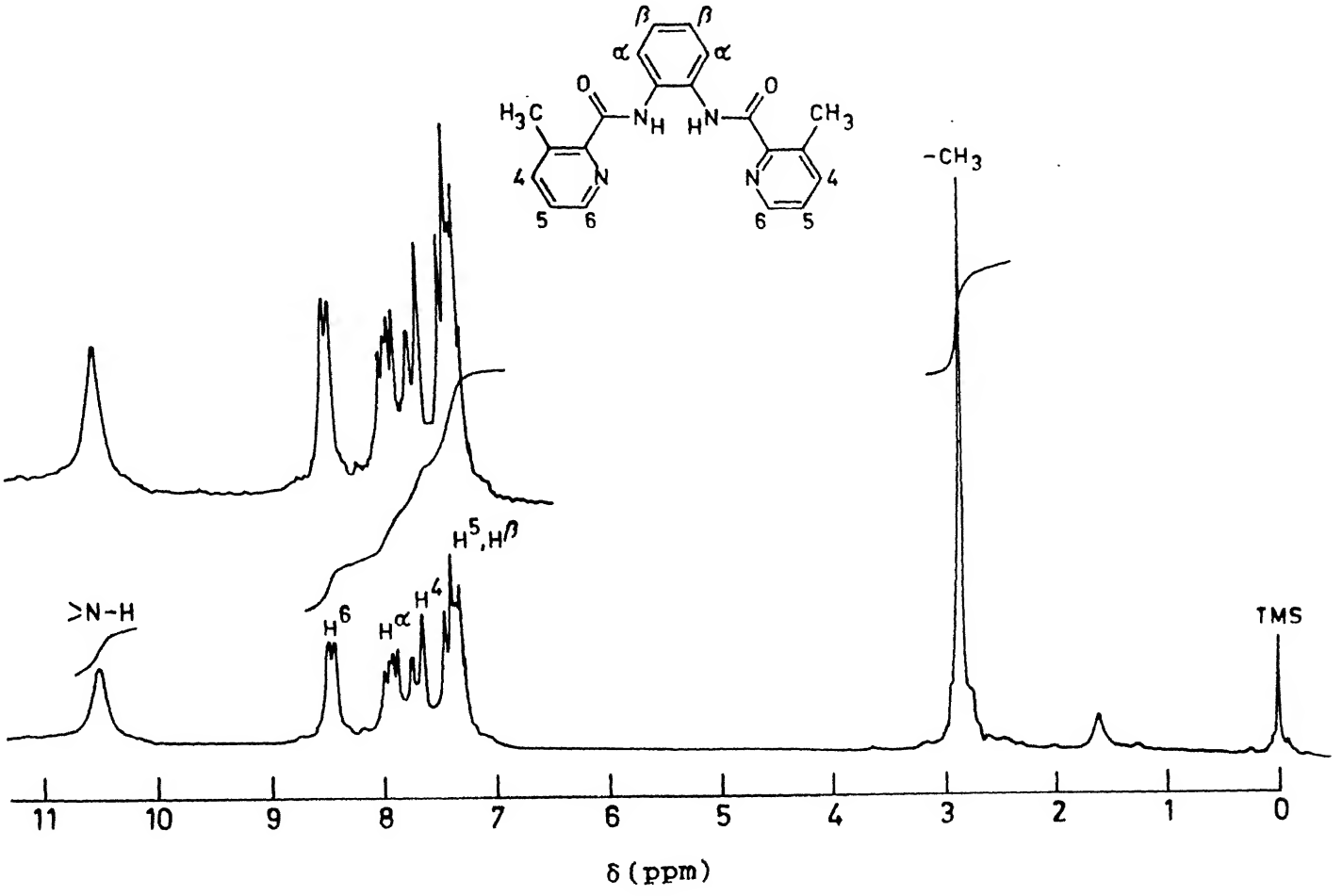

Figure 2.2 ^1H NMR of H_2(3-Mebpb) in $CDCl_3$ solution.

diagnostic[122] of N or S bonded SCN^- and, less critically, the presence of $\nu_{C\equiv N}$ below 2100 cm^{-1} indicates[122] (bpb)Mn-NCS bonding. Except [Mn(3,5-dimebpb)(N_3)] all other complexes are soluble in reasonable concentrations only in DMF and DMSO. We have performed the solution studies in DMF. The complex [Mn(3,5-dimebpb)(N_3)] is insoluble even in DMF and DMSO. Therefore the solution studies on this complex could not be made. Conductivity measurements show that except [Mn(bpb)(NCS)] all other complexes are predominantly nonelectrolyte (Table 2.3). The complex [Mn(bpb)(NCS)] behaves as a 1:1 electrolyte[123] (Table 2.3). Magnetic moment measurements in DMF solution using the Evans method[111] give values of $\mu_{eff.}$ = 4.78 - 4.90 μ_B (Table 2.3), consistent with the presence of monomeric high-spin d^4 (S = 2) manganese(III) complexes. This is in excellent agreement with the solid state values of 4.7 - 4.9 μ_B reported previously for [Mn(bpb)Cl] and [Mn(bpb)(N_3)] by Che and coworkers.[58]

The zinc(II) complex of the bpb(2-) ligand was prepared following a procedure outlined in the literature.[53] The IR (Table 2.3), solution conductivity (Table 2.3), and elemental analysis (Table 2.2) supports the formulation [Zn(bpb)].H_2O.

2.4.2 Absorption Spectra

The absoption spectra of manganese(III) as well as zinc(II) complexes in DMF solutions were measured in the 1100-270 nm region. Typical spectra are shown in Figure 2.3 and the data are listed in Table 2.4. The UV-visible spectra contain intense bands and shoulders in the ultraviolet and a moderately intense shoulder ~430 nm. The intense brown color of these manganese(III)

Table 2.3 : Molar conductance, Magnetic moment and Selected IR Data of Manganese(III) & Zinc(II) Complexes in DMF

Complex	Molar coductivity[a] Λ_M (Ω^{-1} cm^2 mol^{-1})	Magnetic moment[b] $\mu_{eff}(\mu_B)$	IR data[c] (cm^{-1})		
			ν_{amideI}	$\nu_{C\equiv N}$	ν_{N_3}
[Mn(bpb)Cl]	13	4.86	1640		
[Mn(bpb)(N_3)]	16	4.78	1640		2040
[Mn(bpb)(NCS)]	60	4.86	1650	2050	
[Mn(3-Mebpb)(N_3)]	10	4.90	1630		2040
[Mn(4-Mebpb)(N_3)]	8	4.90	1630		2030
[Mn(bpc)(N_3)]	15	4.78	1640		2050
[Mn(3,5-Dimebpb)(N_3)][d]	-	-	1620		2080
[Zn(bpb)].H_2O	3	-	1620		

[a] Expected 1:1 electrolyte range: 65-90 Ω^{-1} cm^2 mol^{-1} in DMF.[123]

[b] Measured in solution using Evans method.[111]

[c] In KBr disk (4000-600 cm^{-1}).

[d] Due to poor solubility of the complex, solution studies could not be performed.

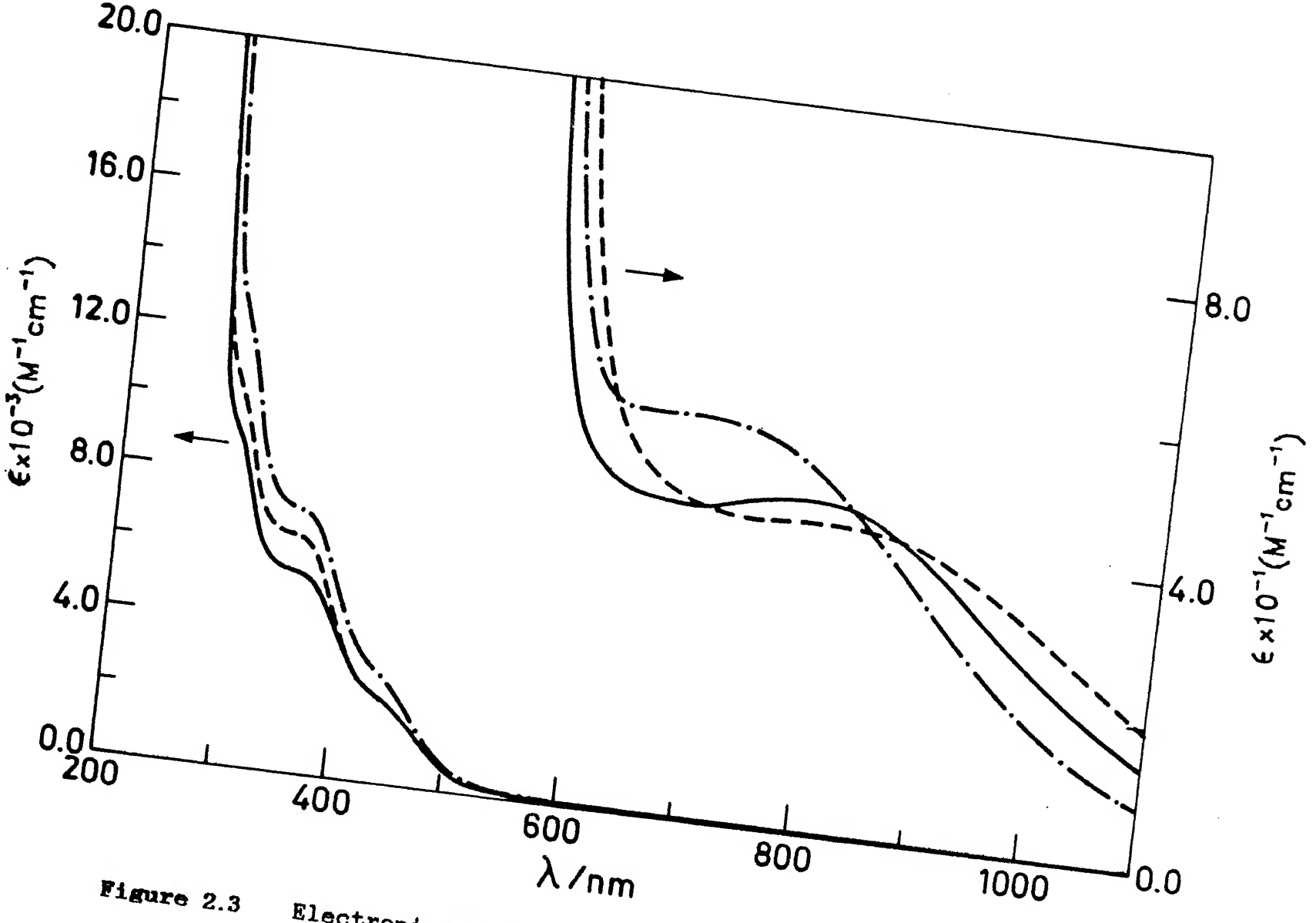

Figure 2.3 Electronic spectra of [Mn(bpb)Cl](——),[Mn(bpb)(N_3)] (- - -), and [Mn(bpb)(NCS)](—·—·—) in DMF solution.

Table 2.4 : Electronic Spectral Data of Manganese(III) & Zinc(II) Complexes in DMF

Complex	λ_{max},nm,(ϵ,$M^{-1}cm^{-1}$)
[Mn(bpb)Cl]	781(46), 435 sh[a](2 500), 367 sh(5 400), 300(9 100)
[Mn(bpb)(N_3)]	816(43), 435 sh(2 400), 367 sh(6 300), 300 sh(10 100)
[Mn(bpb)(NCS)]	673(56), 435 sh(3 100), 367 sh(7 050), 300 sh(12 100)
[Mn(3-Mebpb)(N_3)]	811 sh(60), 445 sh(1 700), 370 sh(3 700), 307 sh(7 900)
[Mn(4-Mebpb)(N_3)]	819 sh(57), 441 sh(2 300), 359 sh(6 573), 302 sh(10 600)
[Mn(bpc)(N_3)]	855 sh(20), 362 sh(3 500), 298 sh(11 100)
[Zn(bpb)].H_2O	361 (4 600) 301 sh(10 800)

[a] sh = shoulder.

complexes in solution is assignable to ligand ----> metal charge-transfer (LMCT) transitions ~ 430 nm. The absense of this band in [Zn(bpb)].H_2O confirms the LMCT nature of the transition ~ 430 nm.

In the near infrared region weak broad absorptions are also seen (Figure 2.3; Table 2.4). The high-spin manganese(III) complexes are expected to experience strong Jahn-Teller distortions. Assuming a square pyramidal structure for these five-coordinate complexes, and that the bpb(2-) ligand donor atoms are approximately equivalent, the ligand field about the metal would be ~ C_{4v}. Under this symmetry, three d-d transitions are expected: d_{z^2} ---> $d_{x^2-y^2}$ (I), d_{xy} ---> $d_{x^2-y^2}$ (II), and d_{xz}, d_{yz} ---> $d_{x^2-y^2}$ (III) (from lower to higher energy).[124-126]

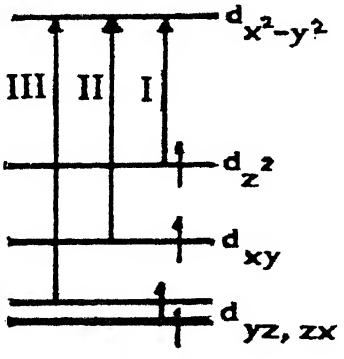

d^4 ion in ~ C_{4v} symmetry

The low-energy bands observed for Cl^- and N_3^- complexes can be assigned to transition I rather than II, since the energy of this band is found to be sensitive to the axial anion (Table 2.4). As the SCN^- complex completely dissociates in solution (Table 2.3), the absorbing species present in solution presumably is the tetragonal six-coordinate complex $[Mn(bpb)(DMF)_2]^+$. The

higher energy in this case (Table 2.4) is consistent with the decreased ligand field strength of the axial DMF and consequent stabilization of the d_{z^2} orbital.

The spectral features of these complexes are very similar to those reported for Mn^{III}-Schiff base[124-126] and Mn^{III}-N_4 macrocyclic ligand[104-106,108] complexes.

The structure of the complexes in the solid state is presumably five-coordinate with bpb(2-) functioning as a dianionic tetradentate N_4 ligand and the fifth coordination site occupied by an anion (Cl^-, N_3^-, and SCN^-). This structural pattern has been authenticated in the [Mn(acen)Cl] (acen = N,N'-ethylene bis (acetylacetoneiminate dianion)) and [Mn(tpp)X] (tpp = tetraphenylporphyrin dianion; X = Cl^-, N_3^-) complexes[127].

2.4.3 Solution Structure

As the magnetic moments of the complexes (Section 2.1) reveal the high-spin d^4 configurations, such a magnetic configuration is predicted to give observable NMR signals.[128] Indeed such signals can be seen in the ^1H NMR spectra for the azido complexes of manganese(III). They are broad and shifted considerably to both downfield as well as upfield of TMS (Table 2.5) due to the presence of paramagnetic high-spin manganese(III). Representative spectra of [Mn(bpb)(N_3)] and [Mn(4-Mebpb)(N_3)] are given in Figure 2.4

In order to assign the ^1H NMR spectra of these complexes we prepared a series of ring-substituted ligands (Scheme II). Assignments for the ring protons (H^3, H^4, and H^{β}), were made unambiguously by the effect of methyl/chloro ring substitution

Table 2.5: ^{1}H NMR Chemical Shifts Relative to TMS for High-spin Manganese(III) Complexes in d_6-DMSO

Complex	Assignments							
	H^3	H^4	H^β	H^5, H^6, H^α			3-Me	4-Me
[Mn(bpb)(N_3)]	-24.5	-18.5	-32.0	29.0	21.0	-32.0		
[Mn(bpc)(N_3)]	-25.0	-18.5		31.0	19.3	-31.5		
[Mn(3-Mebpb)(N_3)]		-16.1	-32.0	27.5	22.3	-32.0	-9.2	
[Mn(4-Mebpb)(N_3)]	-23.6		-31.5	28.3	20.5	-31.5		37.1

[a] Chemical shifts (δ) are in ppm unit with reference to TMS.

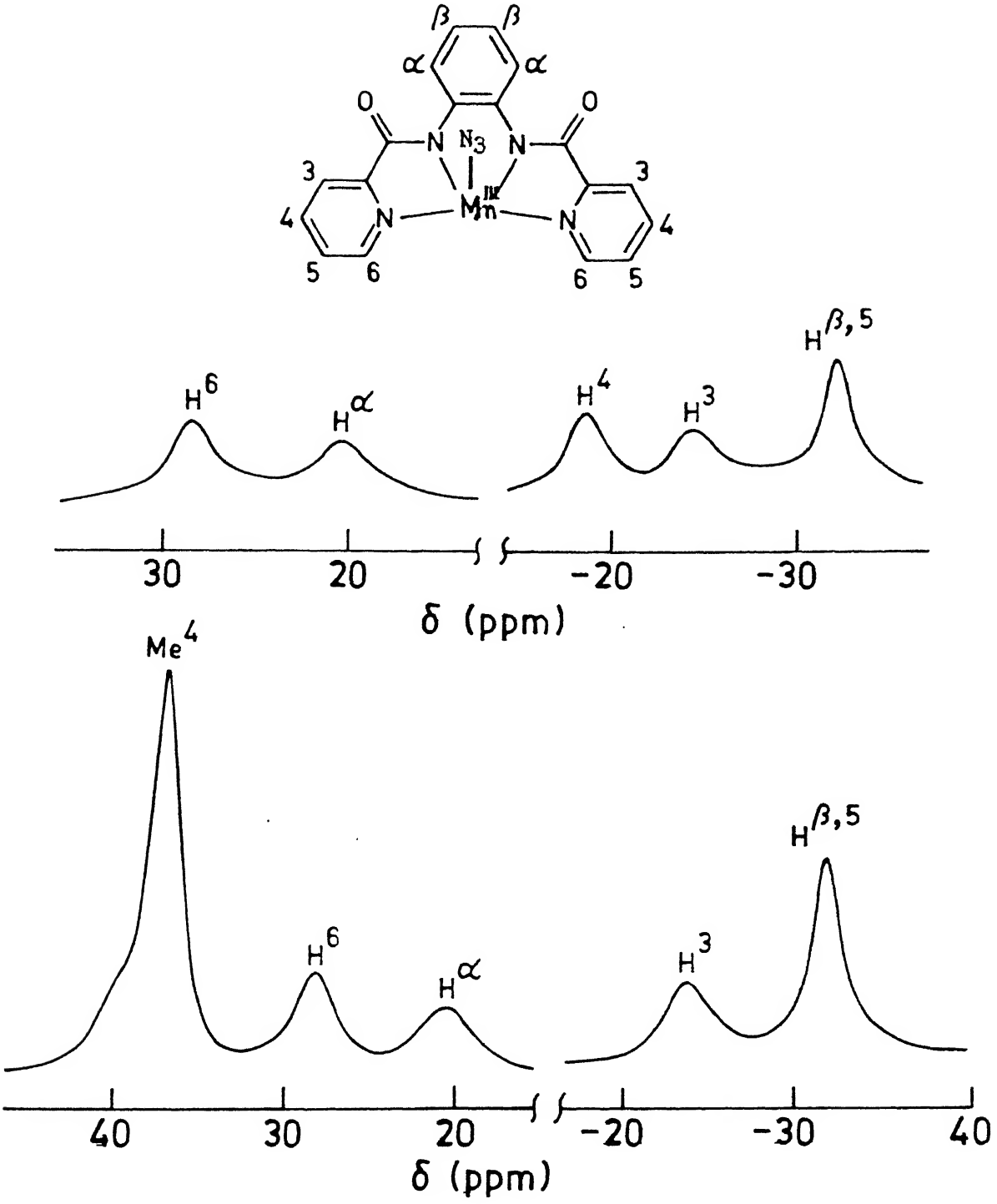

Figure 2.4 Fragmented ^1H NMR of (a) [Mn(bpb)(N_3)]; and (b) [Mn(4Mebpb)(N_3)] in d_6-DMSO solution.

for hydrogen and integrated area ratios. As for example, the assignment for the H^4/4-Me proton(s) has been done as stated below. The resonance of [Mn(bpb)(N_3)] at -18.5 ppm is absent in the 4-methyl substituted complex [Mn(4-Mebpb)(N_3)]. Instead in the latter case a resonance is observed at +37.1 ppm. We assign the resonance at -18.5 ppm due to H^4 in the case of the former complex and the resonance at +37.1 ppm due to 4-methyl in the latter case (Figure 2.4).

Both contact and dipolar contributions are expected to contribute to the observed isotropic shift (i.e., the observed chemical shift minus a reference diamagnetic shift).[129-132] We mean the free ligand proton resonances as the diamagnetic reference. Shifts arising from a σ-delocalization mechanism are characterized by a rapid attenuation of the paramagnetic effect. Such shifts are always downfield of the diamagnetic position, and a decrease of an order of magnitude with each intervening bond is typical. On the other hand, shifts derived from a π-delocalization mechanism do not attenuate with each intervening bond and are characterized by alternating in signs, thus allowing the possibility of upfield shifts. When a ring proton is methyl substituted, the alternating signs of H and CH_3 isotropic shifts indicate that π spin delocalization is responsible for the contact contributions.

The observed behavior (the effect of the 3- and 4-Me substitution) is indicative of a dominating contact contribution of π-spin delocalization mechanism.[129-132] We believe that the transfer of spins takes place from the filled ligand orbitals to the unfilled metal d level. At this level of available

experimental results we cannot elucidate the relative contributions of contact and dipolar effects in these complexes. From the above discussion mainly two results emerge: (i) the present ligand system coordinate to manganese(III) in a planar geometry, (ii) there is a considerable metal-ligand covalency in these complexes.

2.4.4 Electrochemistry

The purpose of the electrochemical measurements was to investigate the suitability of the bpb(2-) ligand to stabilize manganese(III) state towards reduction, and in addition to determine whether or not an oxidative response corresponding to the accessibility of higher oxidation states could be achieved.

2.4.4.1 Manganese(III)-Manganese(II) Couple

All the complexes with bpb(2-) display a cyclic response with characteristic anodic (E_{pa}) and cathodic (E_{pc}) peak potentials with E_f values in the range -0.03 V to + 0.03 V vs. SCE (Figure 2.5) due to the Mn^{III}-Mn^{II} couple. Among the complexes with substituted ligands, [Mn(bpc)Cl] displays Mn^{III}-Mn^{II} couple (E_f = +0.15 V vs. SCE) shifted towards more positive values due to the electron withdrawing property of the two chlorine atoms in the benzene ring. The complexes with methyl sustituted ligands the electron donating effect due to methyl substituents are minimal (shifted cathodically by ~ 30 mV than the analogous bpb(2-) system). The one-electron nature of this redox response has been identified by comparison of current height with the redox behaviour of a sample of $[Fe(bpy)_3]^{2+}$ under the

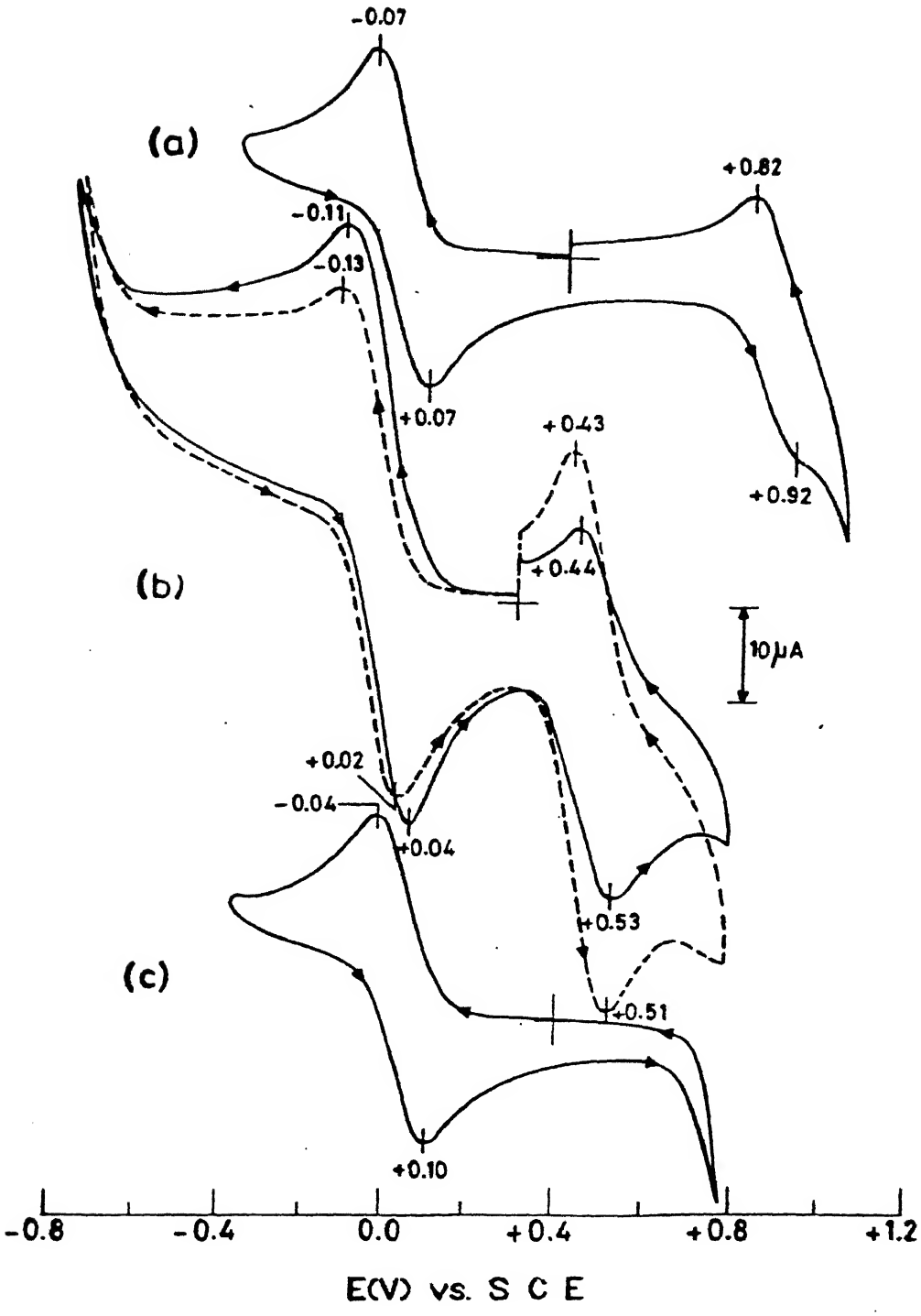

Figure 2.5 Cyclic voltammograms of (a) [Mn(bpb)Cl]; (b) [Mn(bpb)(N_3)] (——) and after the addition of one equivalent of [NBu^n_4]I (- - -);and (c) [Mn(bpb)(NCS)] in DMF. Condition: scan rate 50 mV s^{-1}; glassy carbon working electrode; supporting electrolyte TBAP.

same experimental conditions. The E_f values for the oxidation and reduction waves are recorded in Table 2.6

The peak-to-peak separations (ΔE_p) are ~ 150 mV at a scan rate of 50 mV s^{-1}. The anodic and cathodic peak heights are equal. The Mn^{III} - Mn^{II} couple is evidently quasireversible in nature. Accordingly, we assume that the lack of reversibility observed (Figure 2.4) is most likely due to the loss of axial ligands from the manganese (II) complex followed by solvation [equation (2.3)]. This behaviour has been previously noted for

$$[Mn^{III}(bpb)X] + 1e^- \longrightarrow [Mn^{II}(bpb)X]^{1-} \xrightarrow{DMF} [Mn^{II}(bpb)(DMF)_2] + X^- \quad (2.3)$$

manganese(III) macrocyclic complexes[133]. The potentials (Table 2.6) are comparable to Mn^{III} - Schiff base[134-136] and Mn^{III}-porphyrin[137] complexes. The manganese (III) ----> manganese (II) formal potentials have measurable dependence on the nature of axial ligands. The order of more negative E_f is N_3^- > Cl^- (Figure 2.5, Table 2.6). We cannot consider here the SCN^- complex since it is completely dissociated in DMF solution (Table 2.3). Among Cl^- and N_3^- complexes the shift in the potentials and the ordering are in excellent agreement with[137] the Mn^{III}-porphyrin system.

2.4.4.2 Manganese(IV)-Manganese(III) Couple

An interesting feature of [Mn(bpb)Cl] and [Mn(bpb)N_3] complexes is the appearance of a quasireversible oxidative wave ~ +0.9 V and +0.5 V respectively (Figure 2.5, Table 2.6). In the case of analogous bpc(2-) complex this quasireversible

Table 2.6: Cyclic Voltammetric[a,b] Data for the Manganese(III) Complexes in DMF

Complex	Mn^{III}-Mn^{II} couple		Mn^{IV}-Mn^{III} couple	
	E_f/ V	ΔE_p/ V	E_f/ V	ΔE_p/ V
[Mn(bpb)Cl]	0.00	140	0.87	100
[Mn(bpb)(N_3)]	-0.03	150	0.48	90
[Mn(bpb)(NCS)]	0.03	140	-	-
[Mn(3-Mebpb)(N_3)]	-0.06	140	0.50	100
[Mn(4-Mebpb)(N_3)]	-0.06	120	0.51	110
[Mn(bpc)(N_3)]	+0.15	100	0.60	80

[a] Meaning of the symbols used the same as in the text.

[b] Supporting electrolyte TBAP (0.1 M); glassy carbon working electrode; reference electrode SCE; scan rate 50 mV S^{-1}.

oxidation shifts towards more positive value (E_f= +0.6 V) due to ring chlorine substitution. In an effort to determine the site within the complex which has undergone the oxidation process (ligand or metal ion), the following controlled experiments were performed. The cyclic voltammetric behaviour of [Zn(bpb)].H_2O complex in DMF solution was examined (Figure 2.6). An irreversible oxidative response at +0.94 V and an ill-defined reduction at -1.64 V were observed. This process is probably due to the ligand oxidation. The redox behavior of [NBu_4^n][N_3] and [NBu_4^n][SCN] was also examined in DMF solutions. Again only irreversible oxidative responses of the anions were observed and the E_f values were +0.8 V and +0.96 V respectively. Thus the oxidative responses observed for [Mn(bpb)X](X = Cl^-, N_3^-) could be due to a manganese(III) ----> manganese(IV) oxidation (Equation 2.4).

$$[Mn^{IV}(L)X]^{1+} + e^- \text{ ---------> } [Mn^{III}(L)X] \qquad (2.4)$$

This seems quite reasonable since the accessibility of higher oxidation states of metal ions using bpb(2-) as ligand is documented in an electrochemically detected osmium(IV) complex[57] and a nitrido-chromium(V) complex[59] (Chapter 1). Our results clearly demonstrate the accessibility of formally manganese(IV) state at least on the cyclic voltammetric time scale using bpb(2-) or its various ring substituted derivatives as ligands. This confirms the prediction of Che and co-workers.[58]

The following observations are in order. When the axial ligand is bound to the metal center there is a possibility of

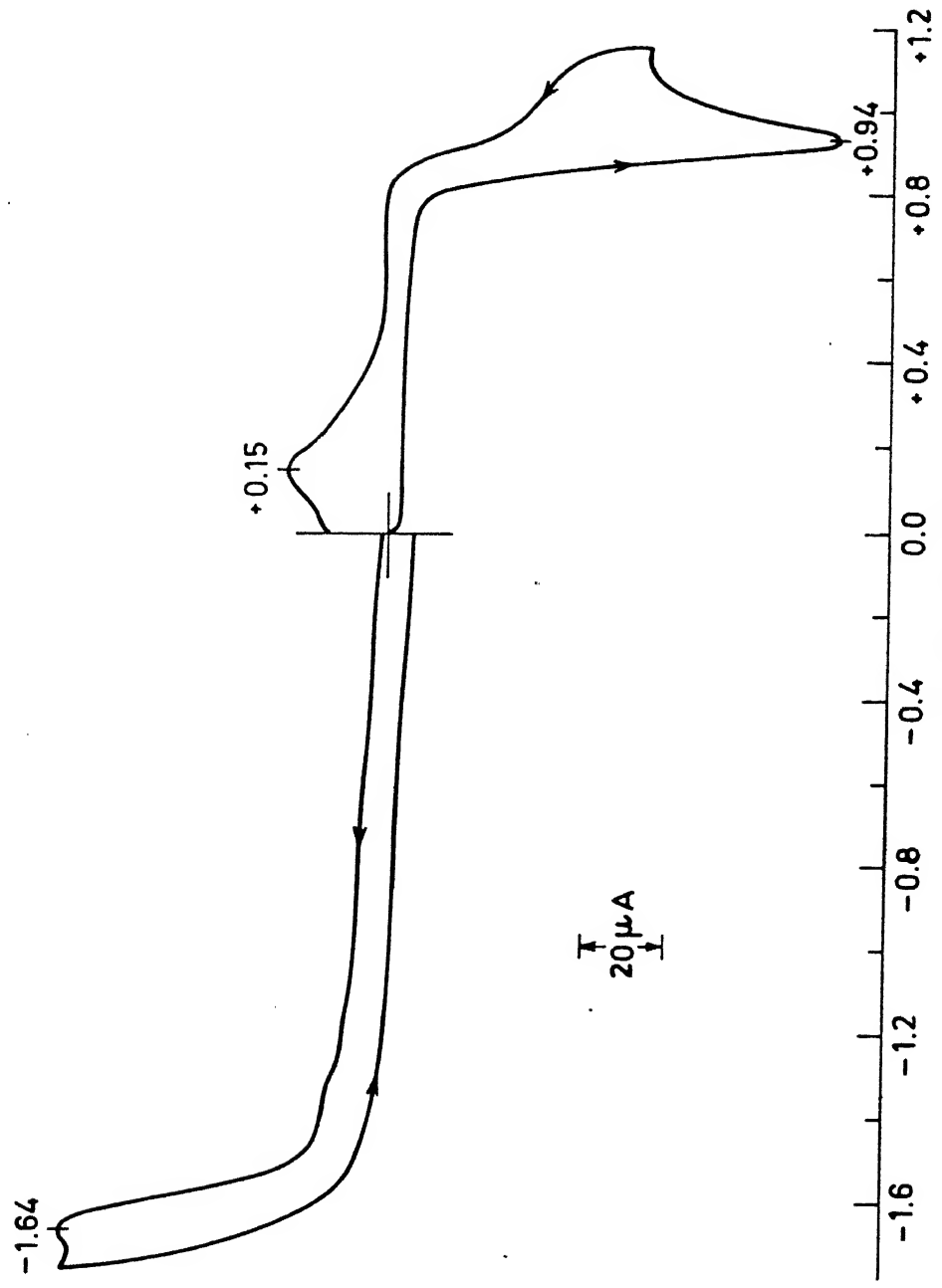

Figure 2.6 Cyclic voltammogram of $[Zn(bpb)].H_2O$ in DMF. Condition: scan rate 50 mV s^{-1}; glassy carbon working electrode; supporting electrolyte TBAP.

the bpb(2-)ligand can stabilize manganese formally in the higher oxidation state.

2.5 Conclusions

The major findings in this chapter are the following:

(i) Our goal of exploring the solution properties of [Mn(bpb)X] (X = Cl^-, N_3^-, SCN^-) has been achieved.

(ii) The ^1H NMR spectral analysis shows an extensive delocalization by the present deprotonated ligands. It also shows that these ligands coordinate in a planar geometry.

(iii) The complexes display an Mn^{III}-Mn^{II} couple subject to the shift of formal potentials under the influence of axial ligands.

(iv) The accessibility of an oxidative response also depends on the nature of the axial ligands.

(v) The present in-plane ligand system is not suitable to generate a manganese(IV) species of considerable stability.

CHAPTER 3

Nature's elaboration of the fundamental iron porphyrin structure has resulted in a multiplicity of functions for the hemoproteins. Protein control of the axial ligation modes of the heme group, both number and type being variable, is one of the most important of the parameters which control hemoprotein structure.[138]

In the non-heme/non-iron-sulfur family bleomycins (BLM) are a group of glycopeptide antibiotics clinically prescribed for the treatment of selected neoplastic diseases. The BLM-Fe(III) complex [139,140] which has a characteristic Fe-N(amide) bond, obtained at pH 7 is in the low-spin form; a decrease of the pH down to 4 converts it in a high-spin species. It has also been demonstrated that at pH 4 the high-spin BLM-Fe(III) species can be converted to a low-spin species by addition of various monodentate axial ligands.[139]

The definitive characterization of low-molecular-weight synthetic complexes[141], which are frequently amenable to more detailed scrutiny than the natural systems, provides a structural framework for understanding the changes of spin state and oxidation state in the natural systems.

Within the class of six-coordinate complexes trans-$[Fe^{III}LX_2]$, with L = a neutral or a dinegative tetradentate N_4 ligand (excluding porphyrins and phthalocyanins) and X = a neutral or an uninegative monodentate axial ligand, only a very limited number of molecules have been described with spin-state of either high-spin or low-spin (Table 3.1).[142-150] However, when L is dinegative only a handful of three complexes are

Table 3.1 : Iron(III) Complexes of Tetradentate N_4 Non-porphyrin Equatorial Ligands.

Complexes	Comments	Reference
$[Fe^{III}(25)X_2]^+$ X= Cl^-, Br^-, and NCS^-	Hexacoordinated iron(III) low-spin complex with neutral in-plane ligand. Axially bromo ligated complex is high-low spin equilibrium. IR, far IR, solid-state reflectance spectra, and magnetic moment.	105
$[Fe^{III}(29)X_2]^{3+/1+}$ X= MeCN, Cl^-, and SCN^-	Hexacoordinated iron(III) low-spin complex with neutral in-plane ligand. Absorption spectra, magnetism, and reactivity.	142
$[Fe^{III}(30)X_2]^+$ X= Cl^- and Br^-	Hexacoordinated iron(III) high-spin complex with neutral in-plane ligand. Absorption spectra, magnetism, and Mössbauer spectra.	143
$[Fe^{III}(L)Cl_2]^+$ (L)= (31) or (32)	Hexacoordinated iron(III) low-spin complex with neutral in-plane ligand. Absorption spectra and magnetism.	144
$[Fe^{III}(33)(MeOH)(OCH_3)]^{2+}$	Hexacoordinated iron(III) low-spin complex with neutral in-plane ligand. In photoassisted oxidation of MeOH as a catalyst.	145
$[Fe^{III}(33)(X)_2]^+$ X= SCN^-, Cl^-, Br^-, and $PhCH_2^-$	Hexacoordinated iron(III) low-spin complex with neutral in-plane ligand. Magnetism, EPR, and X-ray structure.	146

Cont.

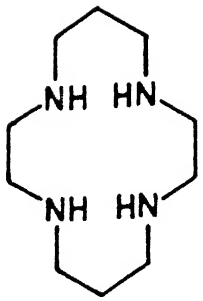

(25)

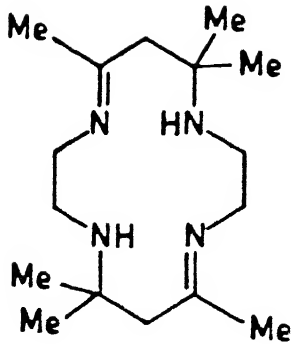

(29)

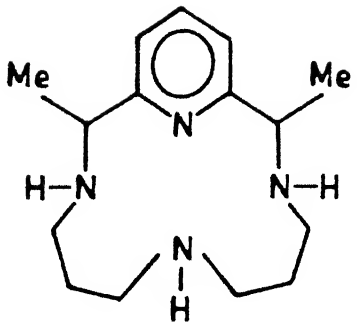

(30)

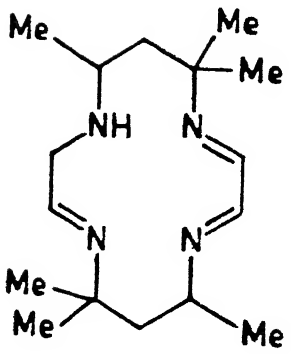

(31)

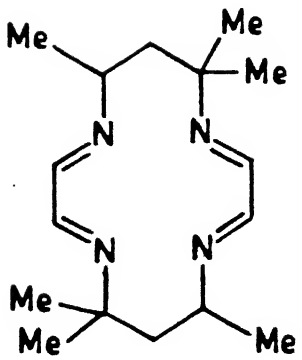

(32)

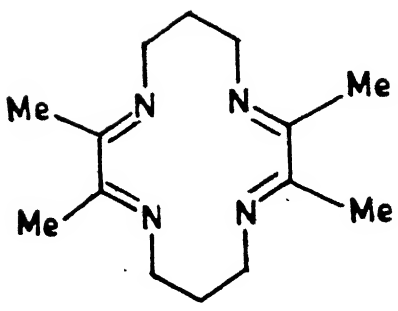

(33)

Complexes	Comments	References
$[Fe^{III}(\mathbf{34})(X)_2]^{+/-}$ X= MeCN, Cl^-, Br^-, and SCN^-	Hexacoordinated iron(III) low-spin complex with dianionic in-plane ligand. Absorption Spectra, EPR, and electrochemistry.	147
$[Fe^{III}(\mathbf{L'})X]$ and $[Fe^{III}(\mathbf{L'})(SPh)(py)]$ $(\mathbf{L'})(2-)$= (**35**), (**36**), and (**37**) X = Cl^-, Br^-, I^-, AcO^-, PhS^-, $PhCH_2S^-$, and $PhCO_2^-$. py = pyridine	Pentacoordinated and hexacoordinated iron(III) complexes. With (**35**) low-spin(S=1/2) as well as intermediate spin (S=3/2). With (**36**) low-spin as well as intermediate spin. With (**37**) high-spin(S=5/2), low-spin, and intermediate spin complexes. Absorption spectra, magnetism, EPR spectra, Mössbauer spectra, and electrochemistry.	148
$[Fe^{III}(\mathbf{L''})_2(A)_2]^+$ $(\mathbf{L''})(2-)$= dimethyl-glyoxime A = imidazole or N-ethylimidazole	Hexacoordinated iron(III) low-spin complexes. EPR spectra, Mössbauer spectra, and magnetism.	149
$[Fe^{III}(\mathbf{38})(im)_2]^+$ im= imidazole	Hexacoordinated iron(III) low-spin complexes. ESR spectra and Mössbauer spectra	150

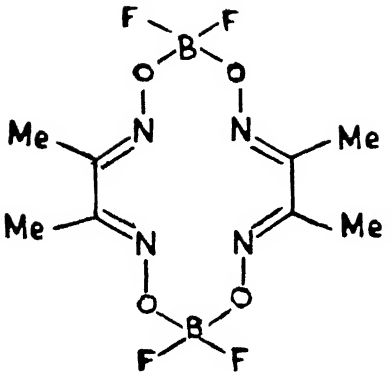
F
F
B
O
O
N
N
Me
Me
Me
Me
N
N
O
O
B
F
F

(34)

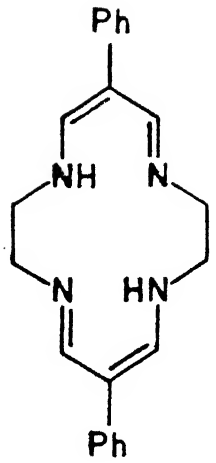
Ph
NH
N
N
HN
Ph

(35)

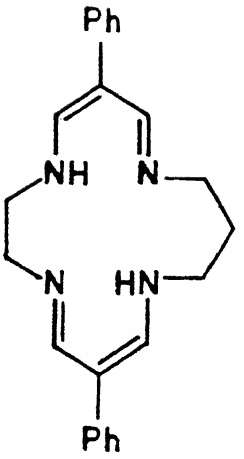
Ph
NH
N
N
HN
Ph

(36)

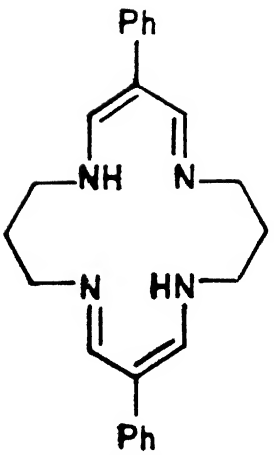
Ph
NH
N
N
HN
Ph

(37)

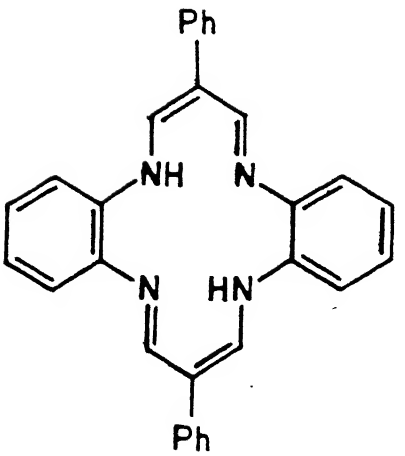
Ph
NH
N
N
HN
Ph

(38)

known and all are low-spin (Table 3.1).[148-150] To date complexes of this class with dinegative open chain tetradentate N_4 ligand system have not been reported to reveal, for a given type of L, change of spin-state phenomena with variation of axial ligands.

In Chapter 2 we have seen that the present ligand system (bpb(2-) or its various ring substituted derivatives) provides a dinegative highly delocalized planar N_4 coordination enviornment similar to porphyrins. Also, axial ligands have pronounced effect on absorption spectra and electrochemical properties of the manganese(III) complexes of the type trans-$[Mn^{III}(L)X]$. In this chapter we describe the syntheses and magnetic and spectroscopic characterization of a series of six-coordinate complexes of the type trans-$[Fe^{III}(L)X_2]^{1+/1-}$ (where L(2-) = tetradentate N_4 ligand and X = monodentate neutral or monoanionic ligand) and studied the effect of axial ligands on the spin-state of the complexes. The X-ray structure of a representative complex trans-$[Fe^{III}(bpc)(MeCO_2)_2].CHCl_3$ has been determined and the results of that are also discussed in this chapter.

3.1 Experimental Section

3.1.1 Solvents and Reagents

Triethylamine was dried by distillation over KOH. Acetonitrile (MeCN) was dried by distillation over CaH_2. For electrochemical experiments further purification was achieved by $KMnO_4$/Li_2CO_3 treatment[151] followed by distillation over P_4O_{10}. Water was distilled twice over alkaline $KMnO_4$. The complex $[Fe(MeCN)_4](ClO_4)_2$ was prepared following the literature procedure.[152] Details of solvent purification and starting

materials other than that stated above are already discussed in Chapter 2 (Section 2.1.1).

3.1.2 Measurements

Variable-temperature magnetic susceptibility measurements were made on powdered samples over the temperature range 40.0 < T < 300 K by the Faraday method using a locally built susceptometer in Professor S. Mitra's laboratory, Chemical Physics Group, Tata Institute of Fundamental Research (TIFR), Bombay, India. The measurements were started at ~ 40.0 K and the sample was heated and held at the desired temperature during the measurement. This process was continued until the sample was attained at room temperature. Effective magnetic moments were calculated from $\mu_{eff} = 2.828\ [\chi_M\ T]^{1/2}$, where χ_M is the corrected molar susceptibility. Diamagnetic corrections were made for the sample holder and for the diamagnetic contribution of the complex being measured. All measurements were made at a fixed field strength and field dependence of the magnetic susceptibility was not studied.

For ^{57}Fe Mössbauer spectroscopy, γ-ray resonance spectra were obtained in the laboratory of Dr. A. K. Nigam, Low-Temperature Physics Group, TIFR, India by using a standard, constant-acceleration spectrometer calibrated with metallic iron at room temperature. All isomer shifts are reported with respect to the room-temperature Fe(0) transmission spectrum. The observed spectra were computer-fitted to Lorentzian lines employing a least-squares minimization technique.

The instrumental details for other measurements are already stated in Chapter 2 (Section 2.1.2).

3.1.3 X-ray Data Collection and Structure Solution and Refinement

The single crystals suitable for X-ray diffraction studies were grown by slow evaporation of a dilute solution of the complex in 1:4 (v/v) mixture of chloroform/n-hexane for two days. Red plate like crystals of $(Et_4N)[Fe(bpc)(MeCO_2)_2].CHCl_3$ having approximate dimentions 0.25 x 0.35 x 0.40 mm^3 was mounted on a glass fiber in a random orientation. Preliminary examination and data collection were performed with Mo Kα radiation (λ = 0.70930) on an Enraf-Nonius CAD-4 computer controlled kappa axis diffractometer equipped with a graphite crystal, incident beam monochromator. Diffraction data at 23°C were collected at University of Louisville, Louisville, Kentucky.

Cell constants and the orientation matrix for data collection were obtained from least-squares refinement, using the setting angles of 25 reflections in the range 13 < θ < 18°, measured by the computer controlled diagonal slit method of centering. The monoclinic cell parameters and calculated volume are: a = 12.283(3), b = 18.819(3), c = 16.437(3) Å, β = 101.02 (2)°, V = 3729.5 $Å^3$. For Z = 4 and formula weight = 808.78 the calculated density is 1.44 g/cm^3. Crystal data, data collection, and refinement parameters are summarized in Table 3.2. As a check on crystal quality, omega scans of several intense reflections were measured; the width at half-height was 0.50° with a take-off angle of 2.8°, indicating moderate crystal quality. From the systematic absences of:

h0l l=2n

0k0 k=2n

Table 3.2 Summary of X-ray Diffraction Data for $(Et_4N)[Fe(bpc)(MeCO_2)_2]\cdot CHCl_3$

formula	$C_{31}\ H_{37}\ Cl_5\ Fe\ N_5\ O_6$
formula weight	808.78
crystal system	monoclinic
space group	P21/c
a, Å	12.283 (3)
b, Å	18.819 (3)
c, Å	16.437 (3)
β, deg	101.02 (2)
Z	4
V, $Å^3$	3729.5
d_{calcd}, g/cm^3	1.44
T, °C	23
radiation	Mo Kα (= 0.70930 Å)
abs coeff (μ), cm^{-1}	8.1
total data collected	6914
unique data used ($I>3\sigma(I)$)	6666
no. of params refined	434
$R(E_o)$[a]	0.041
$R_w(E_o)$[b]	0.041
quality-of-fit indicator[c]	

[a] $R = \Sigma\ E_o\ \ E_c\ / \Sigma\ E_o$. [b] $R_w = [(\ w\ (\ E_o - E_c\ )^2\ /\ \Sigma\ w\ E_o^{\ 2})]^{½}$ where $w = 4\ E_o^{\ 2}\ /\ \sigma^2\ (\ E_o^{\ 2}\ )$ and $\sigma^2\ (E_o^2) = [S^2(C + R^2 \times B) + (p\ E_o^2)^2]/L_p^2$, where S = scan rate, C = total integrated peak count, R = ratio of scan time to background counting time, B = total background count, L_p = Lorentz polarization factor, and p = fudge factor (fixed at 0.03).

[c] quality of fit = $[w(\ E_o - E_c\ )^2/(N_{observns} - N_{parameters})]^{1/2}$.

and from subsequent least-squares refinement, the space group was determined to be $P2_1/c$ (# 14). The scan rate varied from 1 to 3°/min (in omega). The variable scan rate allows rapid data collection for intense reflections where a fast scan rate is used and assures good counting statistics for weak reflections where a slow scan rate is used. Data were collected to a maximum 2θ of 50.0°. The scan width was calculated as follows:

$$\text{scan width} = 0.8 + 0.340 \tan \theta$$

Stationary background counts were recorded on each side of the reflection. The ratio of peak counting time to background counting time was 2:1.

A total of 6914 reflections were collected, of which 6666 were unique and not systematically absent. As a check on crystal and electronic stability three representative reflections were measured every 60 min. The intensities of these standards remained constant within experimental error throughout data collection. No decay correction was applied. An empirical absorption correction, based on a series of psi-scans was applied to the data. Relative transmission coefficients ranged from 0.974 to 1.000 with an average value of 0.983. Intensities were corrected for Lorentz and polarization effect.

Neutral atom scattering factors were taken from the tabulation of Cromer and Waber.[153] Anomalous dispersion effects were included in E_{calc};[154] the values for f′ and f′′ were those of Cromer.[155] A total of 5069 reflections having intensities greater than 3.0 times their standard deviation were used in the refinements. The structure was solved by the direct

methods.[156,157] Subsequent difference Fourier syntheses revealed the positions of the remaining nonhydrogen atoms. The structure was refined by a full-matrix least-squares method with anisotropic thermal parameters used for the non-hydrogen atoms. The function minimized was $\Sigma w(|E_o| - |E_c|)^2$ where E_o and E_c are the observed and calculated structure amplitudes, and the weight, w, is $4E_o^2/\sigma^2(E_o^2)$. The maximum and minimum peaks on the final difference Fourier map corresponded to 0.48 and -0.41 e /Å^3, respectively. All calculations were performed using the SDP/VAX[158] crystallographic software package of Enraf-Nonius & B. A. Frenz & Associates, Inc., for the structural calculations and the programs PLUTO[159] and ORTEP[160] for the molecular and structural drawings. The final weighted R factor(on E) was 0.041 nd the unweighted R factor was 0.041.

3.2 Syntheses of Ligands

The details of ligand syntheses are given in Chapter 2 (Section 2.2).

3.3 Syntheses of Complexes

All the complexes were synthesized for the first time. Very recently Valentine and coworkers[161] reported the synthesis and X-ray structure of $(Et_3NH)[Fe(bpb)Cl_2].MeCN$, but the complex is reported to be very moisture sensitive and all manipulations were performed under an argon atmosphere. However, we empolyed a different methodology and also used substituted ligands and the complexes obtained in the present study are sufficiently stable even in air. The detailed syntheses are given below.

3.3.1 $[Fe(bpb)(C_5H_5N)_2]ClO_4$

A solution of $Fe(MeCN)_4(ClO_4)_2$ (1.33 g, 3.18 mmol) in MeCN (10 mL) was slowly added to a solution containing $H_2(bpb)$ (1.00 g, 3.16 mmol) and pyridine (1.01 mL, 12.55 mmol) in MeCN (20 mL). The resulting deep reddish brown solution was stirred for 1 h and cooled in the refrigerator. A reddish brown crystalline precipitate formed was filtered and washed with ~ 1mL of MeCN and dried in vacuo (yield, 1.6 g, ~80%).

3.3.2 $Na[Fe(bpb)(CN)_2]$

The complex $[Fe(bpb)(C_5H_5N)_2]ClO_4$ (0.11 g, 0.18 mmol) and NaCN (0.10 g, 2.04 mmol) were stirred in ethanol (10 mL) for 2 h. The reddish brown suspension of $[Fe(bpb)(C_5H_5N)_2]ClO_4$ immediately dissolved to generate a deep green solution and dark green crystals started separating out within 15 min. The product and excess NaCN mixture were filtered, washed with ethanol. The solid was redissolved in DMF, filtered to remove excess NaCN and solvent evaporated under reduced pressure. The residue dissolved in ethanol (5 mL) and dry et er (5 mL) was added to it. The solution gives dark green (almost black) crystals after cooling for a day. The product was filtered and dried in vacuo (yield, 0.06 g, ~75 %).

3.3.3 $(Et_4N)[Fe(bpc)Cl_2]$

NEt_4FeCl_4 (0.20 g, 0.61 mmol) in DMF (10 mL) was stirred for 2 min and to it was added solid $H_2(bpc)$ (0.24 g, 0.62 mmol) with stirring. The suspension thus obtained was stirred for 10 min and then 1:10 diluted NEt_3 (1.7 mL, 1.23 mmol) in DMF was added dropwise. The solution immediately turned deep green. It

was warmed on a water bath for 5 min and stirring was continued for 2 h, and then filtered. The resulting solution was evaporated to dryness and 5 mL of MeCN was added. On cooling the product separates out as dark green crystals. The product was filtered and recrystallized from 10 mL MeCN/diethyl ether (yield, 0.17 g, ~43 %). This complex is fairly stable in air.

3.3.4 $(Et_3NH)[Fe(4\text{-}Mebpb)Cl_2]$

This was prepared following a similar procedure as in the case of bpc(2-) analogue starting with H_2(4-Mebpb) (0.35 g, 1.00 mmol) as the starting material. The product was isolated as green crystals (yield, 0.34 g, ~56 %).

3.3.5 $(Et_4N)[Fe(bpc)(MeCO_2)_2].CHCl_3$

Method A: A solution of $Fe(MeCN)_4(ClO_4)_2$ (0.11 g, 0.27 mmol) in DMF (2 mL) was added dropwise to a solution containing H_2(bpc) (0.10 g, 0.26 mmol) and $(Et_4N)(MeCO_2).4H_2O$ (0.28 g, 1.08 mmol) in DMF (5 mL). The solution immediately turned dark brown and was stirred for 1h. The solvent was evaporated under vaccum and MeCN (5 mL) was added. The resulting greenish violet solution gives violet powder on addition of dry diethyl ether (10 mL). The violet powder thus obtained was recrystallized from chloroform/n-hexane to afford reddish violet crystals (yield, 0.10 g, ~55 %). The single crystals suitable for X-ray diffraction studies were grown by slow evaporation of a dilute solution of the complex in 20 mL 1:4 (v/v) mixture of chloroform/n-hexane over a time period of two days.

Method B: Alternatively, it can also be prepared by stirring $(Et_4N)[Fe(bpc)Cl_2$ (0.10 g, 0.15 mmol) with excess NaO_2CMe in MeCN (5 mL) for 24 h. The NaCl that formed was filtered and the filtrate evaporated to dryness giving violet powder (yield, 0.10 g, ~ 95 %). The complex was recrystallized from chloroform / n-hexane.

The products from both the methods gave identical IR and absorption spectra.

3.3.6 $(Et_4N)[Fe(bpb)(CH_3COO)_2].H_2O$

The complex $[Fe(bpb)(C_5H_5N)_2]ClO_4$ (0.52 g, 0.83 mmol) was stirred in MeCN (5 mL). To this stirred solution $(Et_4N)(MeCO_2)$ $4H_2O$ (0.45 g, 1.72 mmol) in MeCN (1 mL) was added dropwise. The solution immediately turned deep green. It was stirred for 1 h, filtered, and concentrated to ~ 3 mL. Dry diethyl ether (1.5 mL) was added to it and the solution was kept in the refrigerator. After 24 h green crystals that formed was filtered, washed with ~ 2 mL of MeCN/diethyl ether (1:2), and dried in vacuo (yield, 0.25 g, ~50 %).

Alternatively, it was prepared following similar procedure as described in the case of bpc(2-) analogue (Section 3.3.5, method A). Both the procedure provides identical complex as is evident from their IR and absorption spectra.

3.4 Results and Discussion

3.4.1 Syntheses and Characterization

The syntheses of mononuclear bis-axially ligated iron(III) complexes are outlined in the following Scheme III.

Scheme III

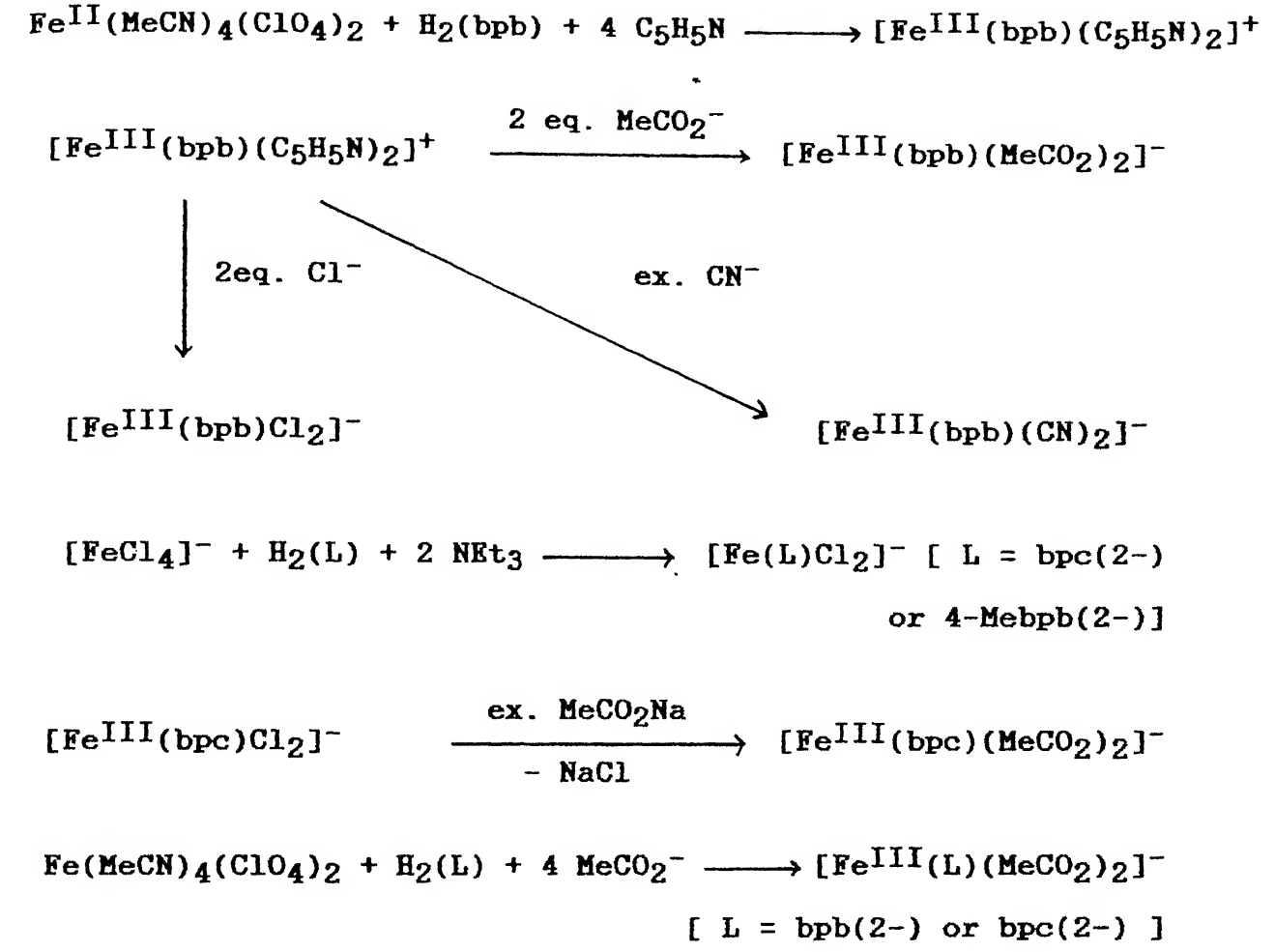

These reactions offer a general route for the syntheses of new iron(III) complexes of types $[Fe(L)X_2]^{1+}$ and $[Fe(L)Y_2]^{1-}$ where L(2-) = bpb(2-), bpc(2-), and 4-Mebpb(2-); X = pyridine, and Y = Cl^-, $MeCO_2^-$, or CN^- .

The new complexes showed no (N-H) IR stretching band in the 3000-3500 cm^{-1} region. The C=O stretching vibrations of the free ligands (Chapter 2, Section 2.2) also shifted towards lower energy in all the complexes (Table 3.3). This indicates that the ligands in these complexes are deprotonated. The IR spectra of the acetate complex of the bpb(2-) ligand shows broad absorbtion

Table 3.3 : Molar Conductance and Selected IR Data of Iron(III) Complexes

Complex	Solvent	Molar conductivity[a] Λ_M (Ω^{-1} cm^2 mol^{-1})	IR data[b] (cm^{-1})		
			γ_{amideI}	$\gamma_{C\equiv N}$	$\gamma_{ClO_4^-}$
$[Fe(bpb)(C_5H_5N)_2]ClO_4$	pyridine	34	1630		1100
	MeCN	120			
$Na[Fe(bpb)(CN)_2]$	DMF	70	1620	2140	
$(Et_4N)[Fe(bpc)Cl_2]$	MeCN	120	1620		
$(Et_3NH)[Fe(4\text{-}Mebpb)Cl_2]$	MeCN	125	1620		
$(Et_4N)[Fe(bpc)(O_2CMe)_2].CHCl_3$	MeCN	120	1600 1620(sh)[d]		
$(Et_4N)[Fe(bpb)(O_2CMe)_2].H_2O$	MeCN	120	1610 1620(sh)[d]		

a Expected 1:1 electrolyte range: 65-90 Ω^{-1} cm^{2}mol^{-1} in DMF; 120-180 Ω^{-1} cm^2 mol^{-1} in MeCN.[123]

c In KBr disk (4000-600 cm^{-1}).

d For acetate complexes $\gamma_{C=O}$ as well as γ_{amide} gives closely seperated one shoulder and one strong peak. sh= shoulder.

~ 3400 cm^{-1} indicating the presence of water in this complex. The acetate complexes show both $\nu_{C=O}$ for acetate and $\nu_{amide\ I}$ stretching vibration ~ 1600 cm^{-1} as a strong peak with a shoulder (Table 3.3). This shoulder is absent in other complexes. The complex $[Fe(bpb)(C_5H_5N)_2]ClO_4$ shows characteristic perchlorate bands at 1100 cm^{-1} and at 620 cm^{-1}.[122] In the cyanide complex $\nu_{C\equiv N}$ vibration absorbs at 2140 cm^{-1}, whereas free cyanide absorbs at 2080 cm^{-1}. This shift towards higher energy upon coordination indicates that the cyanide groups act as σ-donor (see below) rather than as π-acceptor.[122] The following resonating structures show that when cyanide binds as a primarily

$$\underset{\sigma\text{-donor}}{M{-}\!\!-C{\equiv}N:} \longleftrightarrow \underset{\pi\text{-acceptor}}{\overset{+}{M}{=}C{=}\overset{-}{N}:}$$

σ-donor the triple bond character increases. On the other hand, increasing π-back donation weakens the triple bond character.[122]

Electrical conductivity data show 1:1 electrolytic nature of all the complexes in solution (Table 3.3). Based on the above facts and analytical data (Table 3.4) we propose the formulation of the new complexes as formulated in the Table 3.4. It is to be noted that the X-ray structure of $(Et_3NH)[Fe(bpb)Cl_2].CH_3CN$ which was used as a catalyst in the olefin epoxidation by PhIO, has recently been reported in the literature.[161] The remarkable stability of the present complexes demands special attention given the reported moisture sensitivity of $[Fe(bpb)Cl_2]^-$.[161]

3.4.2 Magnetism

To determine the spin-state of the complexes we measured the magnetic susceptibilities of the complexes in solution (Evans'

Table 3.4 : Microanalytical Data[a] of Iron(III) Complexes

Complex	Empirical Formula	% C	% H	% N
$[Fe(bpb)(C_5H_5N)_2]ClO_4$	$C_{28}H_{22}N_6O_6FeCl$	53.70 (53.40)	3.65 (3.52)	13.15 (13.34)
$Na[Fe(bpb)(CN)_2]$	$C_{20}H_{12}N_6O_2NaFe$	53.90 (53.69)	3.00 (2.68)	18.60 (18.79)
$(Et_4N)[Fe(bpc)(Cl)_2]$	$C_{26}H_{30}N_5O_2Cl_4Fe$	48.85 (48.62)	5.10 (4.71)	10.80 (10.90)
$(Et_3NH)[Fe(4\text{-}Mebpb)Cl_2]$	$C_{26}H_{32}N_5O_2Cl_2Fe$	54.30 (54.46)	5.40 (5.62)	12.10 (12.21)
$(Et_4N)[Fe(bpc)(MeCO_2)_2].CHCl_3$	$C_{31}H_{37}N_5O_6Cl_5Fe$	46.50 (46.03)	5.00 (4.61)	8.90 (8.65)
$(Et_4N)[Fe(bpb)(MeCO_2)_2].H_2O$	$C_{30}H_{40}N_5O_7Fe$	56.60 (56.43)	5.90 (6.31)	10.70 (10.97)

[a] Values in parentheses are calculated ones

method)[111] as well as in the solid state. The results are given in Table 3.5. At ambient temperature, the effective magnetic moment of low-spin iron(III) lies in the range 2.0-2.6 μ_B.[162] The doublet ground state gives rise to higher magnetic moment (>1.73 μ_B) due to orbital contribution.[163] The magnetic moment data of the complex $[Fe(bpb)(C_5H_5N)_2]ClO_4$ in solution as well as in the solid state (~2.5 μ_B) show that the complex is low-spin in nature (Table 3.5). The solution magnetic moment of $Na[bpb(CN)_2]$ agrees well with its low-spin behavior (Table 3.5). The axially ligated chloro or acetato complexes show magnetic moment values ~ 5.90 μ_B in the solid state as well as in solution (Table 3.5), confirming the high-spin (S= 5/2) nature of these complexes.

In order to substantiate the spin-state of the complexes, variable-temperature solid state magnetic susceptibility studies on three representative complexes were performed using Faraday method on powdered samples in the range 40-300 K. For the complexes $(Et_4N)[Fe(bpc)(MeCO_2)_2].CHCl_3$ and $(Et_3NH)[Fe(4\text{-}Mebpb)\text{-}Cl_2]$ the μ_{eff} values remain constant over the temperature range, consistent with $^6A_1$ ground state(Tables 3.6-3.7; Figure 3.1). The χ_M^{-1} vs. T plot of these two complexes are linear as expected (Figure 3.1). The Weiss constant θ (in degree) and Curie constant C (in emu-K mol^{-1}) are calculated from the plots. The θ and C values for $(Et_4N)[Fe(bpc)(MeCO_2)_2].CHCl_3$ and $(Et_3NH)[Fe(4\text{-}Mebpb)Cl_2]$ are found to be 5.576(θ), 4.570(C) and 1.457(θ), 4.253(C) respectively. These values are in good agreement with the θ values calculated for known magnetically dilute iron(III) high-spin complexes ($-7 \leq \theta \leq 5$).[164] The behavior of [Fe(bpb)-

Table 3.5 Room Temperature Magnetic Moment[a] of the Iron(III) Complexes

Complexes	Solvent	Concentration (10^{-3} M)	$\mu_{eff}(\mu_B)$	
			Solution	Solid state
[Fe(bpb)$(C_5H_5N)_2$]ClO_4	pyridine	7.5	2.50	2.44
Na[Fe(bpb)$(CN)_2$]	DMF	4.20	2.10	b
(Et_4N)[Fe(bpc)$(Cl)_2$]	MeCN	4.05	5.90	5.96
(Et_3NH)[Fe(4-Mebpb)Cl_2]	MeCN	1.22[c]	5.90	5.86
(Et_4N)[Fe(bpc)$(MeCO_2)_2$] .$CHCl_3$	MeCN	10.60	5.90	5.99
(Et_4N)[Fe(bpb)$(MeCO_2)_2$] .H_2O	MeCN	10.00	5.86	b

[a] Diamagnetic correction values were taken from Ref.114.

[b] not done.

[c] Due to poor solubility of the complex in MeCN higher concentration could not be achieved.

Table 3.6 Variable Temperature Magnetic Susceptibility Data for $(Et_4N)[Fe(bpc)(MeCO_2)_2].CHCl_3$

T (K)	X_M^{-1} (cm^{-3} mol)	μ_{eff} (BM)	T (K)	X_M^{-1} (cm^{-3} mol)	μ_{eff} (BM)
300	6.689x10	5.99	140	3.187x10	5.93
275	6.196x10	5.95	120	2.801x10	5.86
250	5.583x10	5.99	100	2.374x10	5.81
225	5.859x10	6.09	81	1.863x10	5.89
200	4.519x10	5.95	62	1.467x10	5.82
180	4.119x10	5.91	52	1.274x10	5.72
160	3.650x10	5.92	42	9.180	6.06

Table 3.7 Variable Temperature Magnetic Susceptibility Data for $(Et_3NH)[Fe(4\text{-}Mebpb)Cl_2]$

T (K)	X_M^{-1} (cm^{-3} mol)	μ_{eff} (BM)	T (K)	X_M^{-1} (cm^{-3} mol)	μ_{eff} (BM)
300	6.984x10	5.86	140	3.317x10	5.81
275	6.458x10	5.84	120	2.807x10	5.85
250	5.830x10	5.86	100	2.332x10	5.86
225	5.217x10	5.88	81	1.895x10	5.84
200	4.688x10	5.85	62	1.396x10	5.95
180	4.215x10	5.85	52	1.149x10	6.02
160	3.717x10	5.87	42	8.710	6.22

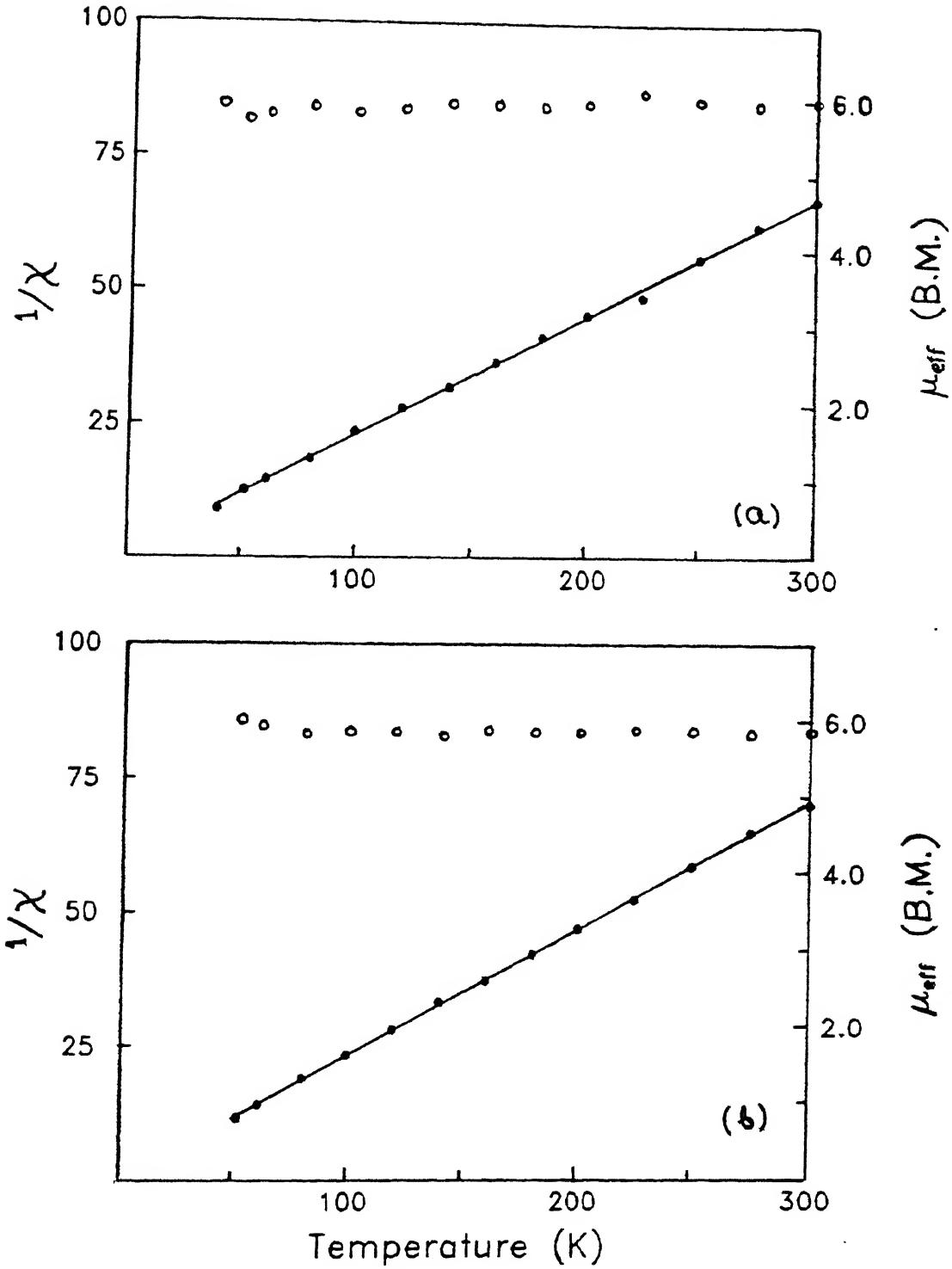

Figure 3.1 Temperature dependencies of the inverse magnetic susceptibilities (•) and effective magnetic moments (o) of (a) $(Et_4N)[Fe(bpc)(MeCO_2)_2].CHCl_3$ and (b) $(Et_3NH)[Fe(4\text{-}Mebpb)Cl_2]$.

$(C_5H_5N)_2]ClO_4$ is displayed in Figure 3.2. As the temperature is lowered, the moment decreases towards the spin-only value as expected (Table 3.8).[165] The plot of reciprocal molar susceptibility vs. temperature for this complex (Figure 3.2) follows the Curie law below ~ 200 K and exhibits noticeable deviation from linearity at higher temperatures. Nevertheless, the magnetic data for $[Fe(bpb)(C_5H_5N)_2]ClO_4$ shows that the ground state is a spin doublet.

3.4.3 Mössbauer Studies

The spin states of $[Fe(bpb)(C_5H_5N)_2]ClO_4$, $(Et_4N)[Fe(bpc)(MeCO_2)_2].CHCl_3$, and $(Et_3NH)[Fe(4\text{-}Mebpb)Cl_2]$ are fully corroborated by ^{57}Fe Mössbauer spectral measurements (Figures 3.3-3.5 and Table 3.9). The Mössbauer parameters of $[Fe(bpb)(C_5H_5N)_2]ClO_4$ and $(Et_4N)[Fe(bpc)(MeCO_2)_2].CHCl_3$ are symptomatic of low-spin and high-spin iron(III) respectively (Table 3.9).[166] The Mössbauer spectra of $(Et_3NH)[Fe(4\text{-}Mebpb)Cl_2]$ at 300 K as well as at 77 K are exhibited in Figure 3.5. At both the temperatures a broad singlet with isomer shift of 0.17 mm/s at 300 K and 0.27 mm/s at 77 K are obtained. The observed isomer shifts are in the lower end of the values usually obtained for high-spin six-coordinate iron(III) complexes.[166] Similar spectral feature was observed for the high-spin iron(III) cytochrome P_{450} model complex [Fe(PPIXDME)$(OC_6H_4NO_2)$ [PPIXDME = protoporphyrin IX di-methyl ester) at 77 K.[167]

3.4.4 X-ray Structure of $(Et_4N)[Fe(bpc)(MeCO_2)_2].CHCl_3$

The ORTEP[160] drawing of the anion together with the atom-labeling scheme is shown in Figure 3.6. Table 3.10 contains the

Table 3.8 Variable Temperature Magnetic Susceptibility Data for $[Fe(bpb)(C_5H_5N)_2]ClO_4$

T (K)	X_M^{-1} (cm^{-3} mol)	μ_{eff} (BM)	T (K)	X_M^{-1} (cm^{-3} mol)	μ_{eff} (BM)
300	4.025×10^2	2.44	140	2.111×10^2	2.30
275	3.856×10^2	2.39	120	1.889×10^2	2.25
250	3.556×10^2	2.37	100	1.593×10^2	2.24
225	3.271×10^2	2.35	81	1.304×10^2	2.23
200	2.980×10^2	2.32	62	9.946×10	2.22
180	2.714×10^2	2.30	52	8.351×10	2.23
160	2.443×10^2	2.29	42	6.879×10	2.21

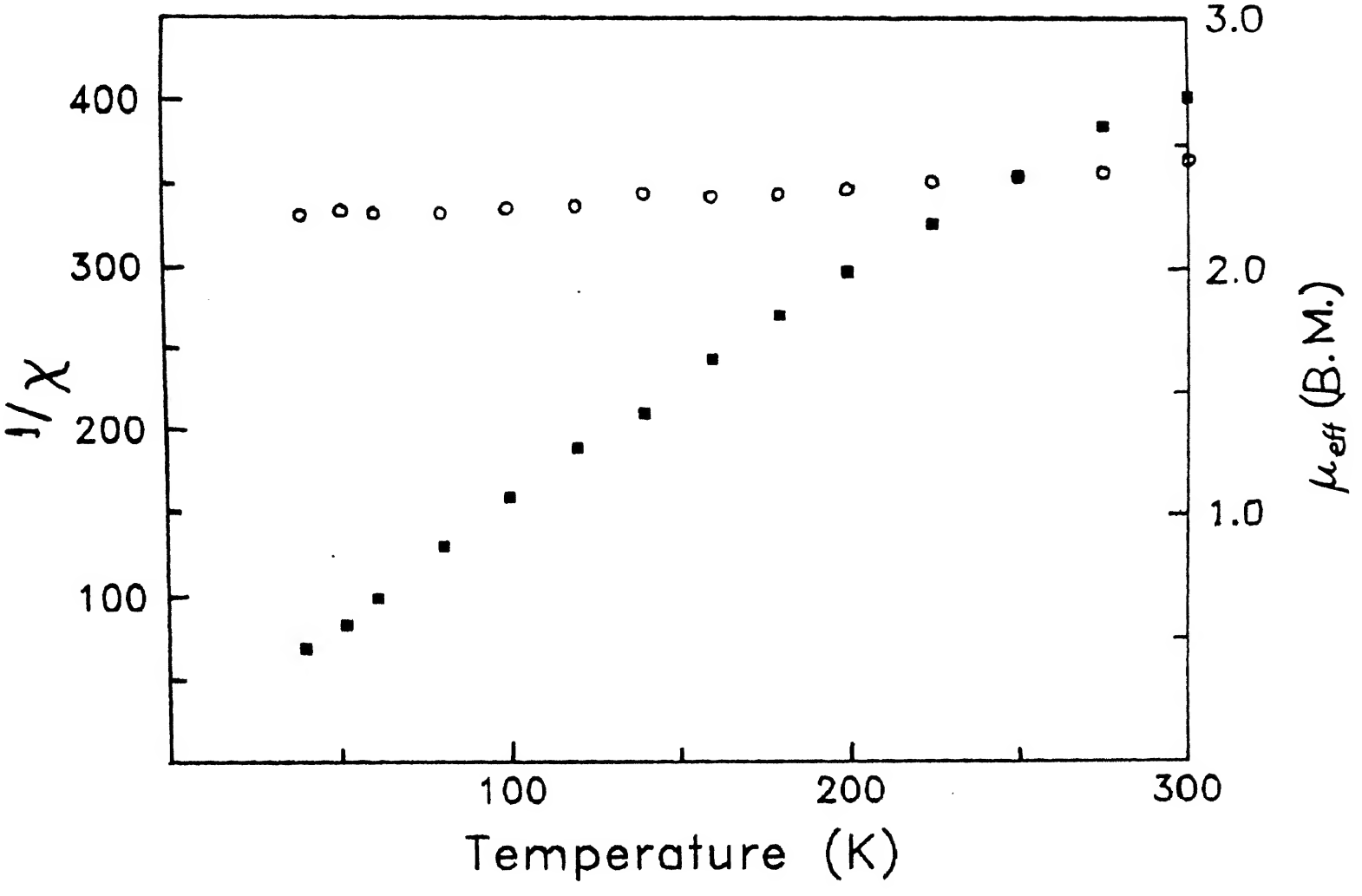

Figure 3.2 Temperature dependencies of the inverse magnetic susceptibilities (■) and effective magnetic moments (o) of $[Fe(bpb)(C_5H_5N)_2]ClO_4$.

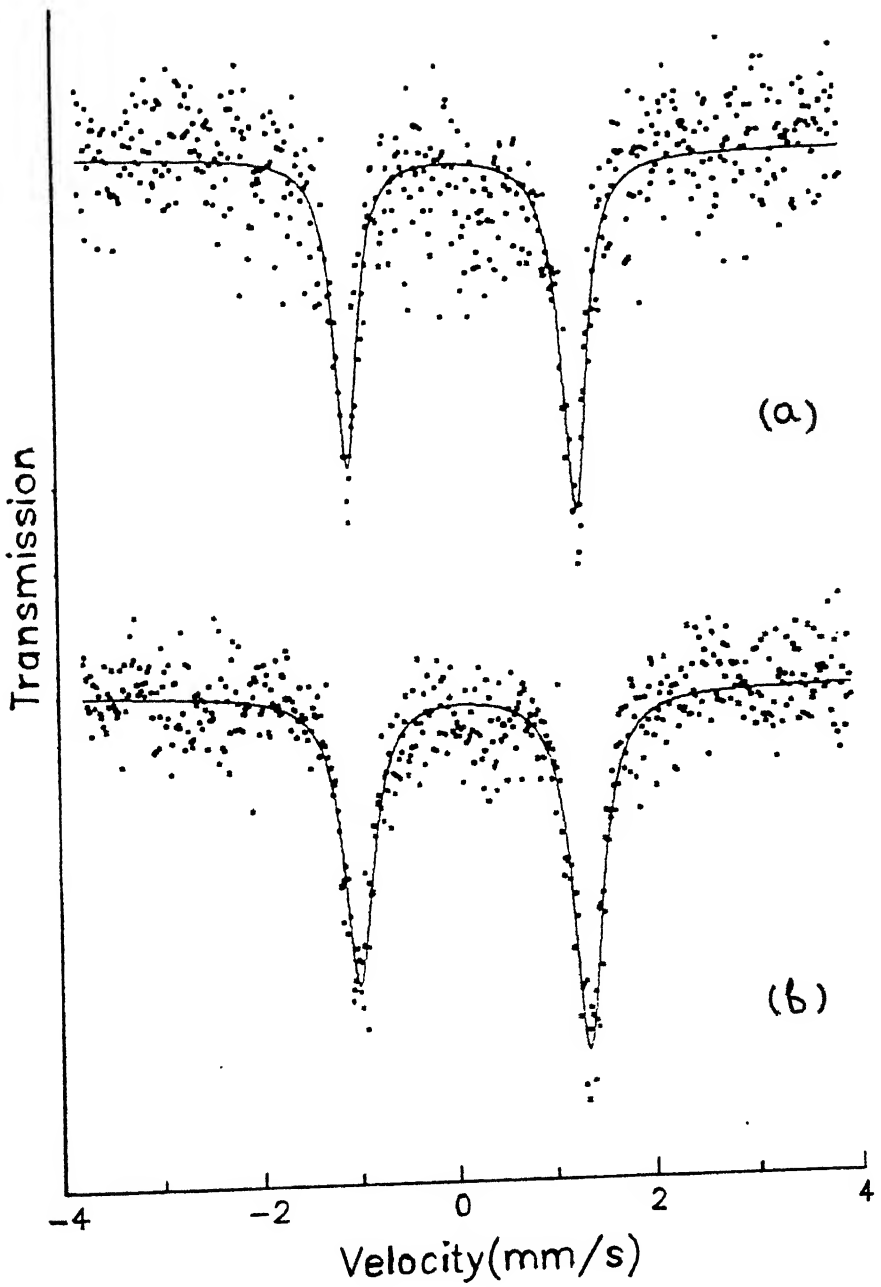

Figure 3.3 Mössbauer spectra of $[Fe(bpb)(C_5H_5N)_2]ClO_4$ at 300 K (a) and 77 K (b).

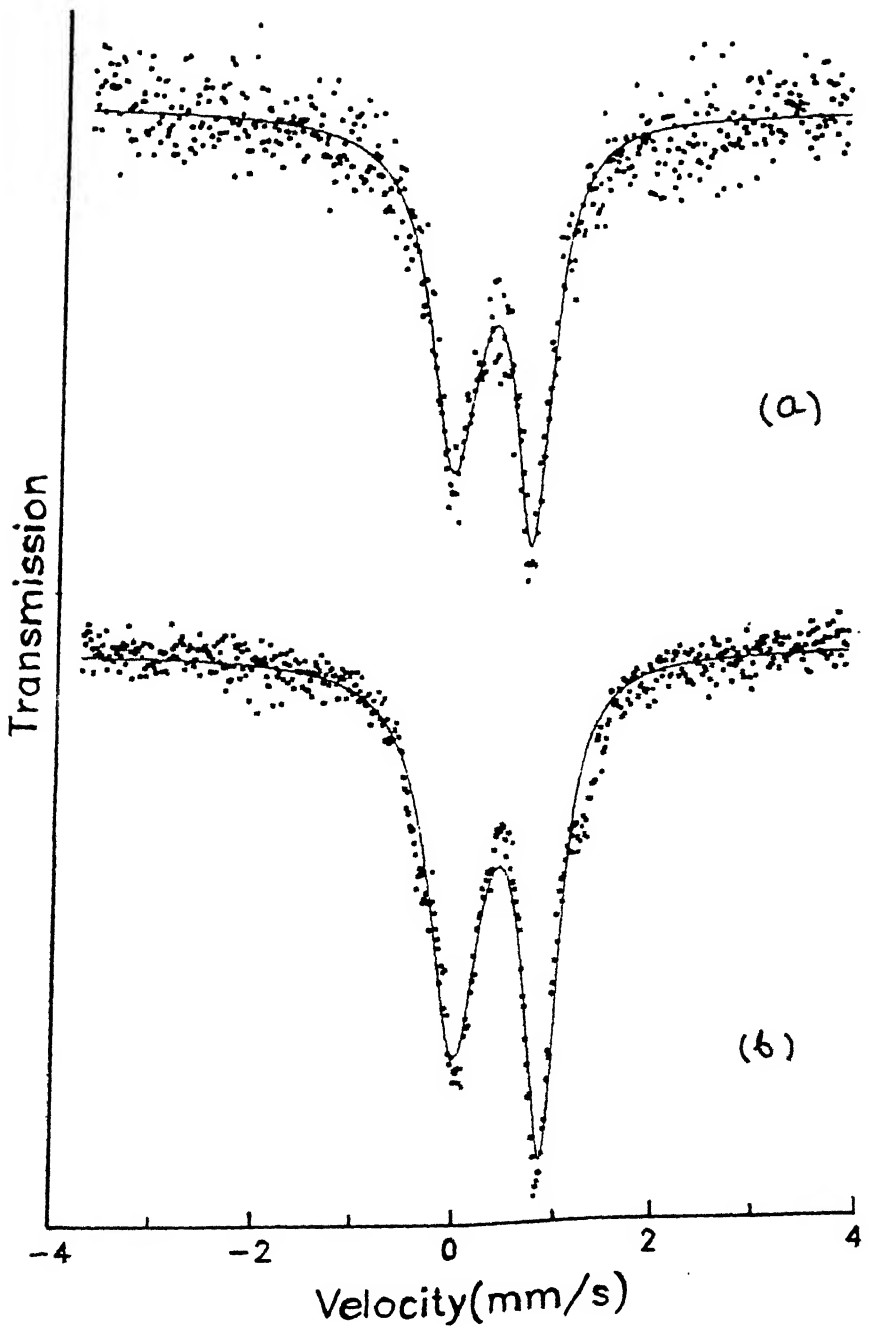

Figure 3.4 Mössbauer spectra of $(Et_4N)[Fe(bpc)(MeCO_2)_2].CHCl_3$ at 300 K (a) and 77 K (b).

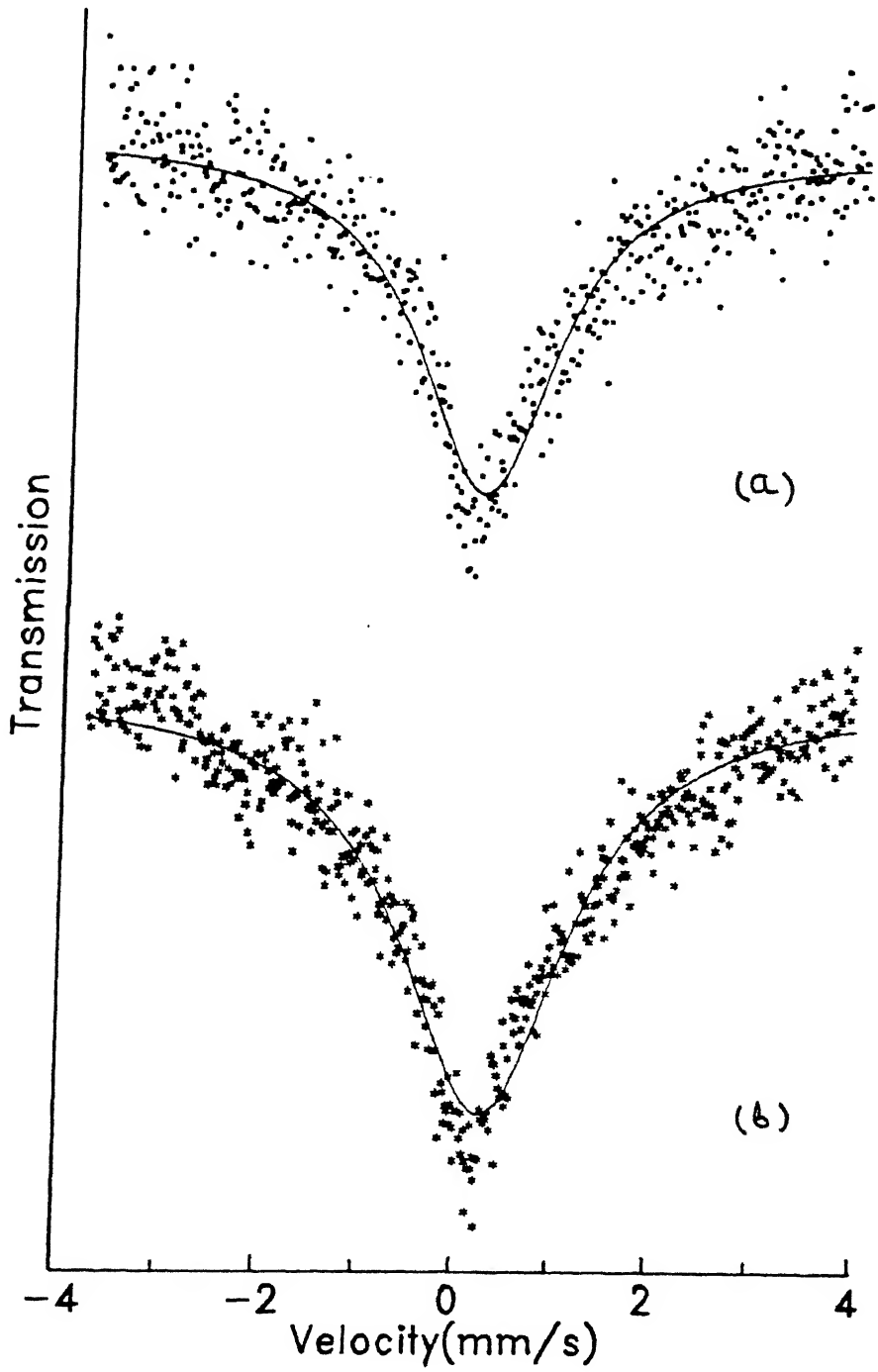

Figure 3.5 Mössbauer spectra of $(Et_3NH)[Fe(4\text{-}Mebpb)Cl_2]$ at 300 K (a) and 77 K (b).

Table 3.9 : Mössbauer Data for Iron(III) Complexes

Complex	T (K)	Spin State	δ (mm s^{-1})	ΔE_Q (mm s^{-1})
$[Fe(bpb)(C_5H_5N)_2]ClO_4$	300	$^2T_2$	0.12	2.36
	77	$^2T_2$	0.18	2.36
$(Et_4N)[Fe(bpc)(MeCO_2)_2].CHCl_3$	300	$^6A_1$	0.35	0.82
	77	$^6A_1$	0.45	0.88
$(Et_3NH)[Fe(4Mebpb)Cl_2]$	300	$^6A_1$	0.17	0.0
	77	$^6A_1$	0.27	0.0

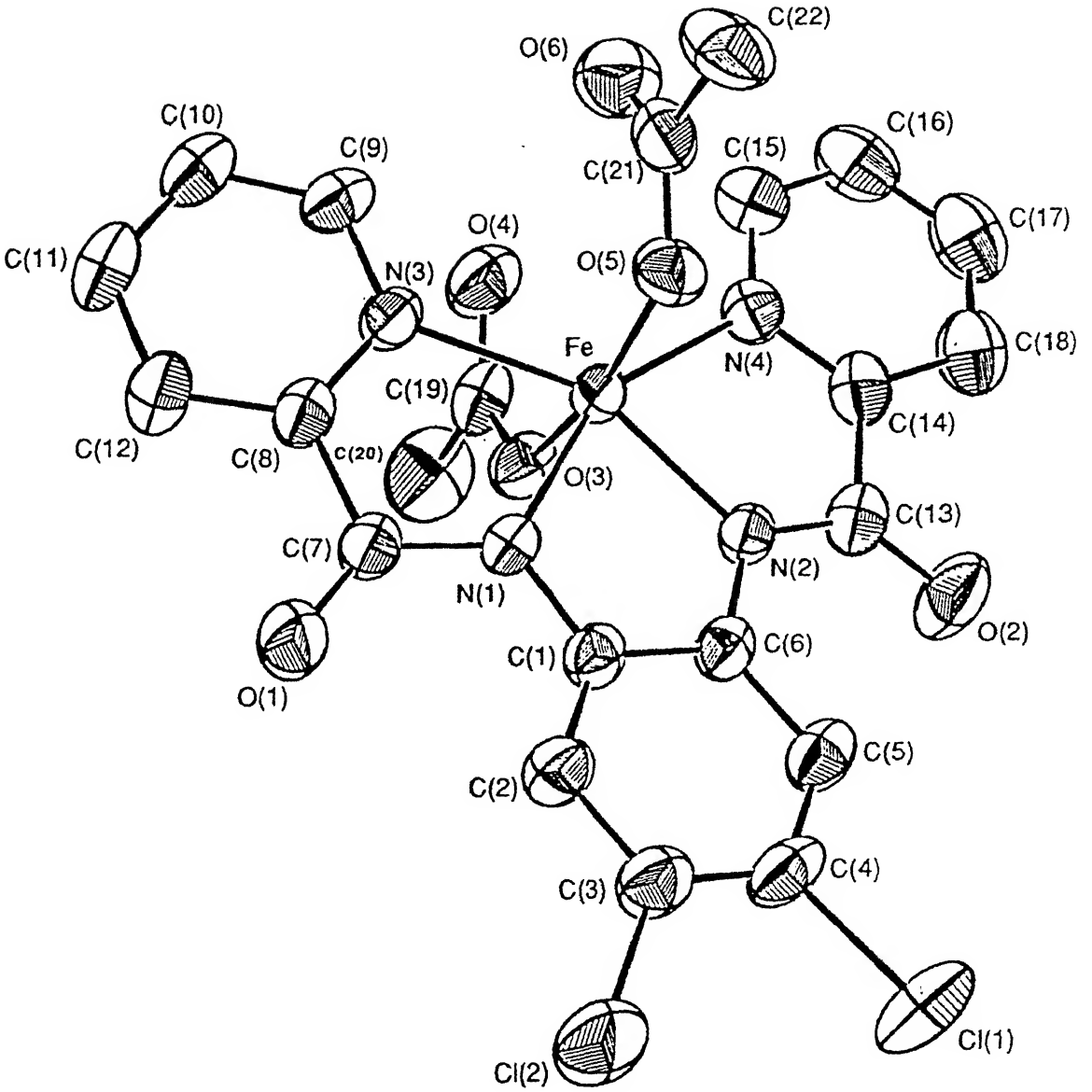

Figure 3.6 Crystal structure of $(Et_4N)[Fe(bpc)(MeCO_2)_2].CHCl_3$ showing the atom-labeling scheme.

Table 3.10: Selected Intramolecular Bond Lengths (Å) and Angles (deg) for $(Et_4N)[Fe(bpc)(MeCO_2)_2].CHCl_3$[a]

Bond distance		Bond Angle	
Fe-N1	2.061(2)	N1-Fe-N2	77.20(9)
Fe-N2	2.067(2)	N2-Fe-N4	76.12(9)
Fe-N3	2.205(2)	N3-Fe-N4	131.02(9)
Fe-N4	2.199(3)	N3-Fe-N1	75.60(9)
Fe-O3	1.965(2)	O3-Fe-O5	166.28(9)
Fe-O4	1.979(2)	N4-Fe-O3	86.53(9)
		N4-Fe-O5	87.82(9)
		N2-Fe-O3	95.85(9)
		N2-Fe-O5	94.91(9)

[a] Estimated standard deviations in parentheses.

selected bond distances and the bond angles of the anion. Details of bond distances, bond angles, positional and isotropic thermal parameters are listed in Tables I-VIII(Appendix).

The iron atom sits in the mean plane of the four N atoms of the planar bpb(2-) ligand. Axially coordinated two acetate ions are almost perpendicular (the dihedral angle between the benzene ring and the plane containing two acetates is 89.80°) to the bpb(2-) plane giving rise to a C_{2v} metal site symmetry.

Table 3.11 lists selected iron-N(py) and iron-N(amide) bond distances. The iron-N(amide) bond distance of the octahedral low-spin iron(III) complex $[Fe(\mathbf{18a})_2]Cl.H_2O$[48] is significantly shorter (0.09 A) than that of the present complex. This is possibly due to the smaller size of the low-spin iron(III) center in the former complex. However, the iron-N(amide) distance in high-spin iron(III) complex $(Et_3NH)[Fe(bpb)Cl_2].MeCN$[161] is only 0.03 A shorter than that of the present one. This small increase in bond distance in $(Et_4N)[Fe(bpc)(MeCO_2)_2].CHCl_3$ indicates the weaker coordinating behavior of bpc(2-) compared to bpb(2-) due to the presence of two chloro substituents in the benzene ring. The ~ 0.02 A longer iron-N(py) bond compared to that in (Et_3NH)-$[Fe(bpb)Cl_2].MeCN$[161] also supports the weaker coordinating ability of bpc(2-) over bpb(2-).

Average iron-N(py) bond distance in the present complex, $(Et_4N)[Fe(bpc)(MeCO_2)_2].CHCl_3$ is 2.205 A, whereas the same in high-spin iron(III) complex $(H_5O_2)[Fe(dipic)_2]$ vary between 2.0037 A to 2.0076 A.[168] This large difference arises from the increased strain exerted by bpb(2-) ligand. This is also evident

able 3.11: Comparison of Fe-N(py), Fe-N(amide), and Fe-O(acetate) Distances in Iron(III) Complexes

Complexes	Spin-states	Fe-N(py) (Å)	Fe-N(amide) (Å)	Fe-O(acetate) (Å)	Ref
$Et_4N)[Fe(bpc)(MeCO_2)_2]$ $.CHCl_3$	h.s.	2.205 2.199	2.061 2.067	1.965 1.979	This work
$Et_3NH)[Fe(bpb)Cl_2]$ .MeCN	h.s.	2.178 2.173	2.037 2.047	-	161
$H_5O_2)[Fe(dipic)_2]$	h.s.	2.003 2.007	-	2.035 2.005	168
b[Fe(OH_2)(EDTA)].H_2O	h.s.	-	-	1.993 2.078	169
$Fe(18a)_2]Cl.\ 2\ H_2O$	l.s.	1.981 1.983	1.957 1.958	-	48
$Fe(phen)_3](ClO_4)_3.H_2O$	l.s.	1.973	-	-	48

lipic = Pyridine 2,6-dicarboxylic acid dianion; EDTA = 1,2 -diaminoethane - N, N´-etraacetic acid tetraanion; the ligand structure of (18a) has been given in p.12 ; phen = 1,10-o-phenanthroline.

in the case of N(py)-Fe-N(py) angle, which deviates from 90° (perfect octahedron) to 131.02 ° in the present case. The ligand geometry in the present case is such that pyridine nitrogens are unable to come closer to the metal center and hence the longer Fe-N(py) bond as well as large deviation in N(py)-Fe-N(py) angle observed here. This type of deviation in N(py)-Fe-N(py) angle is also present in copper, rhodium, and cobalt complexes with bpb(2-) ligand.[56,60,62]

The average axial Fe-O(acetate) bond length is 0.20 Å shorter than the Fe-Cl bond of $(Et_3NH)[Fe(bpb)Cl_2].MeCN$. The Fe-O(acetate) bonds in $Rb[Fe(OH_2)(EDTA)].H_2O$[169] (EDTA = 1,2-diaminoethane-N,N′-tetraacetic acid) vary between 1.993 Å and 2.078 Å. In the present complex the Fe-O(acetate) bond length is 1.965 Å. The shorter Fe-O(acetate) bond length in the present complex indicates the greater influence of the axial acetate ligands than that in the in-plane ligand. This increased interaction in the axial positions may be one of the factors which causes longer in-plane bond lengths.

3.4.5 Absorption Spectra

Solid state spectra of the complexes were recorded in nujol mull. The absorption spectral behavior in the solution phase was also investigated. Representative spectra are shown in Figures 3.7-3.9 and the data are listed in Table 3.12. For all the complexes there are considerable shifts in the absorption positions in going from solid to the solution phase (Table 3.12). This is possibly due to solvent induced structural changes. However, the spectral profile and trends within the complexes

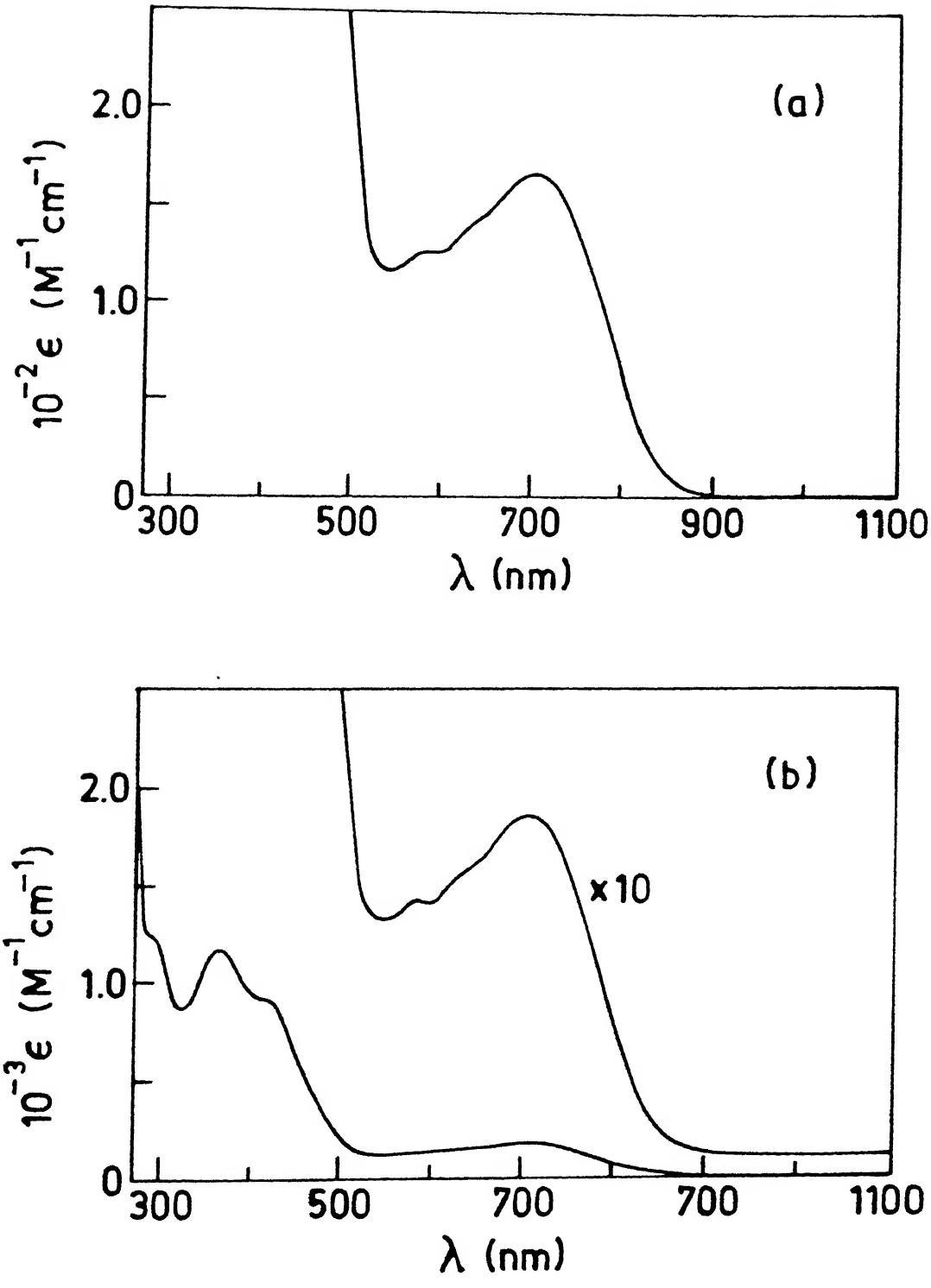

Figure 3.8 Electronic spectra of $Na[Fe(bpb)(CN)_2]$ in DMF for (a) ~ 10^{-3} M (b) ~ 10^{-4} M solution.

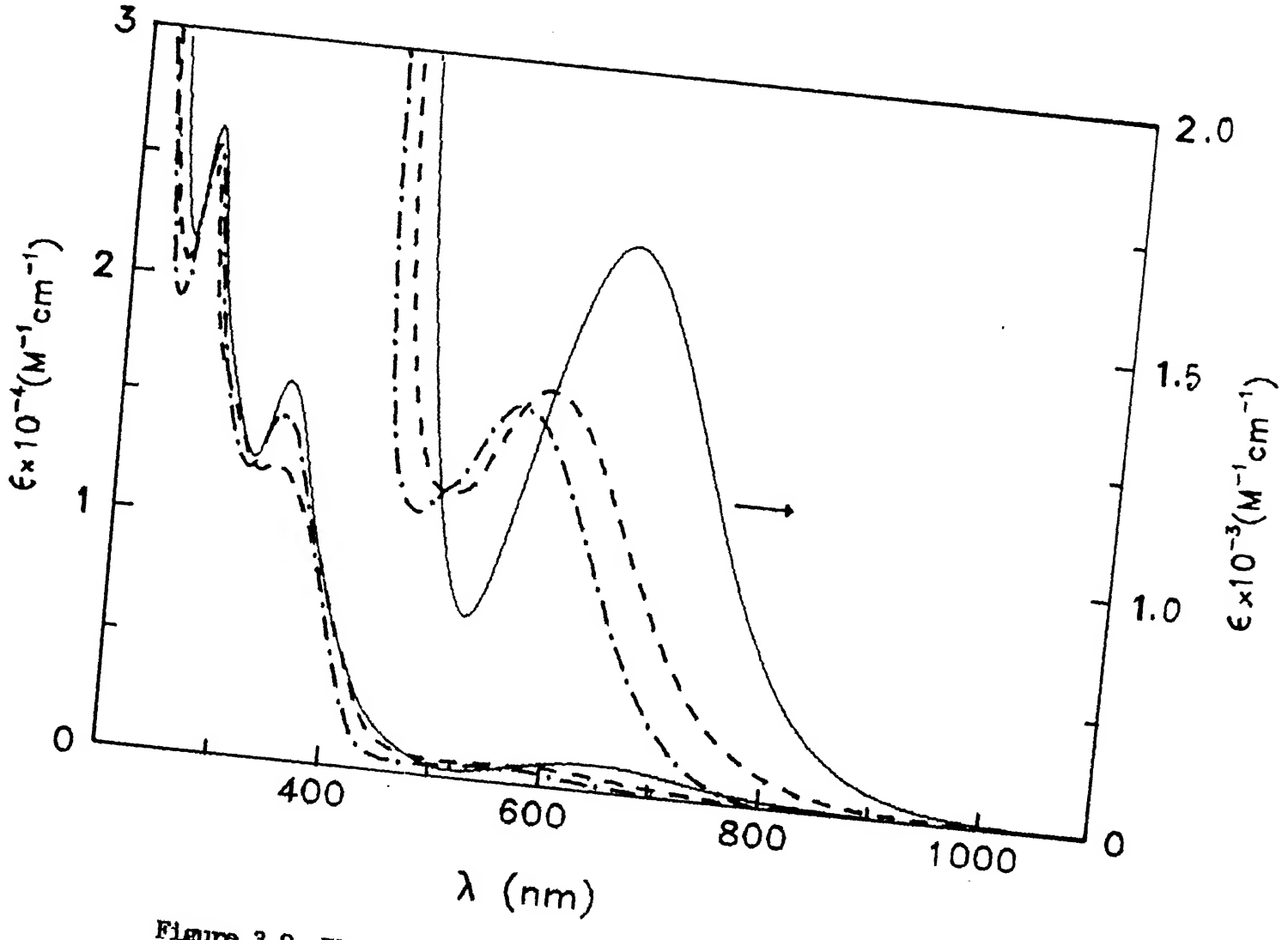

Figure 3.9 Electronic spectra of $(Et_4N)[Fe(bpc)Cl_2]$ (——), $(Et_4N)[Fe(bpb)(MeCO_2)_2].H_2O$ (- - -), and (Et_4N)-$[Fe(bpc)(MeCO_2)_2].CHCl_3$ (-·-·-) in MeCN.

Table 3.12 : Electronic Spectral[a] Data for the Iron(III) Complexes

Complex	Solvent	λ_{max},nm,(ϵ, M^{-1}, cm^{-1})
$[Fe(bpb)(C_5H_5N)_2]ClO_4$	solid[b]	915, 820(sh)[c], 590(sh), 450(sh)
	Pyridine	780(950), 510(sh)(1 800), 350(sh)(9 800)
$Na[Fe(bpb)(CN)_2]$	solid[b]	800, 615(sh), 570(sh), 475(sh), 430
	DMF	702(1 700), 630(sh)(1 400), 579(1 300), 480(sh)(3 100), 415(sh)(8 200),361(10 500), 285(sh)(11 000)
$(Et_4N)[Fe(bpc)(Cl)_2]$	solid[b]	710, 480, 390
	MeCN	650(1 150), 350(15 800), 300(sh)(16 400), 270(26 200) 230(sh)(31 300)
$(Et_3NH)[Fe(4\text{-}Mebpb)Cl_2]$	solid[b]	715, 500(sh), 400
	MeCN	679(900), 347(10 800), 299(sh)(12 700), 266(19 400)
$(Et_4N)[Fe(bpc)(MeCO_2)_2].CHCl_3$	solid[b]	580(sh), 390
	MeCN	560(800), 345(14 400), 270(25 400)
$(Et_4N)[Fe(bpb)(MeCO_2)_2].H_2O$	solid[b]	618, 430
	MeCN	585(850), 345(12 200), 265(23 000), 221(24 200)

[a] Spectral measurements in the range 500-1100nm were made at ~ 10^{-3} M and for the range 200-500nm were made at ~ 10^{-4} M.

[b] Solid spectra were taken in Nujol mull. Scan range 300-1100 nm.

[c] sh = shoulder.

remain intact in solution (see below). It is to be noted that these low energy transitions are of charge-transfer origin (see below) and hence are expected to be purturbed by the polarity of solvents.

All the complexes show in the solid state and in solution phase intense absorptions in the visible region (Table 3.12), which are probably due to ligand-to-metal charge-transfer (LMCT) transitions, expected in the case of iron(III) complexes with oxidizable ligands. In addition to this all the complexes show very intense absorptions in the UV region possibly due to intra-ligand transitions. Similar absorptions in the UV region were also observed in the case of manganese(III) complexes (Chapter 2).

The low energy absorption in low-spin complexes $[Fe(bpb)(C_5H_5N)_2]ClO_4$ and $Na[Fe(bpb)(CN)_2]$ are characteristically red shifted compared to the high-spin complexes (Table 3.12). This could be explained as follows. For a given stereochemistry, in going from a high-spin to a low-spin complex the acceptor orbital will be more stabilized and as a result LMCT transition energies are expected to shift toward lower energy.

Among the high-spin complexes with invariant in-plane ligand the low energy absorptions shift considerably toward higher energies with increase in the field strength of the axial ligand. In the solid state, the complex $(Et_4N)[Fe(bpc)Cl_2]$ shows absorption at 710 nm. However, in the case of $(Et_4N)[Fe(bpc)(MeCO_2)_2].CHCl_3$ the absorption is observed at 580 nm. A shift of 130 nm is clearly observable. On the other hand, the corresponding shift in solution is only 90 nm. This trend also holds good in the case of high-spin bpb(2-) complexes in solution (solid state

absorption data are not available for $[Fe(bpb)Cl_2]^{1-}$ [161]. In solution, for bpb(2-) complexes, changing axial ligands from chloro- (680 nm)[161] to acetate- (585 nm) the low energy absorption positions are blue shifted (a shift of 95 nm). In contrast, keeping the axial ligands fixed, a change in the in-plane ligand from 4-Mebpb(2-) / bpb(2-) to bpc(2-) causes a blue shift of only ~ 5 nm (solid state data). A similar trend is also observed in solution (shift in the case of chloro complexes: ~ 30 nm; shift in the case of acetate complexes: ~ 25 nm) (Table 3.12). These results point toward an important generalization: the effect in the change in axial ligands is more than that in the in-plane ligands.

3.4.6 EPR Spectra

The monomeric low-spin iron(III) complexes display characteristic rhombic **g** tensors whose principal **g** values are extremely sensitive to the nature of the axial ligands.[170-174] Since the structural data for our low-spin iron(III) complexes are not presently available, we analyzed the **g** values obtained for $[Fe(bpb)(C_5H_5N)_2]ClO_4$ and $Na[Fe(bpb)(CN)_2]$ according to the well established theory for low-spin d^5 system. This analysis provides the axial (Δ/λ) and rhombic (V/λ) crystal field distortion parameters in units of the spin-orbit coupling constant.

The EPR spectrum of the complex $[Fe(bpb)(C_5H_5N)_2]ClO_4$ in the polycrystalline state at 77 K shows a typical rhombic low-spin iron(III) behavior with three principal **g** values (Table 3.13; Figure 3.10). On the other hand, the low-spin complex Na[Fe(bpb)-

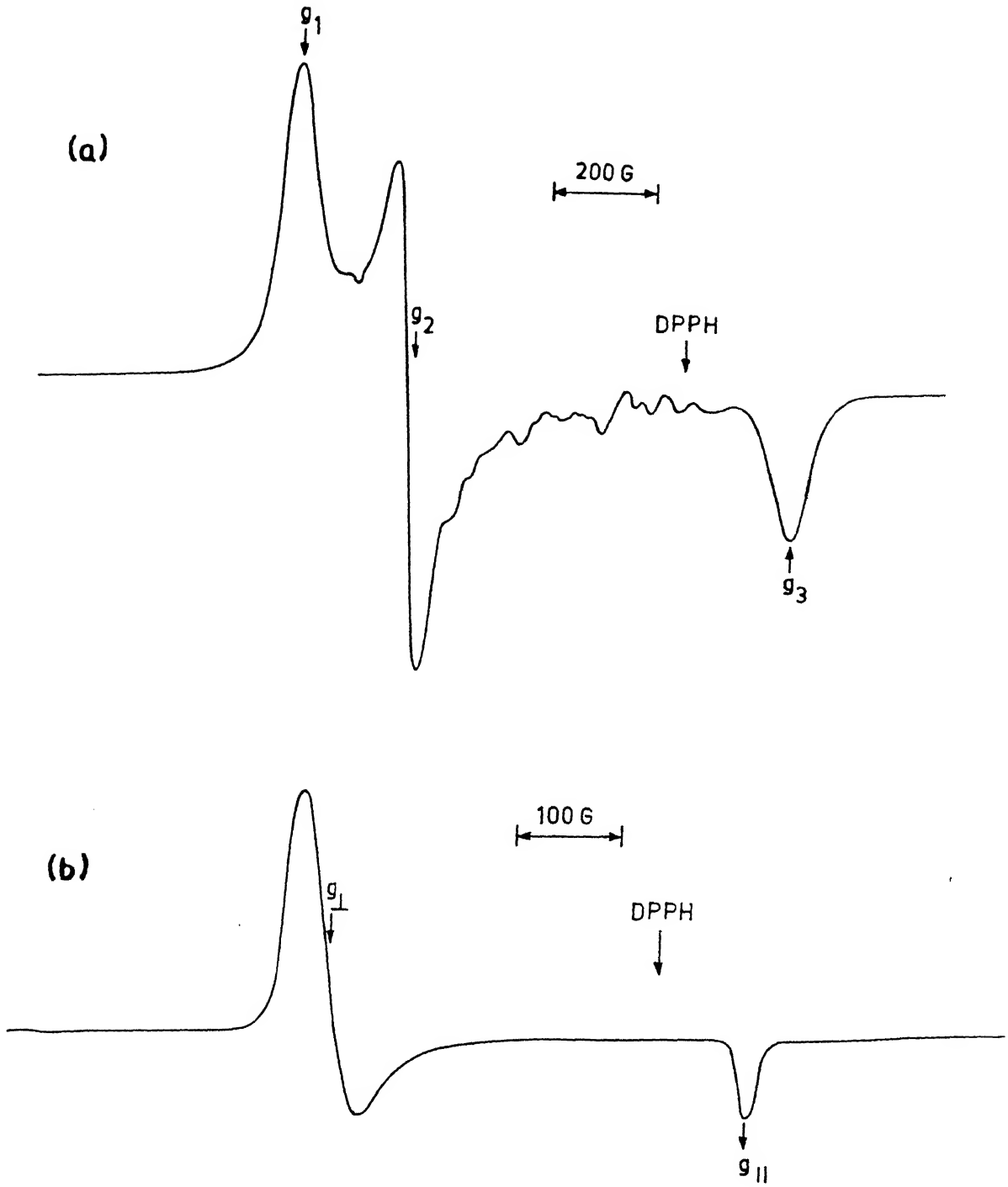

Figure 3.10 X-Band EPR spectra of **(a)** powder $[Fe(bpb)(C_5H_5N)_2]ClO_4$ at **77 K** and **(b)** $Na[Fe(bpb)(CN)_2]$ in DMF solution at **77 K**.

Table 3.13: X-Band EPR Spectral Data for the Iron(III) Complexes

Complex	Phase	T (K)	g
$[Fe(bpb)(C_5H_5N)_2]ClO_4$	powder	300	1.952, 2.197
	powder	77	1.943, 2.182,2.258
$Na[Fe(bpb)(CN)_2]$	powder	300	2.130
	powder	77	2.130
	solution[a]	77	1.955, 2.218
$(Et_4N)[Fe(bpc)(Cl)_2]$	powder	300	4.28[b]
	powder	77	4.28[b]
$(Et_3NH)[Fe(4\text{-}Mebpb)Cl_2]$	powder	300	2.020, 3.940[c]
	powder	77	2.026, 3.190
$(Et_4N)[Fe(bpc)(MeCO_2)_2].CHCl_3$	powder	300	2.020[d], 5.220
	powder	77	5.220
$(Et_4N)[Fe(bpb)(MeCO_2)_2].H_2O$	powder	300	2.850[c], 4.770[c], 7.900[c]
	powder	77	~ 5.00[c]

[a] In DMF solution ([Fe], 0.01M).

[b] Weak signal.

[c] Broad signal.

$(CN)_2$] in the polycrystalline state at 77K shows only a broad isotropic signal at g ~ 2.13. However, in DMF solution at 77 K it exhibits a typical low-spin d^5 axial spectra with two principal g values (Table 3.13; Figure 3.10). The relevant theory used in the interpretation of the EPR spectra of low-spin d^5 complexes is described elsewhere but a brief description of the parameters involved is appropriate here.[170-174]

In octahedral geometry, the $^2T_2$ ground term for low-spin d^5 species arises from the configuration $t^5{}_2$. A general distortion of the octahedron is expressed as the sum of axial and rhombic field perturbation. The axial distortion which can be tetragonal (or trigonal) splits the one-electron t_2 representation into b (or a) and e representations (small letters are used for one-electron representations and capital letters for state representations). The rhombic component splits e further into two nondegenerate orbitals.[170,171] This is shown in the followng Scheme IV.

Scheme IV

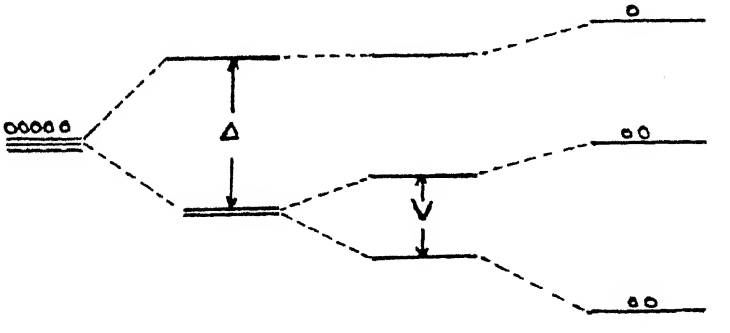

O_h axial rhombic spin-orbit

Splitting of t_2 level due to distortions and spin-orbit coupling

For visualization, the one-electron base functions can be combined to afford the d-orbitals in familiar real forms.[171] In a tetragonal system with z as the tetragonal axis, if d_{xy} lies

above d_{xz}, d_{yz}, the Δ (axial splitting parameter) is taken as positive, and when d_{yz} lies above d_{xz} in the case of added rhombic splitting V (rhombic splitting parameter) is taken to be positive. The parameter V/Δ is called rhombicity.[174]

Since the EPR experiment does not provide information about the labeling (x, y, z) and signs of the g values, we have examined all 48 possible combinations. From the few which satisfy the normalization criterion, we have selected a single solution which has a positive value of the rhombic distortion parameter and maximizes the absolute value of the axial distortion parameter.[173]

The single solution obtained thus gives the value of the axial distortion parameter (Δ/λ) and rhombic distortion parameter. The values a, b, c are the orbital coefficients in the ground Kramers doublet wave function.[171,172] In strict octahedral symmetry $a = \sqrt{2/3}$, $b = \sqrt{1/3}$, and $c = 0$. The solutions for our complexes as well as for selected reported systems are given in Table 3.14.

The a, b, and c values (Table 3.14) for the complex [Fe(bpb)-$(C_5H_5N)_2$]ClO_4 show that the geometry deviates from a perfect octahedron. The ground state of both the complexes are generally consistent with a $(d_{xz,yz})^4(d_{xy})^1$. Heme systems, however, typically have the hole in d_{yz}. Table 3.14 shows that the Δ values for both the complexes are comparable to that of $[Fe(\mathbf{34})(MeCN)_2]^+$.[173] Although the present pyridine and cyanide complexes have identical in-plane ligands, the different coordinating ability of the axial ligands fine tune the geometry in such a way that the rhombicity for cyanide complex becomes

Table 3.14: EPR Data, MO Coefficient, and Distortion Parameters for Iron(III) Complexes.

Complex	g_x	g_y	g_z	A	B	C	Δ/λ	V/λ	V/Δ
[Fe(bpb)-$(C_5H_5N)_2$]	2.182	2.258	1.943	0.099	0.995	-0.013	7.65	2.25	0.29
Na[Fe(bpb)-$(CN)_2$]	2.218	2.218	1.955	0.087	0.996	0.000	8.50	0.00	-
[Fe(**34**)-$(MeCN)_2]^{+a}$	2.219	2.329	1.959	0.078	0.996	-0.014	9.72	3.62	0.37
$[Fe(N_6)]^{3+b}$	2.463	2.841	1.631	0.240	0.969	-0.045	3.323	1.50	0.45
[Fe(PPIXDME)-$(MeIm)_2]^{+c}$	1.570	2.290	2.900	0.850	0.130	-0.510	-3.40	2.07	0.61

[a] (**34**) is a N_4 tetradentate dianionic ligand; Structure is given on p 67(Ref. 173).

[b] N_6 is a N_6 hexadentate neutral macrocyclic ligand (Ref. 173).

[c] PPDIXDME = protoporphyrin IX dimethyl ester ; MeIn = 1-Methyl imidazole (Ref. 167, 173).

zero. However, the rhombicity for the pyridine complex is 0.29. It is to be noted that the rhombicity of the pyridine complex is significantly smaller than that of porphyrin complexes or $[Fe(\mathbf{34})(MeCN)_2]^+$.[173]

The powder spectra of the axially ligated chloride and acetate complexes show the high-spin iron(III) nature of these complexes (Table 3.13). The crystal structures of $(Et_3NH)[Fe(bpb)Cl_2].CH_3CN$[161] and $(Et_4N)[Fe(bpc)(MeCO_2)_2].CHCl_3$ reveal a wide variation of the axial bond lengths (Tables 3.10 - 3.11). The finer details of the EPR spectra of the complexes depend on the nature of both axial as well as in-plane ligands. Thus the former complex shows a typical high-spin rhombic spectrum ($g \sim 4.28$) and the latter complex shows high-spin axial feature (Table 3.13). Nevertheless, the axially ligated acetate and chloride complexes show EPR spectra of essentially high-spin nature.

3.4.7 Electrochemistry

Electrochemical experiments were carried out to investigate the thermodynamic stability of the iron(III) state towards reduction. All the potentials reported here are with respect to saturated calomel electrode (SCE).

(a) Low-spin Complexes.—— The cyclic voltammogram of the complex $[Fe(bpb)(C_5H_5N)_2]ClO_4$ in pyridine shows a quasireversible (Section 2.1.2) reduction (E_f -0.06 V vs. SCE, ΔE_p 150 mV) due to a Fe^{III}-Fe^{II} couple (Table 3.15). No other well defined redox waves were seen within the potential scan range +0.7 V to -1.0 V. On the other hand, the complex $Na[Fe(bpb)(CN)_2]$ in DMF solution shows a $1e^-$ reduction (as judged by the current heights of

Table 3.15: Electrochemical[a] Data for the Iron(III) Complexes

Complex	Solvent	Cyclic voltammetry				
		bpb/bpc oxidation		Fe^{III}–Fe^{II} couple		
		E_f/V	ΔE_p/mV	E_{pc}/V	E_{pa}/V	ΔE_p/mV
$[Fe(bpb)(C_5H_5N)_2]ClO_4$[b]	pyridine	-	-	-0.13	0.02	150
$Na[Fe(bpb)(CN)_2]$[c]	DMF	0.66	80	-0.88	-0.78	100
$(Et_4N)[Fe(bpc)Cl_2]$	MeCN	1.04[d]	80	-0.40[e]	-0.04	360
$(Et_3NH)[Fe(4\text{-}Mebpb)Cl_2]$	MeCN	0.81[d]	100	-0.52[e]	-0.12	400
$(Et_4N)[Fe(bpc)(MeCO_2)_2].CHCl_3$	MeCN	0.93[f]	-	-0.72	-0.16	560
$(Et_4N)[Fe(bpb)(MeCO_2)_2].H_2O$	MeCN	0.80[f]	-	-0.83	-0.23	600

[a] Supporting electrolyte $[NBu_4^n]ClO_4$ (0.15 M; all potentials are referenced to SCE $E_f = 0.5\ (E_{pc} + E_{pa})$; E_{pc} and E_{pa} are the cathodic and anodic peak potentials respectively; scan rate is 50 mVs^{-1} at a glassycarbon electrode.

[b] No well defined oxidative response was observed within solvent cut off region (+0.6 V).

[c] Coulometric data are averages of at least three independent measurements; applied potential +0.9V;n=1.05 where n= coloumb count at the end of electrolysis/ calculated coloumb count for $1e^-$ transfer.

[d] A second irreversible oxidation was observed at +1.4 V (E_{pa}) for $(Et_4N)[Fe(bpc)Cl_2]$ and +1.27 V (E_{pa}) for $(Et_3NH)[Fe(4\text{-}Mebpb)Cl_2]$.

[e] The reduction preceded by a hump at -0.14 V for $(Et_4N)[Fe(bpc)Cl_2]$ and -0.25 V for $(Et_3NH)[Fe(4\text{-}Mebpb)Cl_2]$.

[f] E_{pa} as oxidation followed by adsorption at electrode surface occurs.

authenticated one-electron redox response; Section 2.1.2) corresponding to a Fe^{III}-Fe^{II} couple at -0.88 V vs. SCE (ΔE_p = 100 mV) which is substantially cathodically shifted. This data shows that the CN^- ion stabilizes iron(III) state significantly, implying that it behaves as a strong σ-donating ligand.[175] In fact, among all the axial ligands chosen in this work its stabilizing power towards iron(III) state is maximum (Table 3.15). Additionally, the cyanide complex shows an oxidative response (see below) at +0.66 V (Table 3.15, Figure 3.11). The $1e^-$ nature of this oxidation was confirmed by constant potential electrolysis in DMF (Table 3.15).

(b) High-spin Complexes.—— The electrochemical data for all the high-spin complexes in MeCN solution are given in Table 3.15. Two representative cyclic voltammograms are displayed in Figure 3.12. All the complexes show an irreversible Fe^{III}-Fe^{II} reduction (Table 3.15). The irreversibility of the Fe^{III}-Fe^{II} redox couple is possibly due to structural changes occurring after the addition of an electron to the iron(III) center. We have not yet explored the nature of such species. This could be due to a change in the spin-state of the iron center, given the behavior of the low-spin complexes.

These complexes show an additional quasireversible oxidative response (Figure 3.12, Table 3.15). The wave is reversible to quasireversible in the case of chloride as axial ligands. However, this wave is not very well defined in the case of acetate complexes due to interference of adsorption of the electroactive species on the electrode surface. To identify the

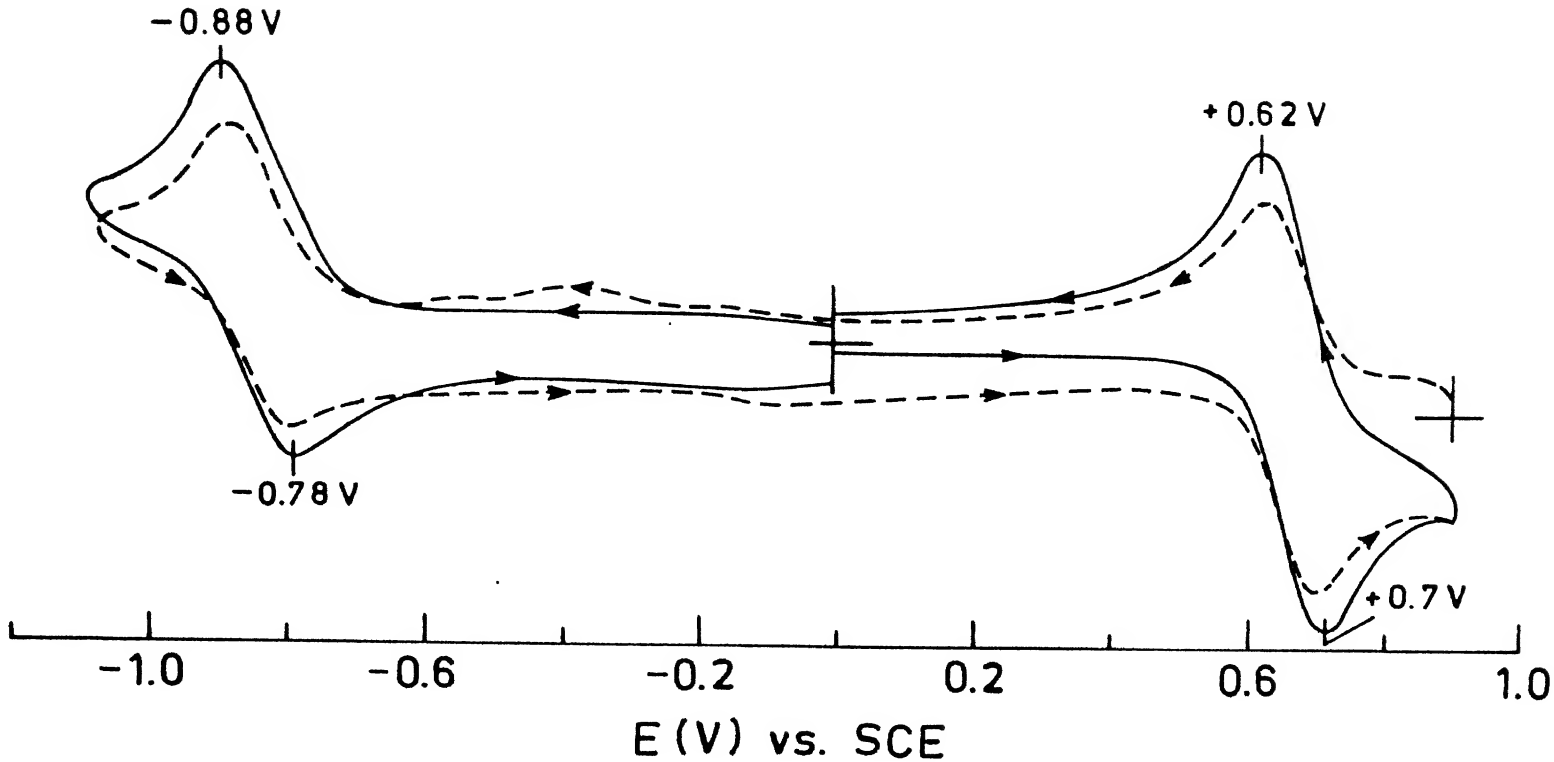

Figure 3.11 Cyclic voltammograms of $Na[Fe(bpb)(CN)_2]$ in DMF before (——) and after (- - -) coulometric oxidation.

Condition: scan rate 50 mV s-1; glassy carbon working electrode; supporting electrolyte TBAP.

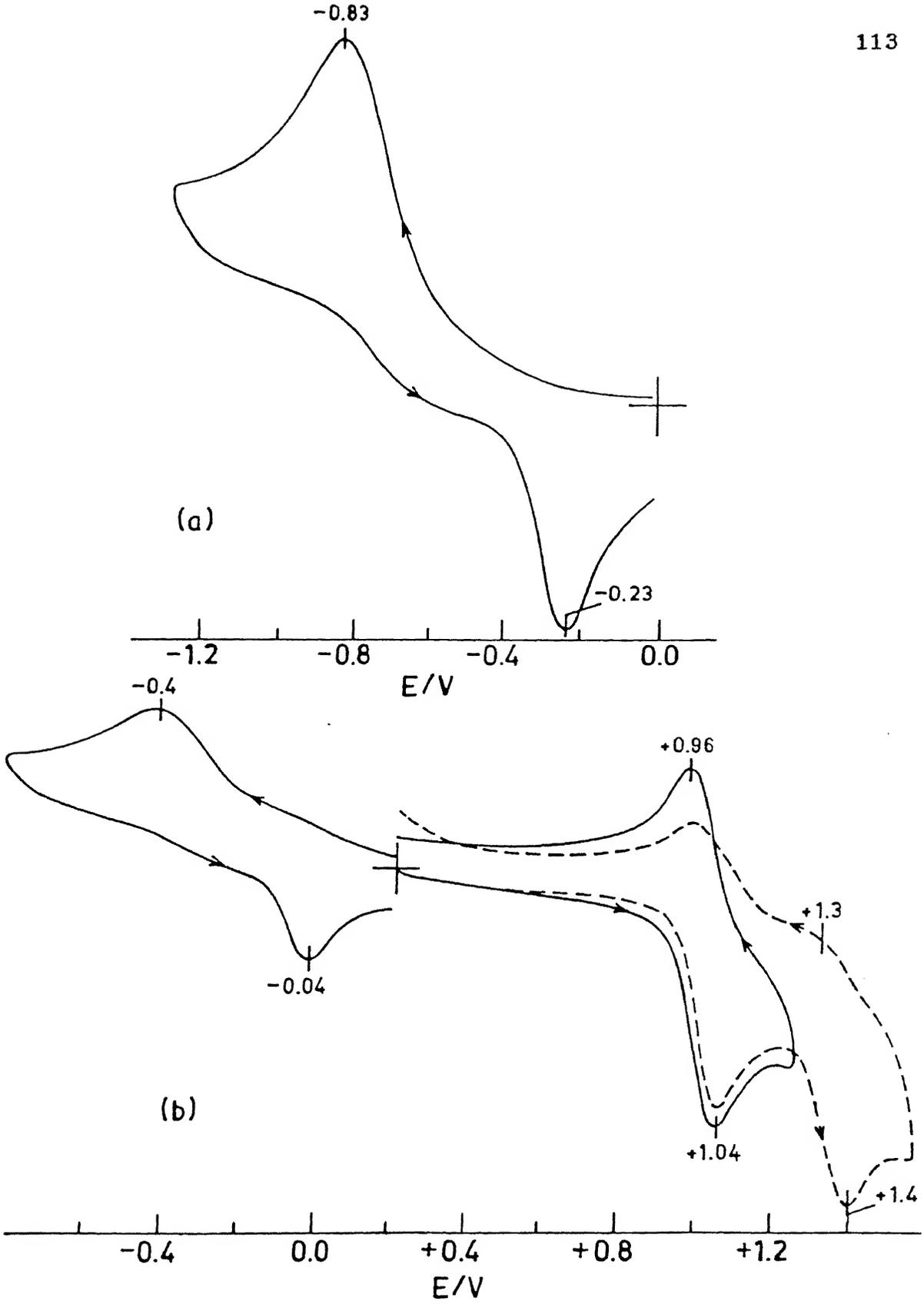

Figure 3.12 Cyclic voltammograms of $(Et_4N)[Fe(bpb)(MeCO_2)_2].H_2O$ (a) and $(Et_4N)[Fe(bpc)Cl_2]$ (b) in MeCN.
Condition: scan rate 50 mV s^{-1}; glassy carbon working electrode; supporting electrolyte TBAP.

nature of the site of this oxidation we have tried to oxidize three representative complexes (chloro complex of the 4-Mebpb(2-) ligand and the acetate complexes) chemically using cerric ammonium nitrate in MeCN. The oxidized solutions do not exhibit any well defined redox response in the potential range of interest, suggesting oxidative decomposition of the complexes (Chapter 4, Section 4.4.3).

3.4.8 Chemical/Electrochemical Oxidation of Na[Fe(bpb)(CN)$_2$]

Constant potential electrolysis of Na[Fe(bpb)(CN)$_2$] at +0.9V in DMF gives rise to a 1e$^-$ oxidation (Table 3.15). The purple colored solution thus generated shows well defined redox response as shown in Figure 3.11. This indicates that the 1e$^-$ oxidized species is sufficiently stable in solution and the possibility of isolating the species in the solid state can not be ruled out.

The complex Na[Fe(bpb)(CN)$_2$] is oxidized in water by cerric ammonium nitrate quantitatively. The purple colored oxidized product was immediately precipitated out from the aqueous solution, which was dried in vacuo. The solid state EPR spectrum (Figure 3.13) of this solid at 77 K shows g values centered around ~ 2, typical of low-spin axial iron(III) system. This confirms that the oxidation is ligand-centered.

The IR spectrum of the product shows the presence of coordinated cyanide at 2100 cm^{-1} and also $\nu_{\text{amide I}}$ occurs at 1670 cm^{-1}. The shift of $\nu_{C=O}$ from that of its congener (the $\nu_{\text{amide I}}$ stretching for Na[Fe(bpb)(CN)$_2$] occurs at 1620 cm^{-1}: Table 3.3) point towards the possibility of the oxidation

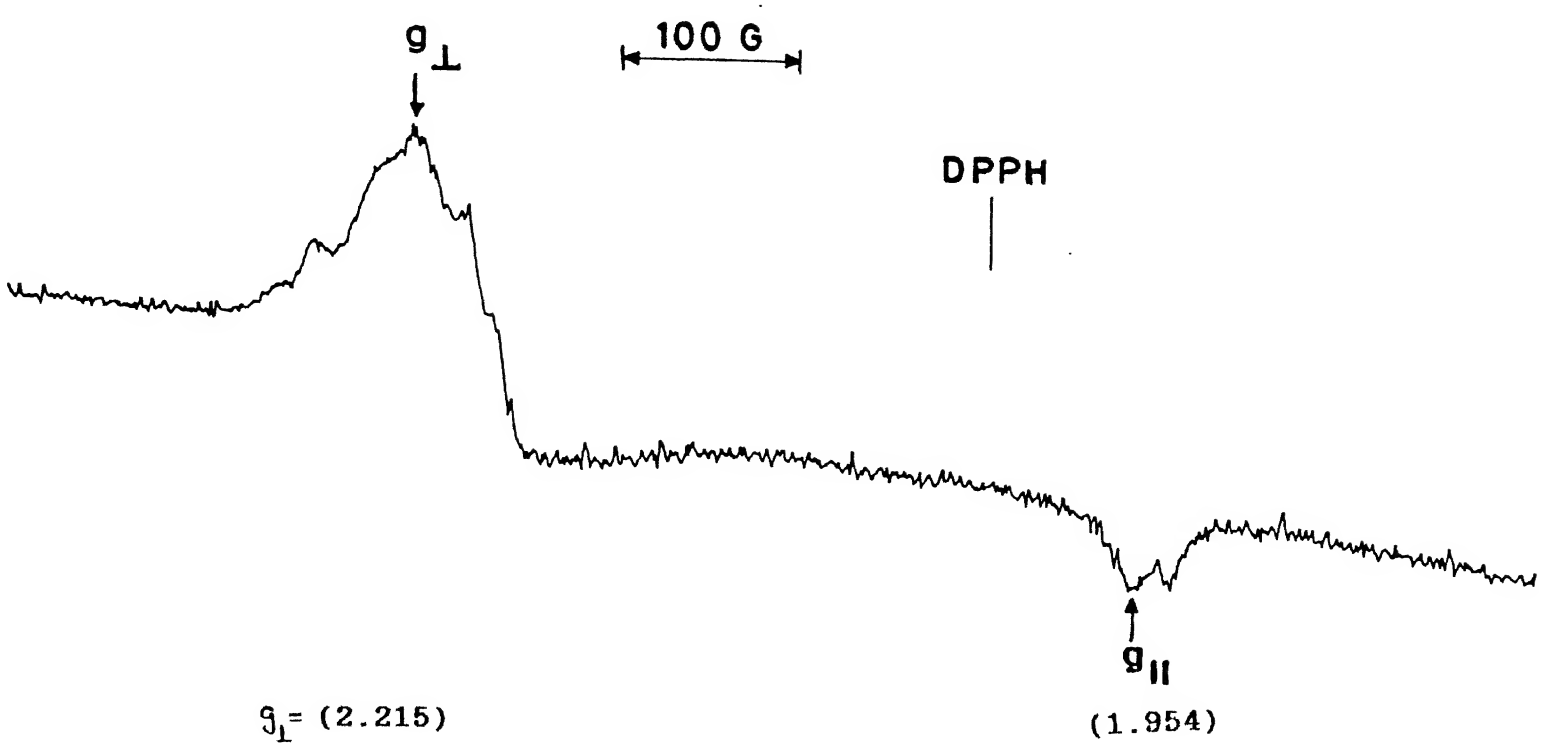

Figure 3.13 X-band EPR spectrum of chemically generated powdered $[Fe(bpb)(CN)_2]$ at 77 K.

occuring at the amide group.

In the case of ligand oxidation it is expected that the LMCT energy should shift towards higher energy due to poorer electron density of the ligand. The poor solubility of the complex in almost all common organic solvents prevented us from doing solution studies. However, the electronic spectrum of the oxidized species was recorded qualitatively for a dilute solution in $CHCl_3$ (Figure 3.14). The spectrum shows an intense absorption at 547 nm and two transitions of medium intensity one as a shoulder at ~770 nm and the other one as a peak at 698 nm. The intense absorption at 547 nm is possibly due to the MLCT transitions which is substantially blue shifted from that of its congener (the LMCT band for $Na[Fe(bpb)(CN)_2]$ in the solid state 800nm; in DMF solution 702 nm). This is as expected. The other two medium intense peaks are possibly of ligand field origin.

These results show that the oxidation observed in the electrochemical experiments of $Na[Fe(bpb)(CN)_2]$ is ligand-centered.

3.5 Conclusions

In this chapter we have explored a rare system comprising of iron-N(amide) bonding where spin state is regulated by the manipulation of axial ligands. The major achievements in this chapter are the following:

(i) We have synthesized a series of iron(III) complexes with deprotonated amide ligand which are indeed rare (Chapter 1).

(ii) A versatile synthetic strategy has been developed which utilizes the lability of the axial ligands to afford a wide variety of axially substituted complexes bypassing the inherent

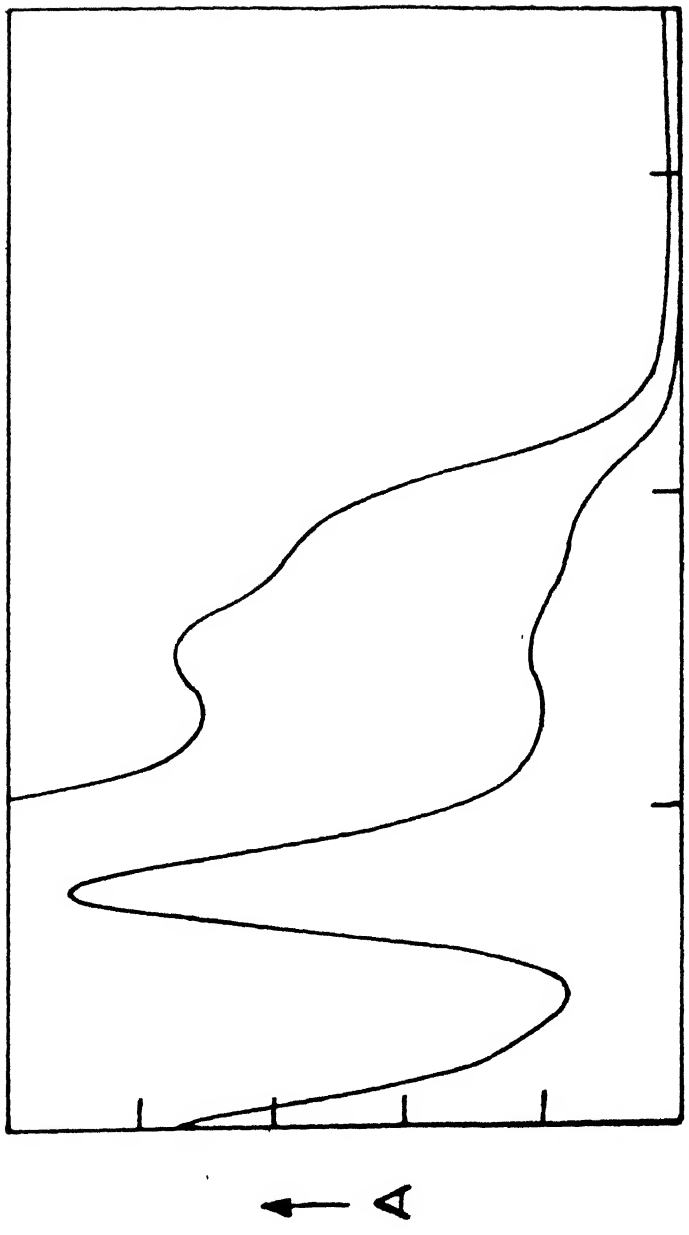

Figure 3.14 Electronic spectra of chemically generated [Fe(bpb)(CN)$_2$] in $CHCl_3$.

problem of using a base (Chapter 1).

(iii) We have shown that it is possible to manipulate the spin state of the iron(III) metal complexes by simply changing the axial ligands keeping the in-plane ligation fixed. This is really a very rare situation (Table 3.1) with non porphyrin N_4 ligand system and for the first time with a open-chain ligand system.

(iv) The oxidative responses observed in these class of complexes have been confirmed to be ligand-centered.

CHAPTER 4

In Chapters 2 and 3 we described the syntheses, spectral properties, and redox activity of a group of manganese(III) and iron(III) complexes using planar four-coordinate deprotonated N_4 bisamide ligands and additional axial ligand(s). In Chapter 2, the effect of the axial ligands on ligand field transitions as well as on the redox properties of high-spin manganese(III) complexes has been considered. In Chapter 3, the effect of the axial ligand fields was more pronounced in dictating the spin state of iron(III).

In order to investigate this ligand field effects in a more involved manner, in this chapter we have undertaken a program which is of twofold origin. First, to prepare a group of cobalt(III) complexes of general structural type trans-$[Co(L)X_2]^{1-}$ (L(2-) = bisamide ligands, X= monodentate anionic ligands) to reveal the effect of axial ligand donor atom types on the spectral and redox potential data. Secondly and more importantly, to provide a meaningful correlation between the field strength of these axial ligands and the Co^{III}-Co^{II} redox potentials of these cobalt(III) complexes having grossly similar stereochemistry and spin state of the metal center.

4.1 Experimental Section

4.1.1 Solvents and Reagents

Details of solvent purification and starting materials are already discussed in Chapter 2 (Section 2.1.1).

4.1.2 Measurements

The ^1H NMR spectra of cobalt(III) complexes were recorded on a Brüker WP-80 (80 MHz) NMR spectrometer with TMS as a standard.

The details for other measurements are already stated in Chapter 2 (Section 2.1.2).

4.2 Syntheses of Ligands

The details of ligand syntheses are already stated in Chapter 2 (Section 2.2).

4.3 Syntheses of Complexes

When our work was in progress the syntheses of four complexes, namely, $Na[Co(bpb)X_2]$ and $Na[Co(bpc)X_2]$ (where X = CN^- and N_3^-) were independently reported by Che and coworkers.[62] The synthetic procedure developed in this investigation is of general applicability.

4.3.1 $(Et_4N)[Co(bpb)Cl_2]$

The ligand $H_2(bpb)$ (0.318 g, 1 mmol) was added slowly to a stirred solution of $CoCl_2.6H_2O$ (0.238 g, 1 mmol) in DMF (15 mL). The blue solution which immediately turned green was stirred for 10 min. To this solution 2.78 mL of triethylamine (1:10 dilution in DMF, 2 mmol) and subsequently $(Et_4N)Cl.H_2O$ (0.367 g, 2.21 mmol) were added. The dark orange brown solution thus obtained was stirred for 6 h. The solvent was then evaporated under vacuum at ~310 K and acetonitrile (20 mL) was added to dissolve the residue. The solution was then filtered and reduced the volume of the filtrate down to 5 mL. On cooling the solution affords dark orange crystals (yield, ~ 80%). The complex was recrystallized from acetonitrile-diethyl ether (1:1 v/v) and dried over silica gel (yield, ~ 66%).

4.3.2 $(Et_4N)[Co(bpc)Cl_2]$

This complex was prepared in a similar manner as in the case of H_2(bpb) ligand (Section 4.3.1) and orange crystals thus obtained were finally dried over silica gel (yield ~ 57%).

4.3.3 $Na[Co(bpb)(N_3)_2]$

The ligand H_2(bpb) (0.318 g, 1 mmol) was added portionwise to a stirred solution of $Co(O_2CMe)_2.4H_2O$ (0.249 g, 1 mmol) in methanol (15 mL). The initial pink colored solution changed to greenish brown. The solution was stirred for 15 min and NaN_3 (0.26 g, 4 mmol) was added. The resulting mixture was stirred for 12 h and in the meantime a brown solution was obtained. This was filtered and volume reduced to ~ 10 mL. After addition of diethyl ether (5 mL) the solution was kept in the refrigerator. Dark brown crystals were isolated and dried in a desiccator containing silica gel (yield, ~ 70%).

4.3.4 $(Et_4N)[Co(bpc)(N_3)_2]$

The complex $(Et_4N)[Co(bpc)Cl_2]$ (0.1 g, 0.15 mmol) was dissolved in acetonitrile (5 mL) and to it was added NaN_3 (0.024 g, 0.37 mmol) and allowed to stir for 12 h. The precipitated NaCl and excess NaN_3 were filtered and to the filtrate diethyl ether (5 mL) was added. The compound crystallized out as yellowish brown flakes (yield, ~ 60%).

4.3.5 $(Et_4N)[Co(bpb)(NCS)_2]$

The complex $(Et_4N)[Co(bpb)(Cl)_2]$ (0.163 g, 0.28 mmol) with excess KSCN (0.07 g, 0.72 mmol) were taken in MeCN (10 mL) and stirred for 10 h. The resulting solution was concentrated and

filtered to remove excess KSCN and KCl formed in the reaction. Diethyl ether (1 mL) was added and then cooled in the refrigerator. The compound was isolated as deep brown crystalline powder after two days (yield, ~ 60 %).

4.3.6 $Na[Co(bpb)(NO_2)_2].H_2O$

To a stirred solution of $Co(ClO_4)_2.6H_2O$ (0.366 g, 1 mmol) in DMF (10 mL), $H_2(bpb)$(0.318 g, 1 mmol) and $NaNO_2$ (0.340 g, 4 mmol) were added subsequently. The resulting brown solution was stirred for 5 min and 2.78 mL of triethylamine (1:10 dilution in DMF, 2 mmol) was added. The resulting deep brown solution was stirred for 6h and solvent removed under vaccum. To the residue MeCN (5 mL) was added and filtered to remove excess KNO_2 and finally diethyl ether (10 mL) was added affording deep brown crystals of $Na[Co(bpb)(NO_2)]$ (yield, ~ 65 %).

4.3.7 $(Et_4N)[Co(bpb)(O_2CMe)_2]$

The ligand $H_2(bpb)$ (0.159 g, 0.5 mmol) and $Co(O_2CMe)_2.4H_2O$ (0.088 g, 0.5 mmol) were taken in DMF (5 mL) and stirred for 5 min. To the green solution thus obtained was added (Et_4N)-$(O_2CMe).4H_2O$ (0.19 g, 0.72 mmol) and stirring continued for 6 h. After this period the solvent was removed under vacuum and dissolved the residue in acetonitrile (5 mL). The resulting solution was filtered and to it diethyl ether (5 mL) was added and kept in the refrigerator. The desired product separated out as green shining needles (yield, ~ 57%).

The analytical and selected characterization data for all the complexes are given in Tables 4.1 and 4.2 respectively.

4.4 Results and Discussion

4.4.1 Syntheses and Characterization

The synthetic strategies employed in this work are more versatile than that reported for $[Co(bpb)(X)_2]^{1-}$ and $[Co(bpc)(X)_2]^{1-}$ (X = N_3^- or CN^-).[62] We have adopted basically three procedures to synthesize the complexes reported here. They include: (i) a one-pot synthetic strategy, (ii) exploration of axial ligand substitution reaction, and (iii) use of cobalt(II) perchlorate to enable one to synthesize the present kind of complexes with a desired axial ligand.

When $Co(O_2CMe)_2.4H_2O$ or $CoCl_2.6H_2O$ or $Co(ClO_4)_2.6H_2O$ in DMF, MeCN or methanol was stirred with H_2(bpb) or H_2(bpc) in air, an immediate color change was observed demonstrating a facile complex formation reaction. When cobalt(II) chloride or cobalt(II) perchlorate was used two equivalents of NEt_3 was needed for the deprotonation of the ligand N-H protons. However, when using $Co(O_2CMe)_2.4H_2O$ the acetate anions itself behave as the base. The desired bis axially ligated cobalt(III) complexes were prepared using Na^+, K^+ or Et_4N^+ salts of the appropriate anions. The azido complex of bpc(2-) and thiocyanato complex of bpb(2-) were prepared from the correspoding axially chloro ligated complexes by substituting the axial chloride. The most probable oxidizing agent in these syntheses is dioxygen. No attempt was made to monitor the metallation reactions under strictly anaerobic conditions.

The identity of these complexes $[Co(bpb)X_2]^{1-}$ (X = Cl^-, N_3^-, SCN^-, NO_2^-, and $MeCO_2^-$) and $[Co(bpc)X_2]^{1-}$ (X = Cl^- and N_3^-)

was confirmed by elemental analyses (Table 4.1), IR spectroscopy, solution electrical conductivity, and magnetic susceptibility measurements (Table 4.2). These cobalt(III) complexes were isolated as brown or green crystalline solids and they are highly soluble in polar organic solvents. The evidence for the isothiocyanato structure[176] of $[Co(bpb)(NCS)_2]^{1-}$ is obtained from the IR data as in the case of corresponding manganese(III) complex in Chapter 2 (Section 2.4.1). The more sensitive C-S frequency is not very useful in this case because ligand absorptions occur in the 700-900 cm^{-1} region. The N-bonded nature of the NO_2^- ligands[177] is confirmed by IR data. The characteristic IR band for $\nu(N_3^-)$ was observed for azido complexes.[62] For $[Co(bpb)(O_2CMe)_2]^{1-}$ the characteristic $\nu(C{=}O)$ band is also observed. Conductivity measurements in MeCN solution give values which are expected for 1:1 electrolytes.[123] The complexes are diamagnetic in MeCN solution. The deprotonated ligands bpb(2-) or bpc(2-) give only trans-complexes as is evident from three-dimensional X-ray structures of $[Os(bpb)(PPh_3)Cl]$,[57] $(Et_4NH)[Fe(bpb)Cl_2]$,[161] $[Rh(bpb)(C_5H_5N)_2]$,[60] $[Co(bpb)(C_2H_5)(H_2O)]$,[62] and $(Et_4N)[Fe(bpc)(MeCO_2)_2].CHCl_3$ (Chapter 3).

The ^1H NMR spectral measurements were performed in CD_3CN solution to elucidate the solution structure of these complexes. The results are given in Figure 4.1 and Table 4.3. The assignments are based on comparisons[60,62] with corresponding rhodium(III), iridium(III), and organocobalt(III) complexes and by integrated area ratios. The ^1H NMR spectral analysis reveals that the present complexes have trans-geometry.

Table 4.1 : Analytical Results[a] of Cobalt(III) Complexes

Complex	Empirical Formula	% C	% H	% N
$(Et_4N)[Co(bpb)Cl_2]$	$C_{26}H_{32}Cl_2CoN_5O_2$	54.30	5.80	12.30
		(54.17)	(5.59)	(12.15)
$Na[Co(bpb)(N_3)_2]$	$C_{18}H_{12}CoN_{10}O_2Na$	44.90	2.60	24.20
		(44.81)	(2.50)	(24.29)
$(Et_4N)[Co(bpb)(NCS)_2]$	$C_{28}H_{32}CoN_7O_2S_2$	54.20	5.40	15.60
		(54.05)	(5.15)	(15.76)
$Na[Co(bpb)(NO_2)_2].H_2O$	$C_{18}H_{14}CoN_6O_7Na$	42.50	2.90	16.60
		(42.50)	(2.75)	(16.53)
$(Et_4N)[Co(bpb)(O_2CMe)_2]$	$C_{30}H_{38}CoN_5O_6$	57.80	6.60	11.30
		(57.75)	(6.10)	(11.23)
$(Et_4N)[Co(bpc)Cl_2]$	$C_{26}H_{30}Cl_4CoN_5O_2$	48.50	4.80	10.70
		(48.36)	(4.68)	(10.85)
$(Et_4N)[Co(bpc)(N_3)_2]$	$C_{26}H_{30}Cl_2CoN_{11}O_2$	47.50	4.70	23.20
		(47.43)	(4.59)	(23.40)

[a] Values in parantheses are calculated ones

Table 4.2 : Molar conductance, Magnetic moment and Selected IR Data of Cobalt(III) Complexes in MeCN

Complex	Molar coductivity[a] Λ_M (Ω^{-1} cm^2 mol^{-1})	Magnetic moment[b] $\mu_{eff}(\mu_B)$	IR data[c] (cm^{-1})		
			ν_{amideI}	$\nu_{C\equiv N}$	ν_N
$(Et_4N)[Co(bpb)Cl_2]$	115	dia.			
$Na[Co(bpb)(N_3)_2]$	102	dia.	1615		2014
$(Et_4N)[Co(bpb)(NCS)_2]$	140	dia.	1610	2080	
$Na[Co(bpb)(NO_2)_2].H_2O$[d]	100	dia.	1610		
$(Et_4N)[Co(bpb)(O_2CMe)_2]$[e]	127	dia.	1620		
$(Et_4N)[Co(bpc)Cl_2]$	102	dia.			
$(Et_4N)[Co(bpc)(N_3)_2]$	104	dia.	1628		2005

[a] Expected 1:1 electrolyte range: 120-160 Ω^{-1} cm^2 mol^{-1}.[123]

[b] Measured in solution using Evans' method.[111]

[c] In KBr disk (4000-600 cm^{-1}).

[d] ν_s 1375 cm^{-1}; ν_{as} 1320 cm^{-1} ; δ_{ono} 810 cm^{-1}.

[e] $\nu_{C=O}$ for acetate occurs at 1638 cm^{-1}.

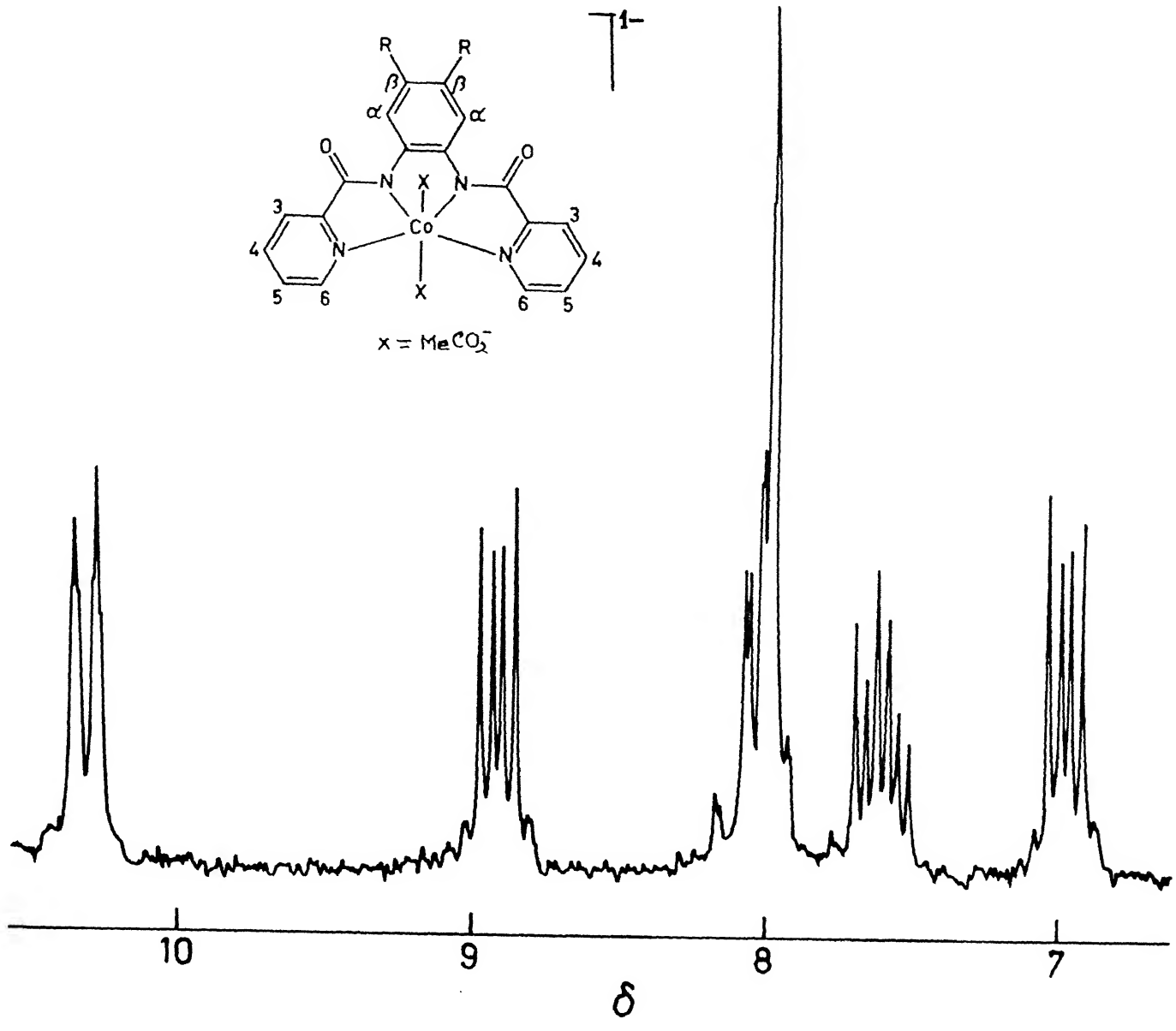

Figure 4.1 Partial ^1H NMR spectrum of $(Et_4N)[Co(bpb)(O_2CMe)_2$ in CD_3CN.

Table 4.3 : Proton NMR Spectral Data of Cobalt(III) Complexes

Complex	Aassignments[a]			
	H_β	H_α	H^6	$H^{3,4,5}$
$(Et_4N)[Co(bpb)Cl_2]$[b]	7.04 (dd, 2H) J_m = 3.50 J_o = 6.00	8.95 (dd, 2H) J_m = 3.50 J_o = 6.00	9.71 (d, 2H) $J(H^5H^6)$ = 5.50	7.72–8.28 (m, 6H)
$Na[Co(bpb)(N_3)_2]$	7.00 (dd, 2H) J_m = 3.50 J_o = 6.00	8.87 (dd, 2H) J_m = 3.50 J_o = 6.00	9.34 (d, 2H) $J(H^5H^6)$ = 5.50	7.65–8.28 (m, 6H)
$(Et_4N)[Co(bpb)(SCN)_2]$	7.10 (dd, 2H) J_m = 3.50 J_o = 6.00	8.89 (dd, 2H) J_m = 3.50 J_o = 6.00	9.56 (d, 2H) $J(H^5H^6)$ = 5.00	7.81-8.37 (m, 6H)
$Na[Co(bpb)(NO_2)_2].H_2O$	7.00 (dd, 2H) J_m = 3.75 J_o = 6.25	8.75 (dd, 2H) J_m = 3.75 J_o = 6.25	9.41 (d, 2H) $J(H^5H^6)$ = 6.25	7.66-8.28 (m, 6H)
$[NEt_4][Co(bpb)-(MeCO_2)_2]$[b,c]	6.97 (dd, 2H) J_m = 3.43 J_o = 5.93	8.93 (dd, 2H) J_m = 3.43 J_o = 5.93	10.32 (d, 2H) $J(H^5H^6)$ = 6.25	7.50–8.15 (m, 6H)
$(Et_4N)[Co(bpc)Cl_2]$[b]		9.03 (s, 2H)	9.65 (d, 2H) $J(H^5H^6)$ = 5.50	7.65–8.28 (m, 6H)
$(Et_4N)[Co(bpc)(N_3)_2]$[b]		8.97 (s, 2H)	9.31 (d, 2H) $J(H^5H^6)$ = 5.50	7.65–8.28 (m, 6H)

[a] Proton numbering scheme is shown in the ligand structure. Chemical shifts are(± 0.01 ppm) with reference to $SiMe_4$ in CD_3CN solution. Coupling constants, J, in Hz; J_o = ortho coupling, J_m = meta coupling. Integrated peak areas in all cases are consistent with the assignments given. Legend: m = multiplet, s = singlet, d =doublet, dd = doublet of doublets, q = quartet. [b] NEt_4^+ ion shows peaks at 3.15 (q, 8 H) for CH_2 and at 1.15 (t, 12 H) for CH_3 protons. [c] Methyl signal of $MeCO_2^-$ ion merged with methyl protons from NEt_4^+ ion at 1.18 (m, 18 H).

4.4.2 Absorption Spectra

The electronic absorption spectral results of these complexes are in Table 4.4 and representative spectra are displayed in Figure 4.2. All complexes show in the order of increasing energy three types of absorptions: ligand field bands of low intensity, transitions of medium intensity, which are due to the ligand-to-metal charge-transfer processes and very strong absorptions due to intraligand transitions. The low-energy absorption band positions shift in the order: $Cl^- < N_3^- < SCN^- < MeCO_2^- < NO_2^-$. This is consistent with similar trends observed for related systems.[176-178]

A simple crystal field model for analyzing the spectra of tetragonal splittings of the spectroscopically accessible $^1T_1$ state of cobalt(III) complexes was proposed by Wentworth and Piper (Scheme V).[179] Since the splittings may be expressed in terms of the ligand field strengths of the tetradentate ligands, $\underline{Dq}^{xy}$, and of the axial ligands, $\underline{Dq}^z$, the electronic spectra of these complexes have been subjected to extensive studies. The crystal field model for tetragonally distorted $\underline{d}^6$ metal complexes suggests that the splitting of the low-energy $\underline{d}$-$\underline{d}$ transition $^1A_{1g} \longrightarrow {}^1T_{1g}$ in an octahedral symmetry, into its two components E ($^1A_{1g} \longrightarrow {}^1E_g{}^a$) and A ($^1A_{1g} \longrightarrow {}^1A_{2g}$), upon lowering of the symmetry to D_{4h},

Table 4.4. Electronic Spectral[a] Data for the Cobalt(III) Complexes in MeCN

Complex	λ_{max}, nm, (ϵ, M^{-1} cm^{-1})
$(Et_4N)[Co(bpb)Cl_2]$	796(210), 411(6 900), 311(sh)(11 600)[b], 272(20 100)
$Na[Co(bpb)(N_3)_2]$	695(sh)(135), 595(sh) (180),475(sh)(3 400) 419(sh)(6 400) 345(19 000), 281(sh) (13 400), 255(16 200)
$(Et_4N)[Co(bpb)(NCS)_2]$	685(sh)(150), 406(7 850) 306(15 500),276(17 300), 222(43 200)
$Na[Co(bpb)(NO_2)].H_2O$	560(sh)(310), 405(sh) (5 500),372(sh)(6 500), 316(sh)(11 500),265(18 900)
$(Et_4N)[Co(bpb)(O_2CMe)_2]$	621(170), 410(7 400), 309(sh)(13 500), 250(sh)(26 000)
$(Et_4N)[Co(bpc)Cl_2]$	774(207), 408(8 400), 311(14 100), 274 (25 700)
$(Et_4N)[Co(bpc)(N_3)_2]$	687(sh)(156), 599(225), 484(sh)(3 400), 415(sh) (8 700), 345(20 900), 285(sh)(16 300), 259 (18 900)

[a] Spectral measurements in the range 500 -1100nm were made at ~ 10^{-3} M and for the range 200-500nm were made at ~ 10^{-4} M .

[b] sh = shoulder.

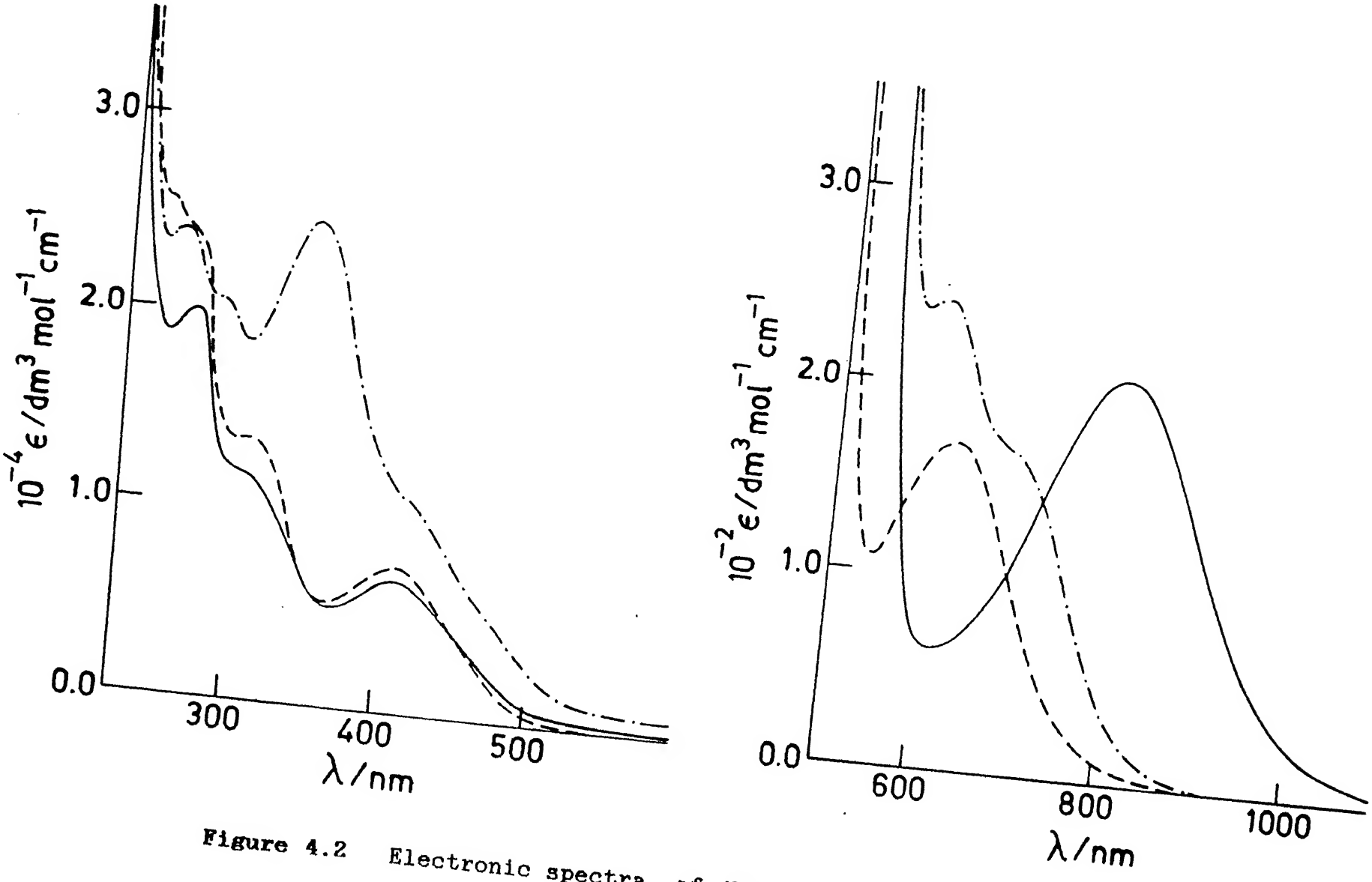

Figure 4.2 Electronic spectra of $(Et_4N)[Co(bpb)Cl_2]$ (——), $(Et_4N)[Co(bpb)(O_2CMe)_2]$ (- - -), and $(Et_4N)[Co(bpb)(N_3)_2]$ (-·-·-) in MeCN solution.

Scheme V

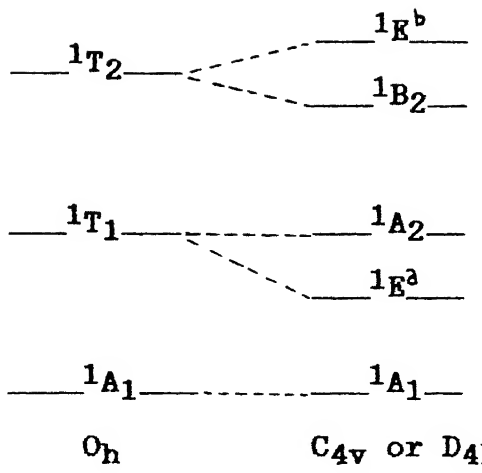

Tetragonal splitting of the exited states of cobalt(III).

will be observed if the in-plane and axial ligands have significantly different ligand field strengths. This splitting is associated with a single tetragonal splitting parameter Dt. The values of Dt are greatest for the strongest in-plane ligands. Application of this approach to the present complexes leads to the ligand field splitting parameters Dq^{xy} associated with bpb(2-) and bpc(2-) ligands and Dq^{z} relating to the axial groups. The equations which apply[179] are:

$$A = 10Dq^{xy} - C \qquad (4.1)$$

$$Dt = (4/35)(10Dq^{xy} - E - C) \qquad (4.2)$$

$$Dq^{z} = Dq^{xy} - (7/4)Dt \qquad (4.3)$$

The interelectronic repulsion parameter C is taken to be 3800 cm^{-1}, a value shown[179] to be roughly independent of the field strength. The low-energy band splits into two components only for bis azido complexes $[Co(bpb)(N_3)_2]^{1-}$ and $[Co(bpc)(N_3)_2]^{1-}$ while

only one d-d band is observed for rest of the complexes (Table 4.4). In most cases the expected $^1A_1$---> $^1T_2$ band is masked by the intense charge-transfer bands. Hence for the complexes having a common in-plane ligand, we have used a constant value of Dq^{xy} calculated from the spectrum of $[Co(bpb)(N_3)_2]^{1-}$ or $[Co(bpc)(N_3)_2]^{1-}$ [Equation (4.1)]. We have taken in the calculations recorded in Table 4.5, the energy of the $^1A_1$ ---> $^1E^a$ transition directly from the maximum of the unresolved band and ligand-field parameters were calculated in these complexes using Equations (4.2) and (4.3). The appropriateness of this approach is indicated in that the values of Dq^{xy} for the bis azido complexes containing similar in-plane ligands bpb(2-) and bpc(2-) are nearly the same (Table 4.5). Additionally, the values of Dq^z for Cl^- and N_3^- obtained from bpb(2-) and bpc(2-) in-plane ligands are also comparable. We observe like many others[180-182] that Dq^z is related in an inverse manner to Dq^{xy}.

For the purpose of comparison we list in Table 4.6 the D_q^{xy} values for selected ligands along with our ligands. It is worth noting that the present ligand system give rise to weakest in-plane ligand field strength.

We would like to emphasize here that to the best of our knowledge this is for the first time that for cobalt(III) complexes using deprotonated bis-amide in-plane ligands a thorough spectral analysis has been done.

4.4.3 Electrochemistry

The purpose of electrochemical studies on these cobalt(III) complexes was to investigate the sensitivity of the Co^{III}-Co^{II}

Table 4.5 : Ligand Field Parameters calculated for Cobalt(III) Complexe

Complex	$Dq^{xy}(cm^{-1})$	$Dt(cm^{-1})$	$Dq^{z}(cm^{-1})$
$(Et_4N)[Co(bpb)Cl_2]$	2060	485	1210
$Na[Co(bpb)(N_3)_2]$	2060	276	1580
$(Et_4N)[Co(bpb)(NCS)_2]$	2060	252	1620
$Na[Co(bpb)(NO_2)].H_2O$	2060	-120	2270
$(Et_4N)[Co(bpb)(O_2CMe)_2]$	2060	80	1920
$(Et_4N)[Co(bpc)Cl_2]$	2050	431	1295
$(Et_4N)[Co(bpc)(N_3)_2]$	2050	244	1620

redox potentials with change in the donor strength of the axial ligands. The redox behavior of these complexes was examined by cyclic voltammetry in MeCN at a glassy carbon working electrode. The electrochemical data are presented in Table 4.7 and the voltammetric behavior of a representative complex $(Et_4N)[Co(bpb)Cl_2]$ is shown in Figure 4.3.

4.4.3.1 The Cobalt(III)-Cobalt(II) Couple

In general, the Co(III) ---> Co(II) reductions for all of these complexes are irreversible (however, the rereduction waves are seen) when examined at a moderate potential scan rate (0.05 V/s). The reduction waves of the $[Co(bpb)X_2]^{1-}$ and $[Co(bpc)X_2]^{1-}$ (X = N_3^- and CN^-), assignable to the Co^{III}-Co^{II} couple, were reported[62] to be poorly resolved, as observed in this work. For $[Co(bpb)Cl_2]^{1-}$ variable scan rate experiments (0.05 - 1.0 V/s) were performed (Figure 4.4) to investigate whether or not the Co^{III} ---> Co^{II} electrode process becomes moderately well behaved. We observe that the general nature of the cyclic voltammograms does not change but the peak potentials become noticeably scan rate dependent as expected for irreversible electrode processes. We have recorded potentials in Table 4.7 at a scan rate of 0.05 V/s.

It is noteworthy that six-coordinate cobalt(III) complexes with uninegative monodentate ligands in the trans-positions generally exhibit totally irreversible[183-186] Co^{III} ---> Co^{II} reductions with no evidence for well-defined anodic peaks. This behavior has been explained due to either a poorer thermodynamic stability of the $[Co^{II}(L)X_2]^{2-}$ (L = a tetradentate dianionic

Table 4.7 : Electrochemical[a] Data for the Cobalt(III) Complexes

Complex	Cyclic voltammetry					
	bpb/bpc oxidation		Co^{III}–Co^{II} couple		Co^{II}–Co^{I} couple	
	E_f/V	ΔE_p/mV	E_{pc}/V	E_{pa}/V	E_f/V	ΔE_p/mV
$(Et_4N)[Co(bpb)Cl_2]$[b]	0.73	60	-0.56	0.00	-1.16	80
$Na[Co(bpb)(N_3)_2]$	0.74	80	-0.84	-0.22	-1.18	80
$Na[Co(bpb)(NO_2)_2].H_2O$	0.88[c]	–	-1.18	-0.16	-1.27	140
$(Et_4N)[Co(bpb)(NCS)_2]$	1.00[c]	–	-0.74	0.10	-1.40[d]	240
$(Et_4N)[Co(bpb)(O_2CMe)_2]$	0.69	70	-0.70	-0.02	-1.20	120
$(Et_4N)[Co(bpc)Cl_2]$	0.90	80	-0.42	-0.04	-1.12	90
$(Et_4N)[Co(bpc)(N_3)_2]$	0.92	70	-0.75	-0.24	-1.16	90

[a] Supporting electrolyte $[NBu_4^n]ClO_4$ (0.15 M; all potentials are referenced to SCE $E_f = 0.5\ (E_{pc} + E_{pa})$; E_{pc} and E_{pa} are the cathodic and anodic peak potentials respectively; scan rate is 50 mVs^{-1} at a glassy carbon electrode.

[b] Coulometric data are averages of at least three independent measurements; applied potential +0.9V; n=1.05 where n = coloumb count at the end of electrolysis/calculated coloumb count for $1e^-$ transfer. Applied potential -1.36V; n = 2.2.

[c] E_{pa} as irreversible oxidation occurs in this case.

[d] E_{pc} as irreversible reduction occurs.

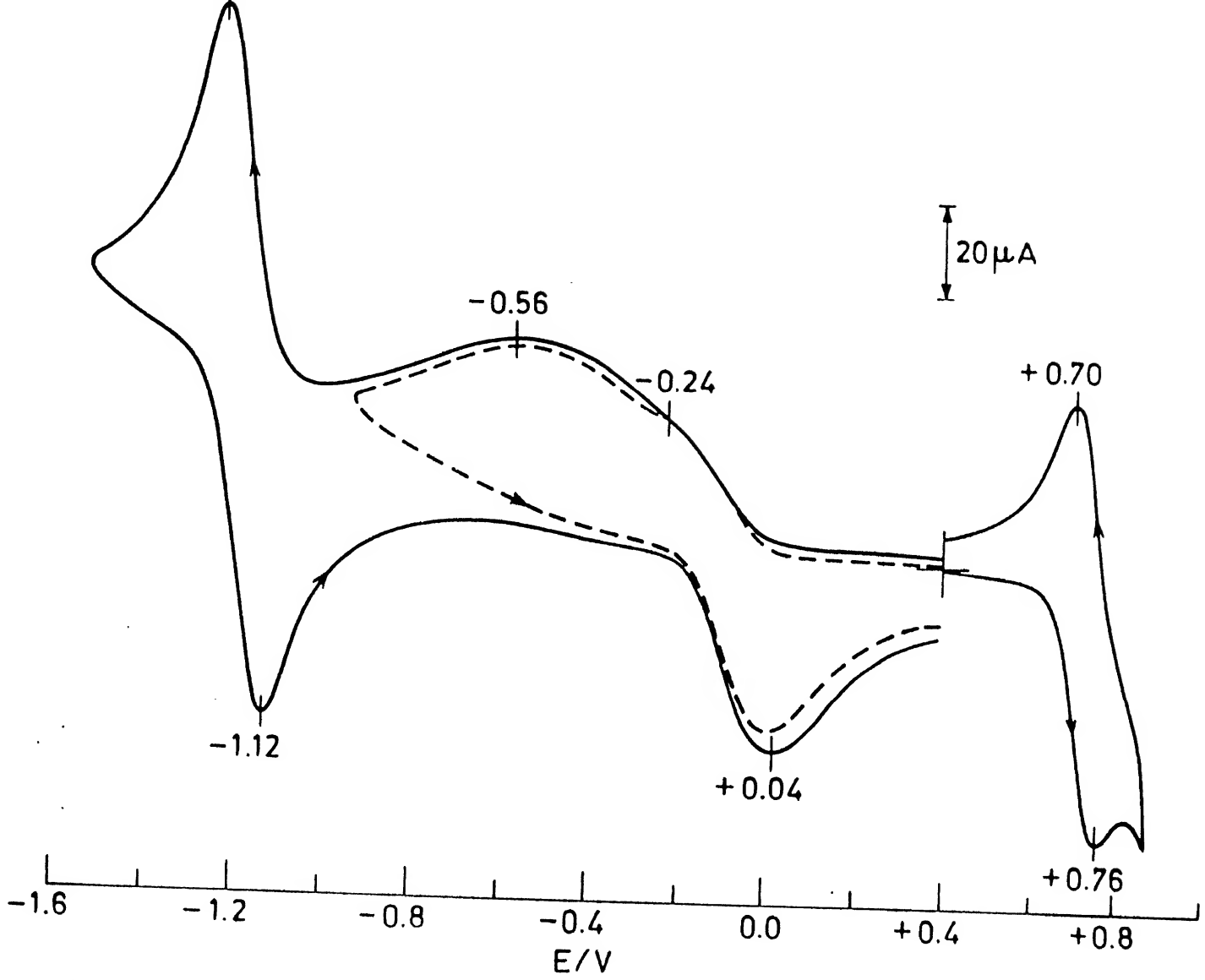

Figure 4.3 Cyclic voltammogram of $(Et_4N)[Co(bpb)(Cl)_2]$ in MeCN. Condition : scan rate 50 mV s^{-1}; glassy carbon working electrode; supporting electrolyte TBAP.

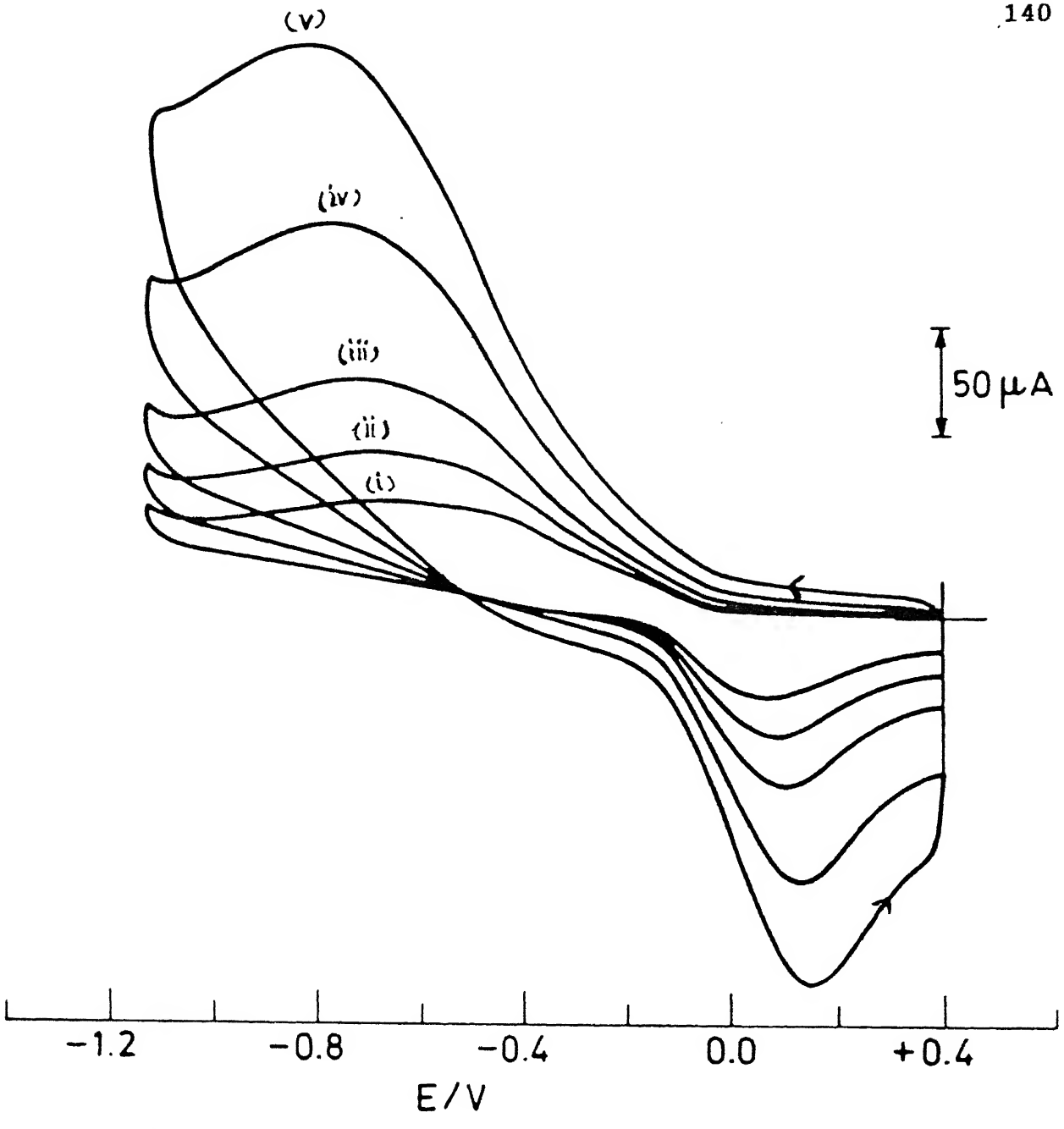

Figure 4.4 Cyclic voltammograms of $(Et_4N)[Co(bpb)(Cl)_2]$ in MeCN. Condition: scan rate (i) 50, (ii) 100, (iii) 200, (iv) 500, and (v) 1000 mV s^{-1}; glassy carbon working electrode; supporting electrolyte TBAP.

ligand) complexes or that the solvolysis reactions of the $[Co^{II}LX_2]^{2-}$ complexes are very fast. We are inclined to believe that the latter is really true in our case given the fact that the complex Co(bpb).H_2O (S = 1/2) has been isolated in the solid state.[53] In some cases during cyclic voltammetric reduction of cobalt(III) complexes the reoxidative anodic wave is observed but with large peak-to-peak separations (ΔE_p).[187-191] In the present case the ΔE_p values for this couple are also very large (Table 4.7).

4.4.3.2 The Cobalt(II)-Cobalt(I) Couple

For all the complexes Co^{III} ----> Co^{II} cathodic wave is followed by a quasi-reversible reduction wave (in the case of $[Co(bpb)(NCS)]^{1-}$ this wave is irreversible; however, the reoxidative wave was seen). We assign this due to a Co^{II}-Co^{I} couple. Constant potential electrolysis experiments on $[Co(bpb)Cl_2]^{1-}$ at -1.36 V confirm a total of two-electron transfer in the reduction processes (Table 4.7). The reduced sensitivity of the Co(II) ---> Co(I) formal potential (Table 4.7) with changes in the axial ligands for a given in-plane ligand suggests that the species being reduced is more or less the same in all cases and whose composition may be [Co(bpb)(MeCN)] or [Co(bpc)(MeCN)] (see above), formed by the solvolysis of the Co(III) ----> Co(II) reduction product. Similar well-defined cyclic voltammograms for the Co(II) ---> Co(I) reduction by unsaturated ligands have been documented in the literature.[182-192]

4.4.3.3 The Cobalt(IV)-Cobalt(III) Couple or Ligand Oxidation

An interesting observation in the cyclic voltammetric

measurements of most of these cobalt(III) complexes is the presence of a nearly reversible oxidative response in the range 0.69 to 0.92 V (Figure 4.3, Table 4.7). For X = SCN^- and NO_2^- this couple is irreversible (Table 4.7). Stabilization of the formally +4 oxidation state of cobalt has been reported using bis(salicylamide) ligands.[19,32,193] The oxidative response observed here could be due to the formation of cation radical of the benzamide bridge as has been observed[60] for the complex, $[Rh(bpb)(py)_2]^{1-}$. Constant potential coulometric experiments on $(Et_4N)[Co(bpb)Cl_2]$ reveal the transfer of one-electron in this oxidative process (Table 4.7). The color of the solution changes from orange to yellow during electrolysis. We could not observe any EPR response from these solutions even at 77 K. Additionally, it is to be noted that the coulometrically generated oxidized solutions do not exhibit any well-defined redox response in the potential range of interest, suggesting oxidative decomposition of the complex. The unstable nature of the oxidized species was also observed by Mak et al.[60]

Two main results emerge from a closer look into the E_{pc} / E_f values of these complexes (Table 4.7):

(i) For a given in-plane ligand (bpb) the E_{pc} values for the Co^{III}/Co^{II} couple decrease in the order: NO_2^- > N_3^- > SCN^- > $MeCO_2^-$ > Cl^-.

(ii) The formal potentials for the Co^{II}-Co^{I} couple and also the oxidative couple are relatively independent of the nature of the axial ligands. From the shift of the E_f values with change in X^- as well as comparing with zinc(II) complex as

already discussed in Chapter 2 (Section 2.4.4.2) it seems reasonable to believe that in the case of oxidation metal participation is also involved.

4.4.4 Spectroelectrochemical Correlations

Owing to the very facile substitution of the axial ligands in the reduced form of these cobalt(III) complexes (see above), electrochemical reversibility for the Co^{III}-Co^{II} couple is not obtained. Thus the Co^{III} ---> Co^{II} potential data are limited to measurement of the cathodic peak potential (E_{pc}),[194] which are the potentials measured where the cathodic peak current is at its maximum and this should not be confused with thermodynamic reduction potentials, which are obtained from reversible cyclic voltammograms. Nevertheless, these E_{pc} values are valuable quantities for discussing similarities and disparities within a class of compounds.[194]

From the E_{pc} values (Table 4.7) it is evident that the more stronger axial ligands (Table 4.5) shift the potential to more negative values, whilst the less stronger axial ligands have the opposite effect. The discrepancy of the acetato complex may be due to its not being predominantly σ donor (see below). We became interested in seeing if the E_{pc} values of a group of four complexes (X = Cl^-, SCN^-, N_3^-, and NO_2^-) for a given in-plane ligand bpb(2-) having the same charged type could be correlated with the ligand field strength of these axial ligands. It is to be noted that in all these measurements the solvent is invariant (MeCN). Interestingly, the spin state of the metal also does not change (see above) during electron transfer (both are low-spin).

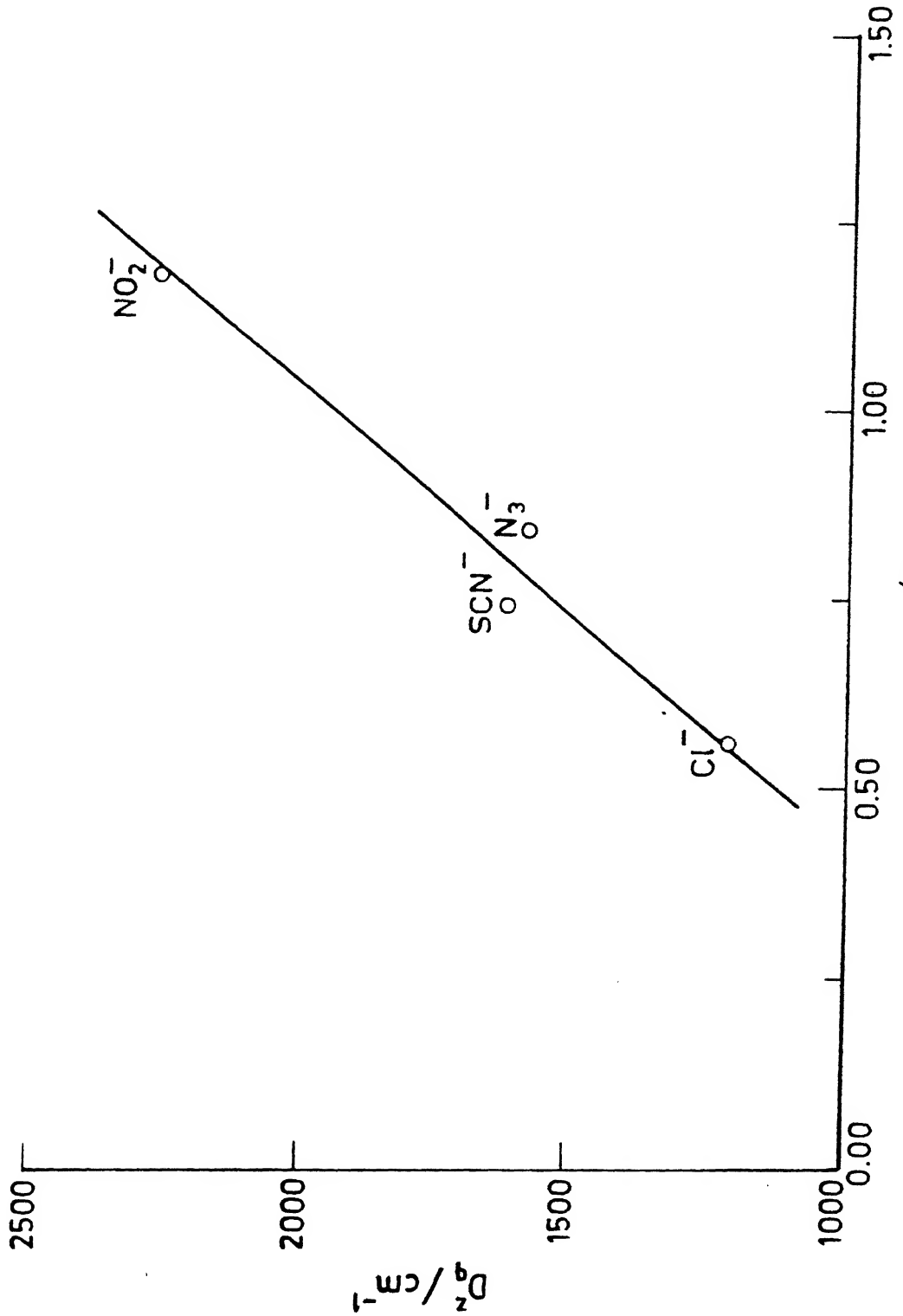

Figure 4.5 The least squeres plot of Dq^2 **vs.** $E_{p,c}$ for $[Co(bpb)X_2]^{1-}$ (X = Cl^-, N_3^-, SCN^-, NO_2^-) complexes.

In this situation a linear correlation is expected[195,196] between the E_{pc} values for the Co^{III}-Co^{II} couple and the $\underline{Dq}^z$ values for the axial ligands. This is exactly what has been achieved (Figure 4.5) and is consistent with the electron being added to the d_{z^2} antibonding metal orbital[181,185] which is being tuned by the field strength of the axial ligands, $\underline{Dq}^z$. As expected, the slope of the plot of $\underline{Dq}^z$ vs E_{pc} (Figure 4.5) is 1.6 cm^{-1} mV^{-1}.[197] A linear line is also obtained if one plots E_{pc} vs. energies of the lowest energy d-d band implying importance of the axial ligand in these four complexes for a given in plane ligand (Figure 4.6).

4.5 Conclusion

The major results which emerge from this Chapter are the following:

(i) The bis(picolinamide) ligands bpb(2-) and bpc(2-) have been used to synthesize a group of diamagnetic trans-$[CoLX_2]^{1-}$ complexes (L = bpb(2-) or bpc(2-); X = Cl^-, N_3^-, SCN^-, NO_2^- or $MeCO_2^-$].

(ii) The present complexes exhibit a facile electron-transfer series, $Co^{III} \longrightarrow Co^{II} \rightleftharpoons Co^{I}$.

(iii) A linear spectroelectrochemical correlation has been provided demonstrating the importance of the nature of the axial ligands in this group of complexes.

(iv) The weak field nature of the present tetradentate ligand system as revealed from the detailed spectroscopic analysis (Table 4.6) explains the strong influence of axial ligands on the spectral and redox properties and spin-state of the metal complexes, as seen in this Chapter as well as in

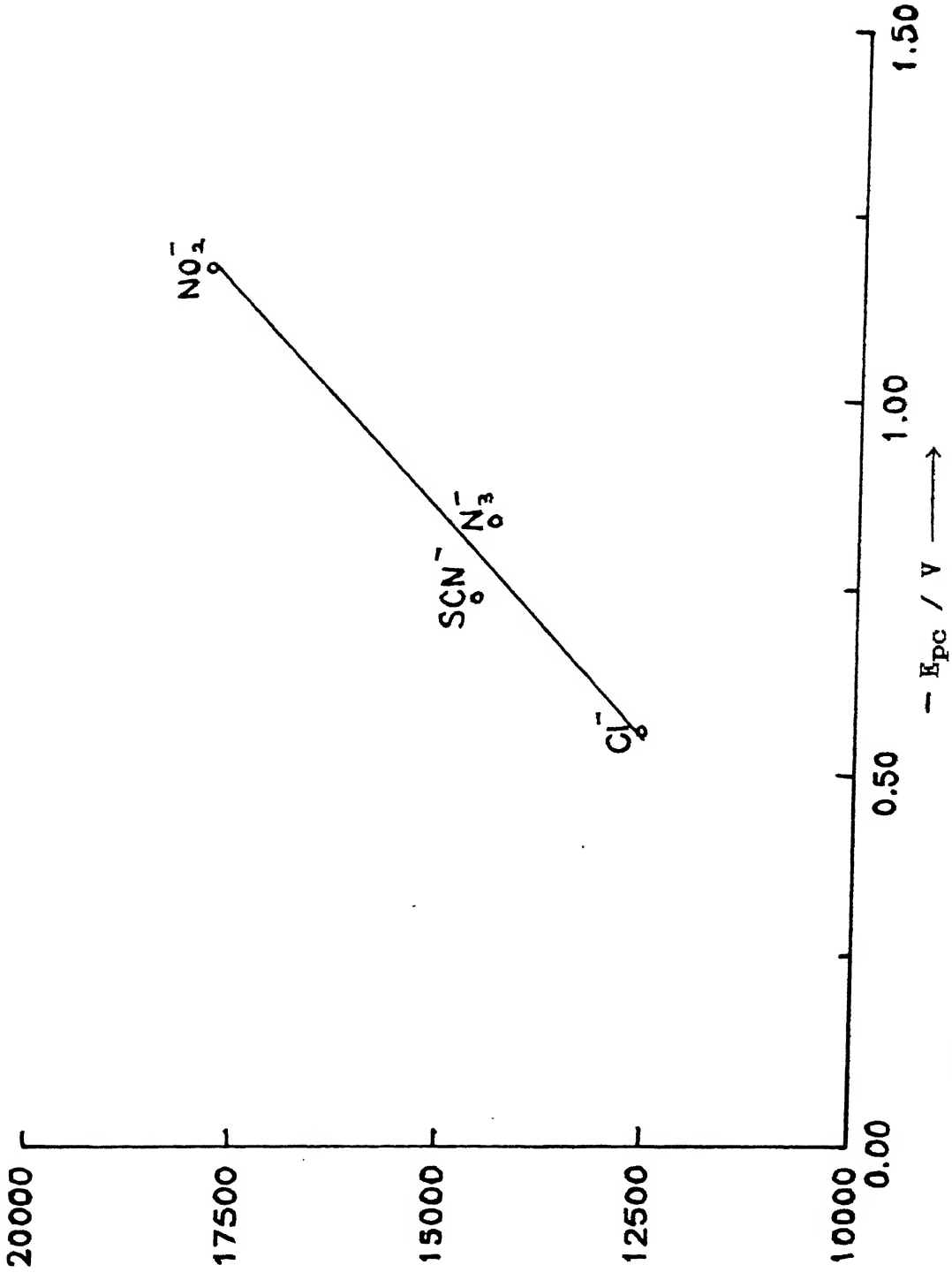

Figure 4.6 The least squeres plot of λ_{max} vs. E_{pc} for $[Co(bpb)X_2]^{1-}$ (X = Cl^-, N_3^-, SCN^-, NO_2^-) complexes.

Chapter 2.

(v) This work gives an impetus for the necessary modification of the ligand superstructure to prevent ligand oxidation and hence the possibility of stabilizing +4 oxidation state of cobalt. The above situation would enable the present synthetic non-porphyrin N_4 bis(picolinamide) ligand system to exhibit a versatile electron-transfer series of relevance to biological processes.[198-200]

CHAPTER 5

In Chapters 2-4 we have described the synthesis and properties of the manganese(III), iron(III), cobalt(III) complexes of tetradentate bis(picolinamide) ligand system with various axial ligand(s) that exhibit rich redox chemistry. Except for ring chloro/methyl substitution, so far we kept the in-plane tetradentate ligand constant. The in-plane ligand structure was such that it provides a grossly planar coordination in the equatorial plane to its metal complexes.[56,57,59-63,161]

In this Chapter we describe the coordinating behavior of two new bidentate ligands, 2-pyridinecarboxamidobenzene (H(pb)) and 2-pyridinecarboxamido2,4,5-trichlorobenzene (H(ptb)) which on deprotonation can provide two amide nitrogen donors and two pyridine nitrogen atoms, in their bis-chelate complexes. The overall nature of these two ligands are analogous to bpb(2-) and bpc(2-). Thus, in essence, keeping the type of donor atoms invariant we have introduced flexibility in the in-plane ligand. It was anticipated that pb(2-) and ptb(2-) ligands might well lead to imposed stereochemistry[201,202] on the metal ions due to non-planar arrangement in their bis-chelates. In this regard copper(II) ion would be an ideal choice to test this hypothesis.[203]

The purpose of the work presented in this chapter is primarily to investigate the stereochemical changes around the copper(II) center caused by ligand structure modification utilizing bpb(2-), pb(2-), and ptb(2-) pyridine amide ligands. Absorption and EPR spectroscopic and electrochemical techniques have been used to monitor this effect.

Additionally, we note that there has been a great deal of

research activity in the copper coordination chemistry of bleomycins(BLM)[47,65,66,68,70,204,205] and the interaction of BLM-metal chelates with DNA. The metal binding site of BLM contains the core donors of imidazole, deprotonated amide nitrogen, pyrimidine(pyridine-N) and secondary amine joined to a terminal primary amine. The structure of the present ligands partially fulfills the ligating sites required by BLM. Our endeavour is set in this backgroud.

5.1 Experimental Section

5.1.1 Solvents and Reagents

Dichloromethane was purified by washing with saturated sodium bicarbonate solution followed by five or six times with water and keeping over anhydrous calcium chloride for 24h and distilled. Aniline was vaccum distilled before use. Dimethylsulfoxide (DMSO) was purified by distillation over BaO. 2,4,5-Trichloro-nitrobenzene was from Aldrich Chemicals Co. and was used as received. Details of solvent purification and starting materials other than that stated above are already discussed in Chapter 2 (Section 2.1.1).

5.1.2 Measurements

The details for all measurements are that stated in Chapter 2 (Section 2.1.2).

5.1.3 Molecular Orbital Calculations

Extended Hückel Molecular Orbital (EHMO) calculational details followed those described by Ammeter and coworkers[206]. To obtain reasonable diagonal matrix elements for a metal centre we

carried out complete charge iterative calculations on our model at each conformation. Madelung parameters needed for the self-consistent charge calculations were taken from the literature[207]. At self-consistency the metal atom carried a charge of 0.67+(ω = 0°), 0.68+(ω = 30° and 60°) and 0.69+(ω = 90°). These calculations resulted in converged metal H_{ii}'s.

5.2 Syntheses of Ligands

The synthesis of the ligand H_2(bpb) was described in Chapter 2 (Section 2.2.4). The synthesis of 2-pyridinecarboxamidobenzene (H(pb)) is reported in the literature[208]. However, we have developed a straightforward procedure modifying the reported procedure for H_2(bpb). A similar procedure was employed in synthesizing 2-pyridinecarboxamido-2,4,5-trichlorobenzene(H(ptb)) which is synthesized here for the first time.

5.2.1 Synthesis of 2,4,5-Trichloroaniline

Solid stannous chloride dihydrate (23.0 g, 0.10 mol) was added slowly to a stirred mixture of 1,2,4-trichloro-5-nitrobenzene (7.0 g, 0.03 mmol) and concentrated HCl (75 mL). The solution was boiled for 3-4 h and cooled to room temperature. A solution of 50 g of NaOH in 100 mL water was added slowly with stirring. The mixture was warmed and filtered through a Büchner funnel and washed with 50 mL of water. The solid thus obtained was recrystallized from aqueous-methanol. The product was dried in vaccuo (yield 5.5 g, ~ 90%). Melting point 93°C.

^{1}H NMR ($CDCl_3$): δ 6.81 (s, 1 H), 7.23 (s, 1 H), 5.10 (s, 2 H).

5.2.2 2-Pyridinecarboxamidobenzene (H(pb))

The ligand H(pb) was prepared by adding a solution of aniline (5.0 g, 0.053 mol) in pyridine (7 mL) dropwise to a stirred solution of pyridine-2-carbxylic acid (5.8 g, 0.046 mol) in pyridine (8 mL) at room temperature. The resulting solution was stirred for 15 min and afterwards the temperature was gradually increased to ~ 100°C using a water bath. To this solution triphenyl phosphite (14.2 g, 0.045 mol) was added dropwise with stirring. Heating and stirring were continued for a further 5 h. The pyridine was then distilled off using a rotary evaporator. The resulting oil was dissolved in chloroform (20 mL), washed three times with water, four times with saturated sodium bicarbonate solution, and then again three times with water. The resulting chloroform solution was evaporated in vacuo and a oil resulted which was washed with water several times to remove unreacted aniline. The solid thus obtained was recrystallized from chloroform/n-hexane to give white crystalline powder of H(pb) (yield 6.5 g ~ 65 %). Melting point 76°C (reported value[208] 76-77°C). IR data: ν_{N-H} 3335 cm^{-1}, ν_{amideI} 1671 cm^{-1}.

^1H NMR ($CDCl_3$): δ 7.28(m) and 7.84(t)(7 H), 8.29(d, 1 H), 8.57 (d, 1 H), 10.00 (br, 1 H)

5.2.2 2-Pyridinecarboxamido-2,4,5-trichlorobenzene (H(ptb))

Triphenyl phosphite (8 g, 25.78 mmol) was added dropwise to a stirred warm solution of picolinic acid (3.1 g, 25.18 mmol) and 2,4,5-trichloroaniline (5.0 g, 25.45 mmol) in pyridine (25 mL). The resulting solution was heated to ~ 100°C for 4 h. The brown solution thus obtained was kept overnight at room temperature

affording the product as fine needles. The product was filtered and washed with methanol to afford fibrous H(ptb) (yield 4.1 g, ~ 53%). Recrystallization was done from hot methanol. Melting point 166°C. IR data: ν_{N-H} 3320 cm^{-1}, ν_{amideI} 1690 cm^{-1}.

^1H NMR ($CDCl_3$) : δ 7.50(m, 2 H), 7.90(t, 1 H), 8.20(d, 1 H), 8.62 (d , 1H), 8.86 (s, 1H), 10.65 (br, 1H)

5.3 Syntheses of Complexes

The complex [Cu(bpb).H_2O] was synthesized following a reported procedure by warming equimolecular mixture of copper(II) acetate monohydrate and H_2(bpb) in aqueous ethanol[53]. The syntheses of the two new complexes are described below.

5.3.1 [Cu(pb)$_2$.H_2O]

To a solution of H(pb) (0.3 g. 1.51 mmol) in ethanol (5mL) was added a solution of $CuSO_4.5H_2O$ (0.19 g, 0.76 mmol) in water (1 mL) and 25% ammonia solution (3 mL). The resulting green solution was warmed on a water bath for 0.5 h. The precipitate which initially formed eventually dissolved and a deep green solution resulted. Then the solution thus obtained was filtered and kept open for 4 h at room temperature. Deep green crystals that formed were filtered and washed with a small volume of 80% ethanol. The crystals were dried in vaccuo to give [Cu(pb)$_2$.H_2O] (yield, 0.22 g, ~72%). Recrystallization was done from aqueous methanol.

5.3.2 [Cu(ptb)$_2$.H_2O]

A mixture of copper(II) acetate monohydrate (0.09 g, 0.45 mmol) and H(ptb) (0.3 g, 0.99 mmol) in methanol (7 mL) were stirred for overnight at room temperature. A brown crystalline

solid was obtained. It was recrystallized from chloroform/n-hexane and dried in vacuo to afford [$Cu(ptb)_2.H_2O$] (yield, 0.2 g ~ 70 %).

5.4 Results and Discussion

5.4.1 Syntheses and Characterization

The peptide bonds in H_2(bpb), H(pb), and H(ptb) have been synthesized in high yield by the condensation of picolinic acid and the corresponding amines in pyridine using triphenyl phosphite as water scavenger.[52] The ligands were characterized by ^1H NMR and IR spectra (Experimental Section). The ^1H NMR spectrum of H(ptb) in $CDCl_3$ is shown in Figure 5.1. All the three ligands have two kinds of N donors: a pyridine N and a peptide N. The benzene ring in H(pb) and benzene ring with chloro substituents in H(ptb) are sufficient to generate enough steric hindrance so as to yield the tetrahedrally distorted copper complexes (see below). The copper complexes with deprotonated ligands have been synthesized directly from copper(II) acetate. In the synthesis of [$Cu(pb)_2.H_2O$] ammonia solution was used to deprotonate the ligand N-H proton. In the other two cases acetate ion acts as a base.

The IR spectra of all the three complexes show the absence of N-H absorptions and low-energy shift of the ν_{amideI} (Table 5.1) which indicates the co-ordination of the deprotonated ligands.[53] For all the three complexes a broad absorption at ca. 3600 cm^{-1} characteristic of ν(OH) is observed. This fact taken in conjunction with microanalytical (Table 5.2) results point toward a co-ordinated water molecule in these complexes. For

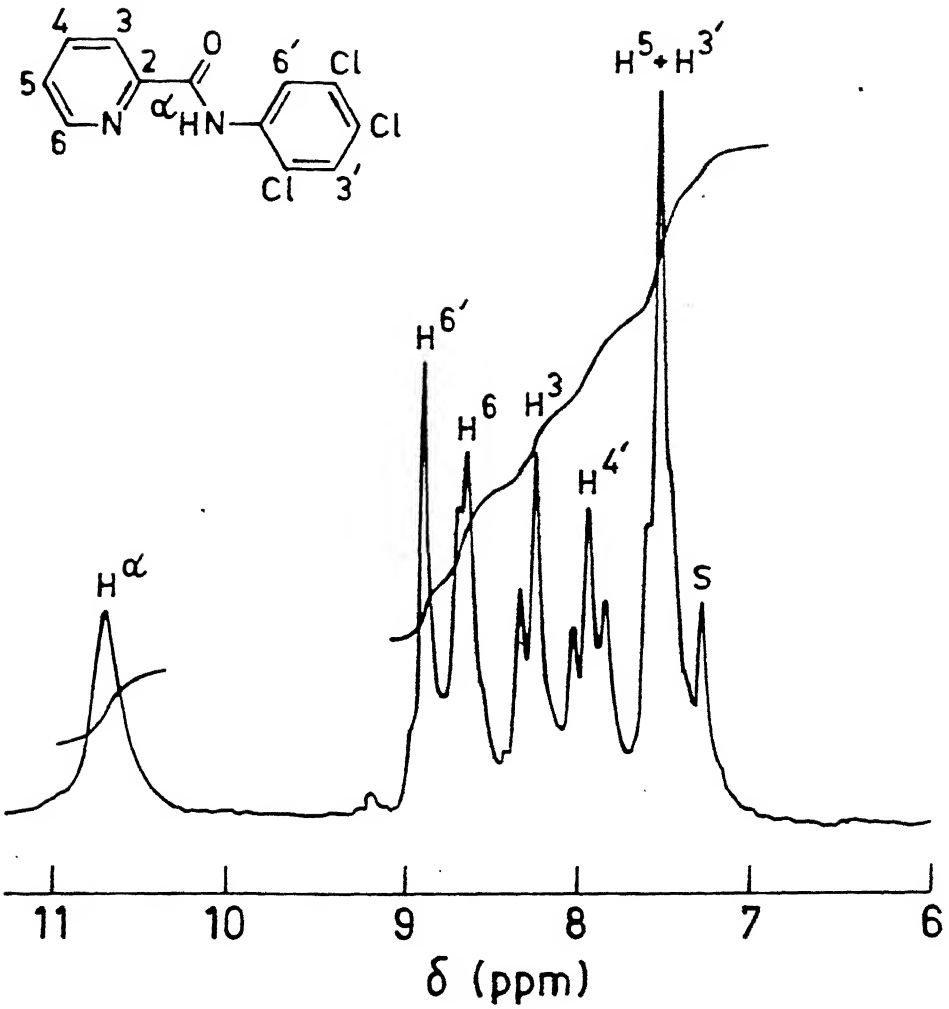

Figure 5.1 Partial ^{1}H NMR spectrum of the ligand H(ptb) in $CDCl_3$.

Table 5.1 : Molar conductance, Magnetic moment, and Selected IR Data of Copper(II) Complexes

Complex	Molar coductivity[a] Λ_M (Ω^{-1} cm^2 mol^{-1})	Magnetic moment[b] $\mu_{eff}(\mu_B)$	IR data[c] (cm^{-1}) ν amideI
$[Cu(bpb).H_2O]$[d]	4	-	1635
$[Cu(pb)_2.H_2O]$	5	1.73	1630
$[Cu(ptb)_2.H_2O]$	8	1.87	1630

[a] Solvent: DMF. Expected 1:1 electrolyte range in DMF: 65-90 Ω^{-1} cm^2 mol^{-1}.[123]

[b] Measured in DMF solution using Evans' method.[111]

[c] In KBr disk (4000-600 cm^{-1}).

[d] Due to poor solubility in DMF magnetic moment in solution could not be determined. Solid state value μ_{eff}=2.00 was reported.[56]

Table 5.2 : Microanalytical Data[a] of Copper(II) Complexes

Complex	Empirical Formula	% C	% H	% N
$[Cu(bpb).H_2O]$	$C_{18}H_{14}N_4O_3Cu$	54.80 (54.33)	3.70 (3.55)	14.20 (14.05)
$[Cu(pb)_2.H_2O]$	$C_{24}H_{20}N_4O_3Cu$	60.20 (60.55)	4.40 (4.25)	11.60 (11.80)
$[Cu(ptb)_2.H_2O]$	$C_{24}H_{14}N_4Cl_3O_3Cu$	42.10 (42.20)	2.40 (2.05)	8.10 (8.20)

[a] Values in parentheses are calculated ones

[Cu(bpb).H_2O] it has been confirmed from X-ray structural analysis.[208] The very low solution electrical conductivity values in DMF solution (Table 5.1) indicate that these copper(II) complexes are non-conducting. At room-temperature the effective magnetic moments in DMF solutions are ~ 1.8, which is typical of S = 1/2 Cu^{II} (Table 5.1).

5.4.2 Absorption Spectra

In the 1000-500 nm region [Cu(bpb).H_2O], [Cu$(pb)_2$.H_2O], and [Cu$(ptb)_2$.H_2O] exhibit in DMF solution two shoulders of d-d transition origin, as revealed from their low intensities (Figure 5.2, Table 5.3). One clearly sees that the d-d absorptions of [Cu$(pb)_2$.H_2O] and [Cu$(ptb)_2$.H_2O] are considerably red-shifted compared to [Cu(bpb).H_2O] which is a distorted square-based pyramid as revealed by X-ray crystallography (see above). Close inspection of the spectral data in Table 5.3 reveals certain clues related to the solution structures of these complexes. An interesting observation in the spectral behaviour of [Cu(bpb).H_2O], [Cu$(pb)_2$.H_2O] and [Cu$(ptb)_2$.H_2O] is the difference in the intensity of the d-d transition band(s). The enhanced intensity in [Cu$(pb)_2$.H_2O] and [Cu$(ptb)_2$.H_2O] is suggestive of distortion from the tetragonal stereochemistry towards tetrahedral, apparently caused by steric constraints. Similar enhancement of intensity due to distortion has been reported for a variety of four-coordinate copper(II) complexes having CuN_4 unit.[209-214]

To investigate the effect of solvent molecules in the co-ordination zone of all the three complexes we have examined their

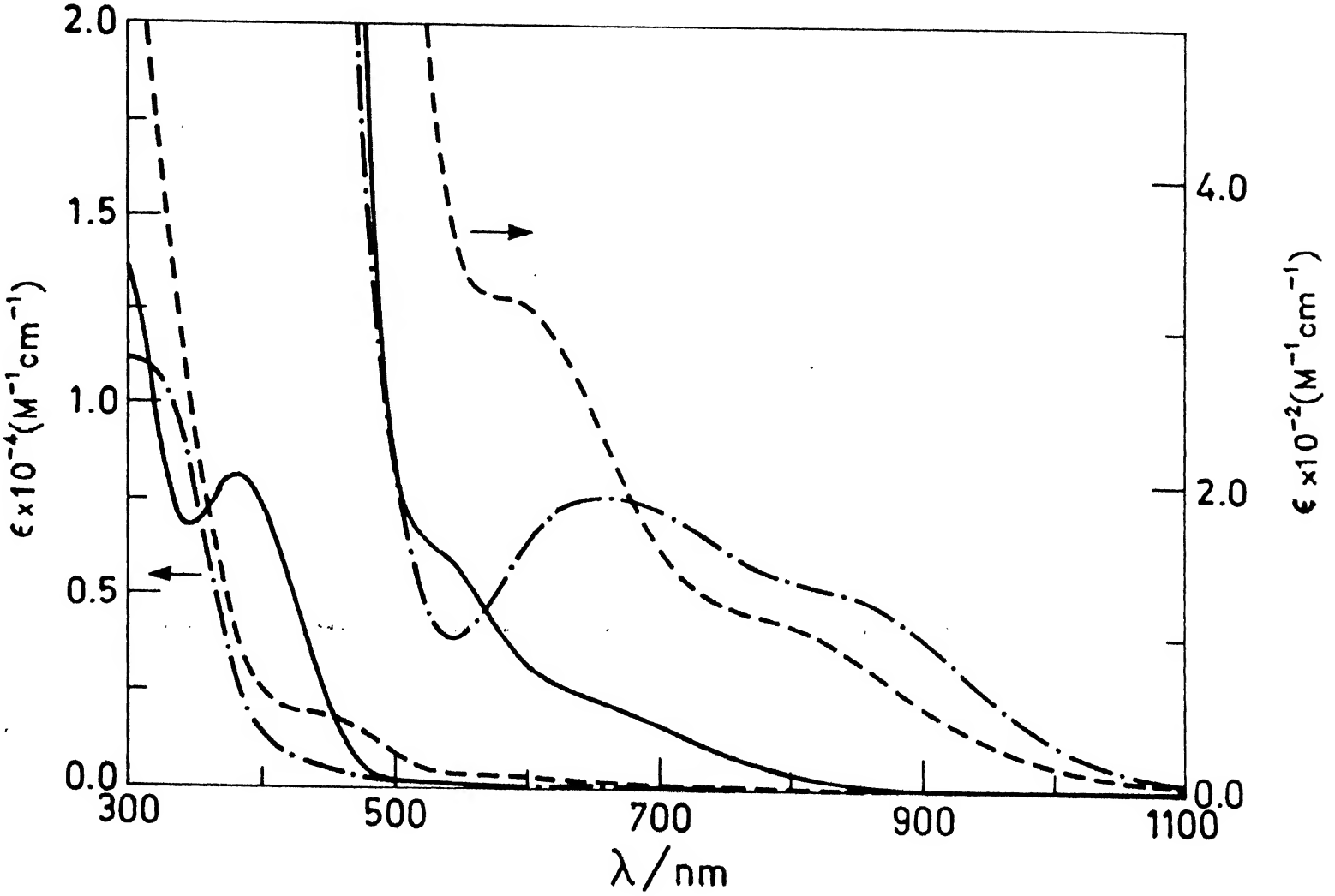

Figure 5.2 Electronic spectra of [Cu(bpb).H_2O] (——) and [$Cu(pb)_2.H_2O$] (- - -) in DMF solution and [$Cu(pb)_2.H_2O$] (—•—•—) in pyridine solution.

Table 5.3 : Electronic Spectral[a] Data of Copper(II) Complexes

Complex	Solvent	λ_{max},nm,(ϵ,$M^{-1}cm^{-1}$)
[Cu(bpb).H_2O]	DMF	660(sh)(55)[b],545(sh)(145), 382(8 000), 302(13 000)
	pyridine	785(sh)(40), 558(150), 395(8 600)
[Cu(pb)$_2$.H_2O][c]	dichloro-methane	800(sh)(120),600(sh)(330), 442(2 000), 320(sh)(6 500)
	MeCN	800(sh)(100),585(sh)(350), 434(sh)(2 200), 315(sh) (9 100), 254(23 800), 240(23 900)
	DMF	790(sh)(110),580(sh)(320), 430(sh)(2,000),
	DMSO	785(sh)(115),606(220), 435(sh)(660), 283(23 789)
	pyridine	850(sh)(120),676(190), 450(sh)(760), 310(sh) (11 100)
[Cu(ptb)$_2$.H_2O][c]	DMF	830(sh)(60),603(350) 424(1 900),290(sh)(13 000)
	pyridine	815(sh)(100), 612(200), 420(sh)(1400)

[a] Spectral measurments in the range 500 - 1100 nm were made at ~ 10^{-3} M and for the range 200 - 500 nm were made at ~ 10^{-4} M.

[b] sh = shoulder.

[c] Electronic spectral data in Nujol mull ; [Cu(pb)$_2$.H_2O], 820 nm, 620 nm ; [Cu(ptb)$_2$.H_2O], 980 nm, 620 nm.

behavior in a number of solvents of varying coordinating capability. For [Cu(bpb).H_2O] the shift of the d-d bands towards lower energy is indicative of axial ligand coordination.[47,65,66,215] Barring the behavior in pyridine solution there is not much shift (Table 5.3) in the d-d band positions for [Cu(pb)$_2$.H_2O]. The observed shift in the positions of the two shoulders could be due to minor perturbation of the electronic structure of the copper center by the solvent molecules.[47,65,66,215] Interestingly, for [Cu(pb)$_2$.H_2O] an appreciable red shift in the absorption positions was observed in pyridine. We believe that this is due to the imposed stereochemical rigidity of the structure of [Cu(pb)$_2$.H_2O] in pyridine solution where solvent molecules cannot approach the metal centre due to steric reasons and hence favours considerably towards tetrahedral distortion. It is understandable that for DMF/DMSO molecules it would not be that problem to approach the metal center but it is expected to be in the case of pyridine due to steric reasons (aromatic ring - pyridine ring interaction). It is to be noted that unlike [Cu(pb)$_2$.H_2O] the complex [Cu(ptb)$_2$.H_2O] does not vary much in going from DMF to pyridine.

We decided to study the absorption spectral behavior in the solid-state as well (Figure 5.3, Table 5.3). The absorption spectrum of [Cu(bpb).H_2O] dispersed in mineral oil mull exhibits (Figure 5.3, Table 5.3) a broad envelop at ~ 450 nm in the visible region. Low energy absorption(s) could not be observed. On the other hand, [Cu(pb)$_2$.H_2O] and [Cu(ptb)$_2$.H_2O] exhibit almost similar (for [Cu(ptb)$_2$.H_2O] the lowest energy band is appreciably

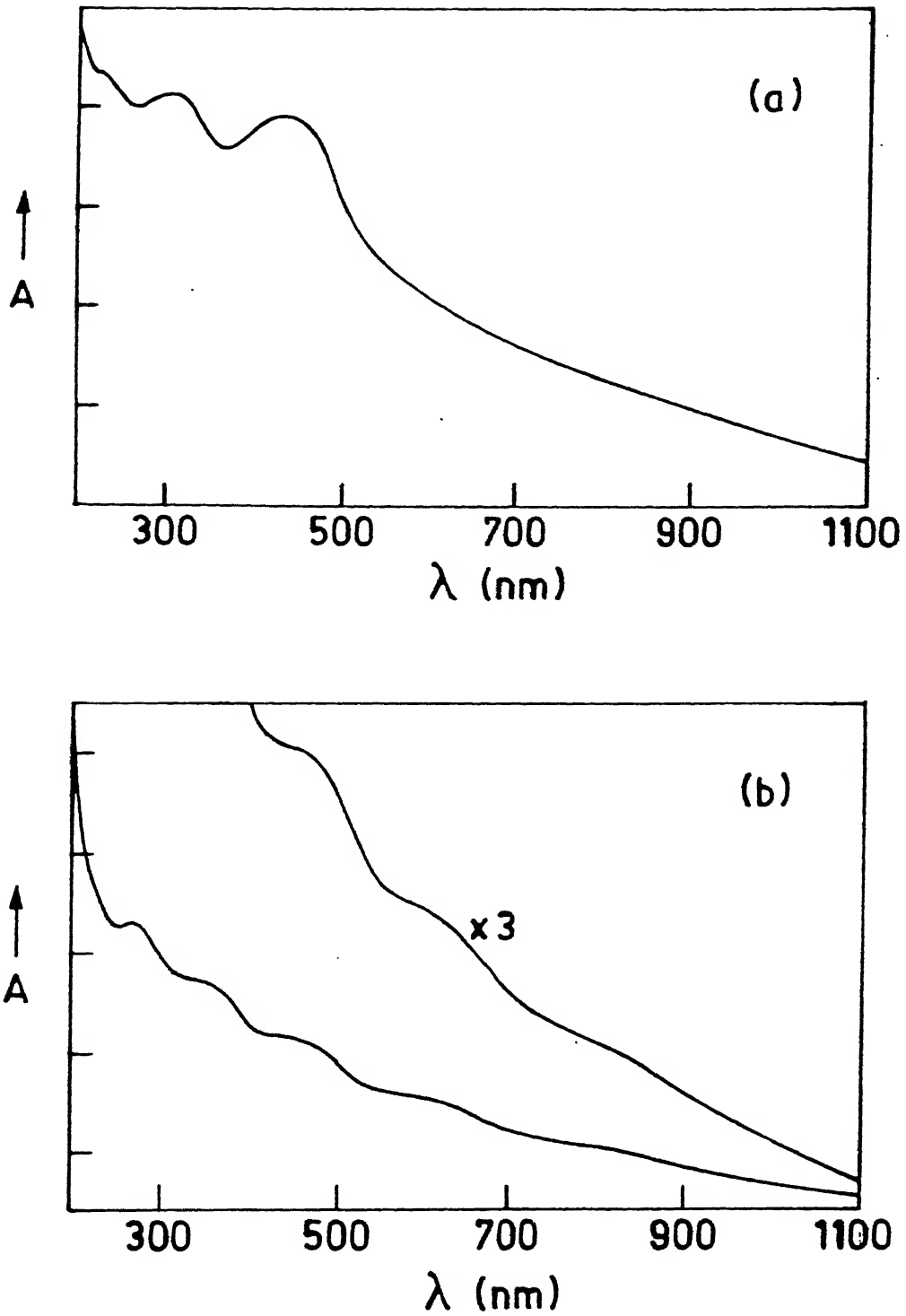

Figure 5.3 Electronic spectra of [Cu(bpb).H_2O] (a) and [Cu(pb)$_2$.H_2O] (b) in nujol mull.

red shifted in the solid state) absorption spectral positions to that obtained in solution (Figure 5.2, Table 5.3), implying that the solid state structures are retained in solution. The shift of the absorption band(s) (in the region 500-1000 nm) to the lower energy in going from solution (pyridine exerts a special effect, stated above) to the solid state is consistent with increased axial interaction in solution at Cu^{II}.[47,65,66,215] Since $[Cu(pb)_2.H_2O]$ and $[Cu(ptb)_2.H_2O]$ show substantial tetrahedral distortion from the limiting planar geometry, its ligand field absorptions must be appreciably red-shifted. That is exactly what we have observed. These results indicate that the tetrahedral distortion is a little larger in the solid state than in solution, suggesting that there is some intermolecular force which enhances the distortion in the crystal. However, we are surprised to note that the extent of tetrahedral distortion in pyridine medium is larger than that in the solid state. Absorptions in this spectral region are exhibited by other tetrahedrally distorted $Cu^{II}N_4$ chromophores.[209-212,216-219]

It is interesting to note that the visible absorption spectrum in DMF solution of $[Cu(ptb)_2.H_2O]$ but not $[Cu(pb)_2.H_2O]$ resembles that reported for Cu(II)-BLM[202] even though in both $[Cu(pb)_2.H_2O]$ and $[Cu(ptb)_2.H_2O]$ the copper centre is expected to have similar structure in the first co-ordination sphere. It is thus evident that two structurally similar species [$[Cu(pb)_2.H_2O]$ and $[Cu(ptb)_2.H_2O]$] might exhibit different spectroscopic behaviour depending on finer structural detail.

5.4.3 EPR Spectral Studies

To extract complementary information on the degree of distortions towards tetrahedral in [Cu(pb)$_2$.H$_2$O] and [Cu(ptb)$_2$-H$_2$O], EPR studies were performed. Representative EPR spectra of these copper(II) complexes in solution obtained at liquid dinitrogen temperature are shown in Figure 5.4. The spectra for [Cu(bpb).H$_2$O] and [Cu(ptb)$_2$.H$_2$O] in Figure 5.4 also quite clearly show superhyperfine structure (9 lines) due to four equivalent (to within the line-width) in-plane nitrogen atoms; the values of $A_{\parallel}^{N}$ can also be obtained from the parallel features (Table 5.4). These data in DMF solutions are consistent with a distorted square-pyramidal geometry (axial symmetry) about copper with an unpaired electron in the $d_{x^2-y^2}$ orbital. The EPR spectra of [Cu(pb)$_2$.H$_2$O] in pyridine solution is quite different from that obtained in others solvents (Figure 5.4). The small but significant variation in g values as obtained here (Table 5.4) provides information about distortion about distortion in the geometry around copper(II).[211-214] This is supported by the variation in the position of the ligand-field feature; the higher g the lower is λ_{max}.[214] Similar observations made for copper(II) complexes[214] have been ascribed to increasing tetrahedral distortion.

Kivelson and Neiman[220] have pointed out that compounds having $g_{\parallel} > 2.3$ are ionic compounds, whereas those with $g_{\parallel} < 2.3$ are covalent in character. The $g_{\parallel}$values of the present complexes fulfill the latter criterion. For the axial spectra of copper(II) complexes ($g_{\parallel} > g_{\perp} > 2.03$) the g values are related by the expression[221] $G = (g_{\parallel} - 2)/(g_{\perp} - 2) \sim 4.01$. The cryogenic DMF

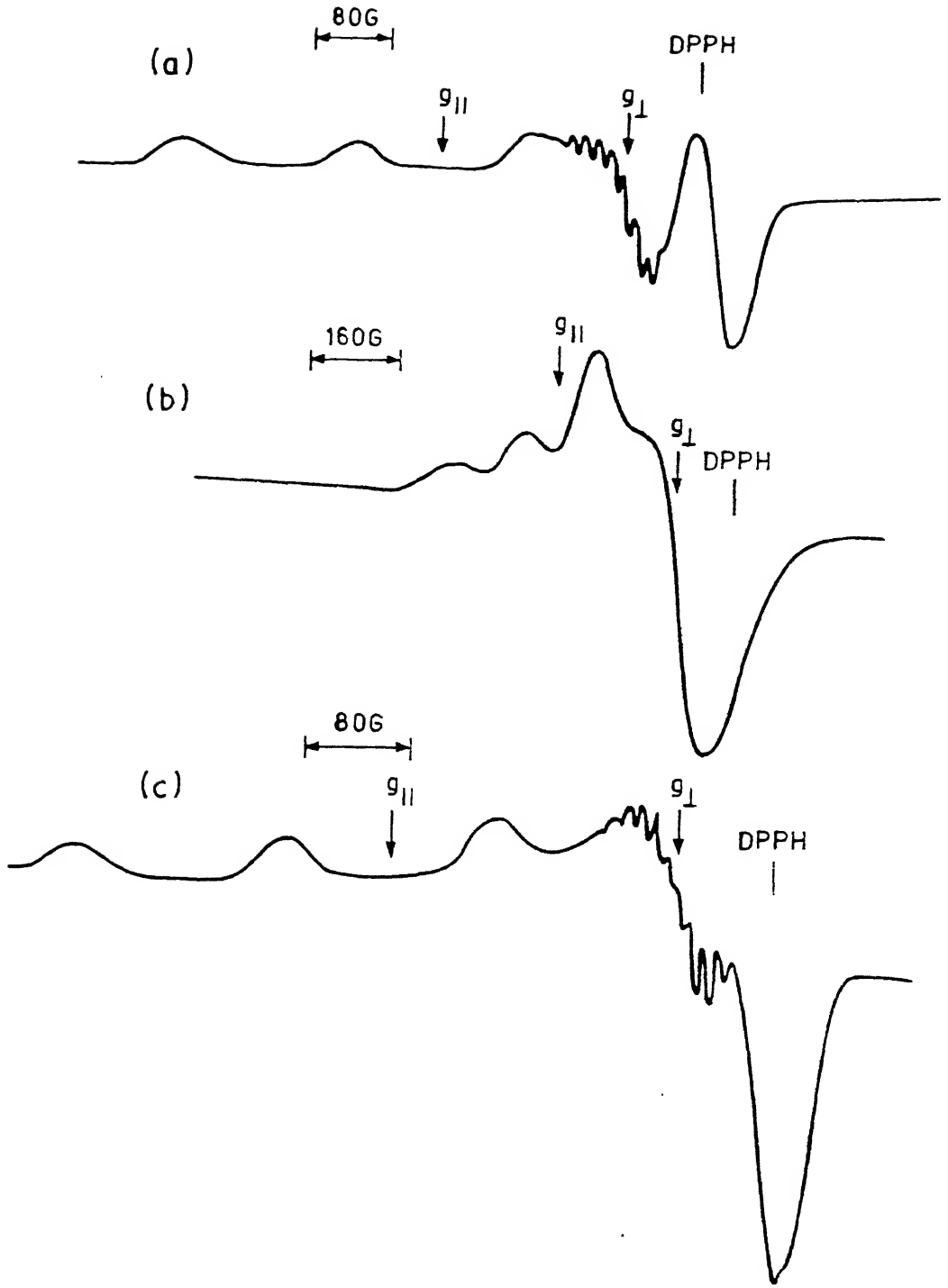

Figure 5.4 EPR spectra of (a) [Cu(bpb).H_2O] in DMF, (b) [$Cu(pb)_2$.H_2O] in pyridine and (c) [$Cu(ptb)_2$.H_2O] in DMF at liquid dinitrogen temperature

Figure 5.4 : X-Band EPR Spectral[a] Data

Complex	Solvent	$g_{\parallel}$	$g_{\perp}$	$A_{\parallel}$(G)	$A_{\parallel}^{N}$(G)	α^2
[Cu(bpb).H_2O]	DMF	2.191	2.050	200	15	0.81
	pyridine	2.197	2.057	190	-	
[Cu(pb)$_2$.H_2O]	DMF	2.216	2.055	168	-	0.75
	pyridine	2.242	2.066	128	-	0.67
[Cu(ptb)$_2$.H_2O]	DMF	2.210	2.055	168	12	0.74
	pyridine	2.218	2.043	145	-	

[a] EPR spectra were taken in liquid dinitrogen temperature.

solution EPR spectra of [Cu(bpb).H_2O], [Cu(pb)$_2$.H_2O] and [Cu(ptb)$_2$.H_2O] exhibit G values of 3.92, 4.04 and 3.92 respectively. Because the G values are very close to 4, the present ligands are comparatively weak field in character.

The tendency for $g_{\parallel}$ to increase and $A_{\parallel}$ to decrease with an increase in the degree of tetrahedral distortion has been reported previously for structurally well-characterized complexes of copper(II).[211-214] The quotient $g_{\parallel}$ / $A_{\parallel}$ is a convenient empirical index of tetrahedral distortion,[213] as measured by the dihedral angle between each of the two co-ordination planes defined by a CuN_2 moiety (see below). The dihedral angle between the two N-Cu-N planes progressively change from 0 (square planar) to 90° (tetrahedral). In DMF solution the value of this quotient is 110 cm for [Cu(bpb).H_2O] and 132 cm for both [Cu(pb)$_2$.H_2O] and [Cu(ptb)$_2$.H_2O]. In pyridine solution for [Cu(pb)$_2$.H_2O] this value is 175 cm and for [Cu(ptb)$_2$.H_2O] this value is 153 cm. Thus there is an observable distortion towards tetrahedral in [Cu(pb)$_2$.H_2O]. With available data thus far obtained we are not in a position to make a comment on the different behavior of [Cu(pb)$_2$.H_2O] and [Cu(ptb)$_2$.H_2O] in pyridine solution.

Interestingly, when one uses the relationship between $g_{\parallel}$ and ω as proposed by Addison *et al.*[211] For [Cu(pb)$_2$.H_2O] the dihedral angle is estimated to be ~ 55°.

The EPR spectra of [Cu(bpb).H_2O], [Cu(ptb)$_2$.H_2O] and [Cu(ptb)$_2$.H_2O] are closely similar to[202] that of Cu(II)-BLM ($g_{\perp}$ = 2.058, $g_{\parallel}$ = 2.213, $A_{\parallel}$ = 184 x 10^{-4} cm^{-1}).

5.4.4 Electrochemistry

Table 5.5 collects the results of the electrochemical investigation on the present complexes and Figure 5.5 shows representative current-voltage responses obtained from applying cyclic voltammetry to these complexes. Barring the situations for $[Cu(pb)_2.H_2O]$ in dichloromethane and pyridine the separation of the anodic (E_{pa}) and cathodic (E_{pc}) peaks were 80-90 mV (scan rate = 50 mVs^{-1}) in all other solvents utilised in this work and peak current ratios were near unity. All these parameters are diagnostic for a nearly reversible[222,223] one-electron reduction process (Section 2.1.2). The one-electron nature of this reduction process was confirmed by controlled-potential coulometric measurements on $[Cu(pb)_2.H_2O]$ (Table 5.5). On coulometric reduction, as expected, the d-d transitions disappear (Figure 5.6). The electronic spectra of purple colored reduced solution shows an intense absorption maxima (λ_{max} 460nm; ϵ 2900 M^{-1} cm^{-1}) possibly due to metal-->ligand charge transfer transition.[224,215]

In $[Cu(bpb).H_2O]$ the copper centre is square-pyramidal and from the absorption and EPR spectral analysis it is reasonable to believe that in both $[Cu(pb)_2.H_2O]$ and $[Cu(ptb)_2.H_2O]$ the copper centres are effectively in distorted tetrahedral CuN_4 co-ordination. From the electrochemical viewpoint, the copper(II) to copper(I) reduction in a (pseudo)tetrahedral environment is expected to occur at quite positive potential.[225-227] The outcome of this investigation is no exception (Table 5.5), when one compares the redox potentials for $[Cu(bpb).H_2O]$, $[Cu(pb)_2.H_2O]$ and $[Cu(ptb)_2.H_2O]$ in a given solvent (DMF). In going from

Table 5.5 : Electrochemical[a] Data for the Copper(II) Complexes

Complex	Solvent	Cu^{II}/Cu^{I} couple	
		E_f/V	ΔE_p/mV
[Cu(bpb).H_2O]	DMF	-1.10	80
	pyridine	-1.10	120
[Cu(pb)$_2$.H_2O][b]	dichloro-methane	-0.53	100
	MeCN	-0.52	80
	DMF	-0.47	90
	DMSO	-0.44	90
	pyridine	-0.60[c]	140
[Cu(ptb)$_2$.H_2O]	DMF	-0.40	70
	pyridine	-0.39	100

a Supporting electrolyte $[Bu_4^nN]ClO_4$ (0.15 M); all potentials are referenced to SCE ; $E_f=0.5(E_{pc} + E_{pa})$; E_{pc} and E_{pa} are the cathodic and anodic peak potentials respectively; scan rate is 50 mV s^{-1} at a glassy carbon electrode.

b Coulometric data in DMF are averages of at least three independent measure ments; applied potential -0.7V; n=1.05 where n= coloumb count at the end of electrolysis / calculated coloumb count for $1e^-$ transfer.

c E_{pc} is given as peak-to-peak seperation (ΔE_p) is high.

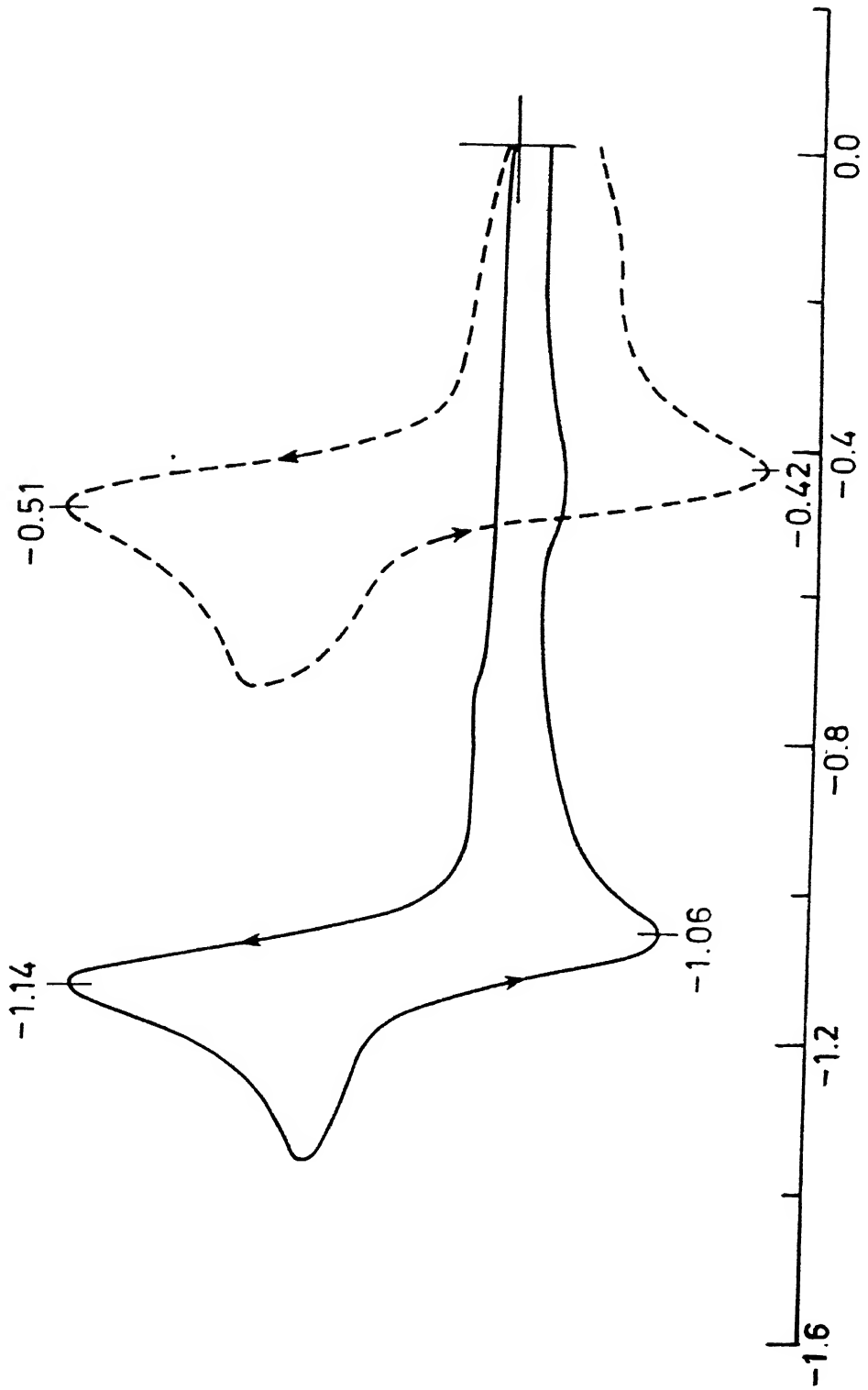

Figure 5.5 Cyclic voltammograms of [Cu(bpb).H_2O] (——) and [Cu(pb)2.H_2O] (- - -) in DMF. Condition: scan rate 50 mV s^{-1}; glassy carbon working electrode; supporting electrolyte TBAP.

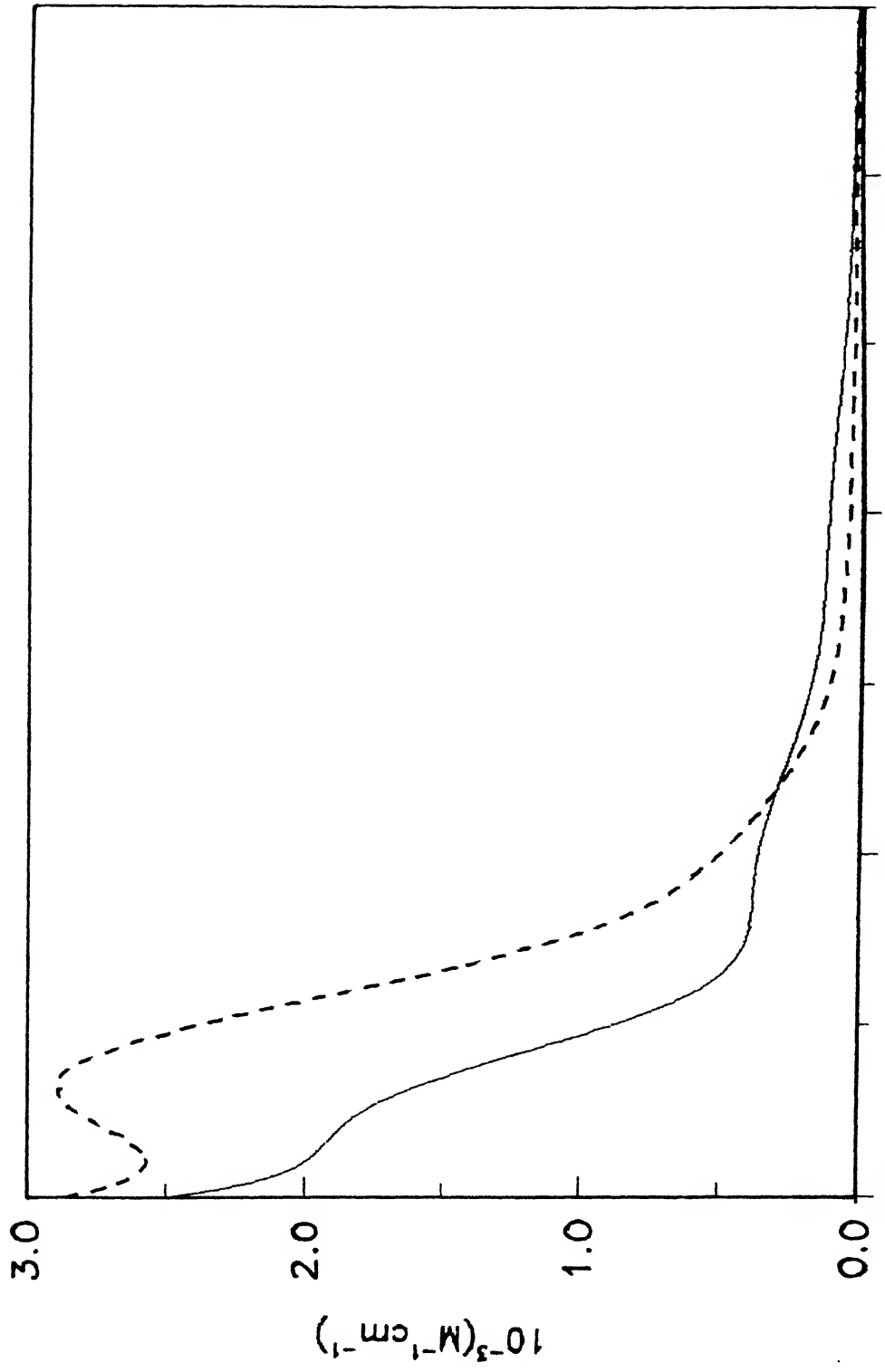

Figure 5.6 Electronic spectra of $[Cu(pb)_2.H_2O]$ before (——) and after (- - -) coulometric reduction in DMF solution.

[Cu(bpb).H_2O] to [$Cu(pb)_2.H_2O$] and from [Cu(bpb).H_2O] to [$Cu(ptb)_2.H_2O$] the redox potentials shift to positive potential by 0.63 V and 0.70 V respectively. This is a remarkable result to show the importance of the structural effect on Cu^{II}/Cu^{I} redox potential for a given type of ligand system. To the best of our knowledge, the observed shift in the redox potentials in going from effectively tetragonal to effectively tetrahedral, is the largest.

We decided to investigate the effect of the solvation energy on the Cu^{II}/Cu^{I} redox thermodynamics of [$Cu(pb)_2.H_2O$]. Here the Cu^{II}/Cu^{I} potentials shift to less cathodic values in changing the solvent series: pyridine, dichloromethane, MeCN, DMF and DMSO (Table 5.5). At a first glance, it is reasonable to anticipate that the poorly co-ordinating solvent dichloromethane will give rise to highest potential (more tetrahedral distortion) and strongly co-ordinating DMF/DMSO/pyridine to exhibit lowest potential (more tetragonal distortion). Barring the case in pyridine this is in sharp contrast to what has been observed. The reduction potential trend observed here could be explained if we invoke the factors influencing the solvation enthalpies[228-230] of the two oxidation states involved in the redox process. The solvents that hydrogen-bond strongly the mononegatively charged Cu(I) species is expected to stabilise this oxidation state over the Cu(II) state. This hydrogen-bonding interaction of the solvents is related to their dielectric constant. Since the free energy of solvation is proportional to z^2/r (z = charge number and r = the ionic radius), small ions of high charge number are strongly stabilised in polar solvents. Thus more negative the

value of the solvation energy more positive the values of E_f

The reduction potentials of $[Cu(pb)_2.H_2O]$ and $[Cu(ptb)_2.H_2O]$ in DMF are -0.47 V and -0.40 V respectively. Interestingly, these values are close to the value reported for Cu(II)-BLM (-0.52 V).[66]

5.4.5 Electronic Structural Studies

From X-ray structural,[56] absorption and EPR spectral and electrochemical results we see that in the crystalline state as well as in DMF solution the structure of $[Cu(bpb).H_2O]$ is tetragonal. In contrast, the solution structure of $[Cu(pb)_2.H_2O]$ and $[Cu(ptb)_2.H_2O]$ is distorted towards tetrahedral. We conclude by examining structural preferences based on relative electronic energies. This has been achieved by LCAO-MO calculations performed at the extended Hückel level. We have used $[Cu(NH_2)_2(HCONH)_2]^{2-}$ as the calculational model (Figure 5.7), which simulates grossly the co-ordination environment of the present copper(II) complexes. Table 5.6 contains the diagonal matrix elements and Slater exponents for all the atoms present in the model. The Cu 3d function was taken as a linear combination of two Slater functions, with the exponents and coefficients listed in Table 5.6. The Cu-N(py), Cu-N(amide), C=O, C-H and N-H distances and the pertinent bond angles were from the X-ray structure of $[Cu(bpb).H_2O]$. The molecular plane is the xy plane and z axis is perpendicular to it. Calculations were performed for both the C_{2v} (cis planar co-ordination) / C_{2h} (trans planar co-ordination) and C_2 (variation of the dihedral angle between the two CuN_2 co-ordination planes starting from the idealised C_{2h}

Table 5.6 : Parameters used in EHMO calculation

Orbital	H_{ii}/eV[a]	1	2	C_1	C_2
H(1s)	-13.60	1.300			
C(2s)	-21.40	1.625			
C(2p)	-11.40	1.625			
N(2s)	-26.00	1.950			
N(2p)	-13.40	1.950			
Cu(3d)	-14.00	5.950	2.30	0.5933	0.5744
Cu(4s)	-11.44	1.950			
Cu(4p)	- 6.06	1.550			

[a] Used as initial guess values in charge iteration procedure.

conformation) co-ordination geometries. We see that in a planar co-ordination, C_{2h} conformation is energetically more favourable (HOMO stabilises by ca. 7 kcal/mol) compared to C_{2v} conformation. The percentage of ligand orbital participation decreases in going from C_{2v} to C_{2h}. Our calculations compare favourably to similar work.[207,231,232] However, the present results are somewhat more involved owing to the lower symmetry of the calculational model and the attendant lack of orbital degeneracy.

The effects of geometric factors on the energies of the d-block orbitals are depicted in Figure 5.8. For simplicity, orbitals are labeled according to their principal d component. Variation of dihedral angle(ω)from 0° (planar) to 90° (tetrahedral) mainly results in the energy of the $d_{x^2-y^2}$ orbital to drop much more steeply as the angle increases, while the energy of the d_{yz} orbital rises much less sharply, thus shifting the minimum of the total energy toward that of the tetrahedral structure. Also, the d_{z^2} orbital is lowest in energy in the two extreme structures. This behaviour can be traced to changes in antibonding interactions of metal and ligand orbitals. In going from ω = 0° to ω = 90° the HOMO experiences a significant energy change (~30 kcal/mol). The 3d composition of the HOMO at 0° (57% $d_{x^2-y^2}$ and 41% ligand contribution) changes to 61% $d_{x^2-y^2}$ and 26% ligand contribution at 90°. At ω= 90° the HOMO appears to be less antibonding because of the substantial decrease of ligand orbital contribution. To generate the observed co-ordination stereochemistry of [Cu(pb)$_2$.H$_2$O] in pyridine (see EPR spectral discussion) from the idealised planar configuraion, a change in

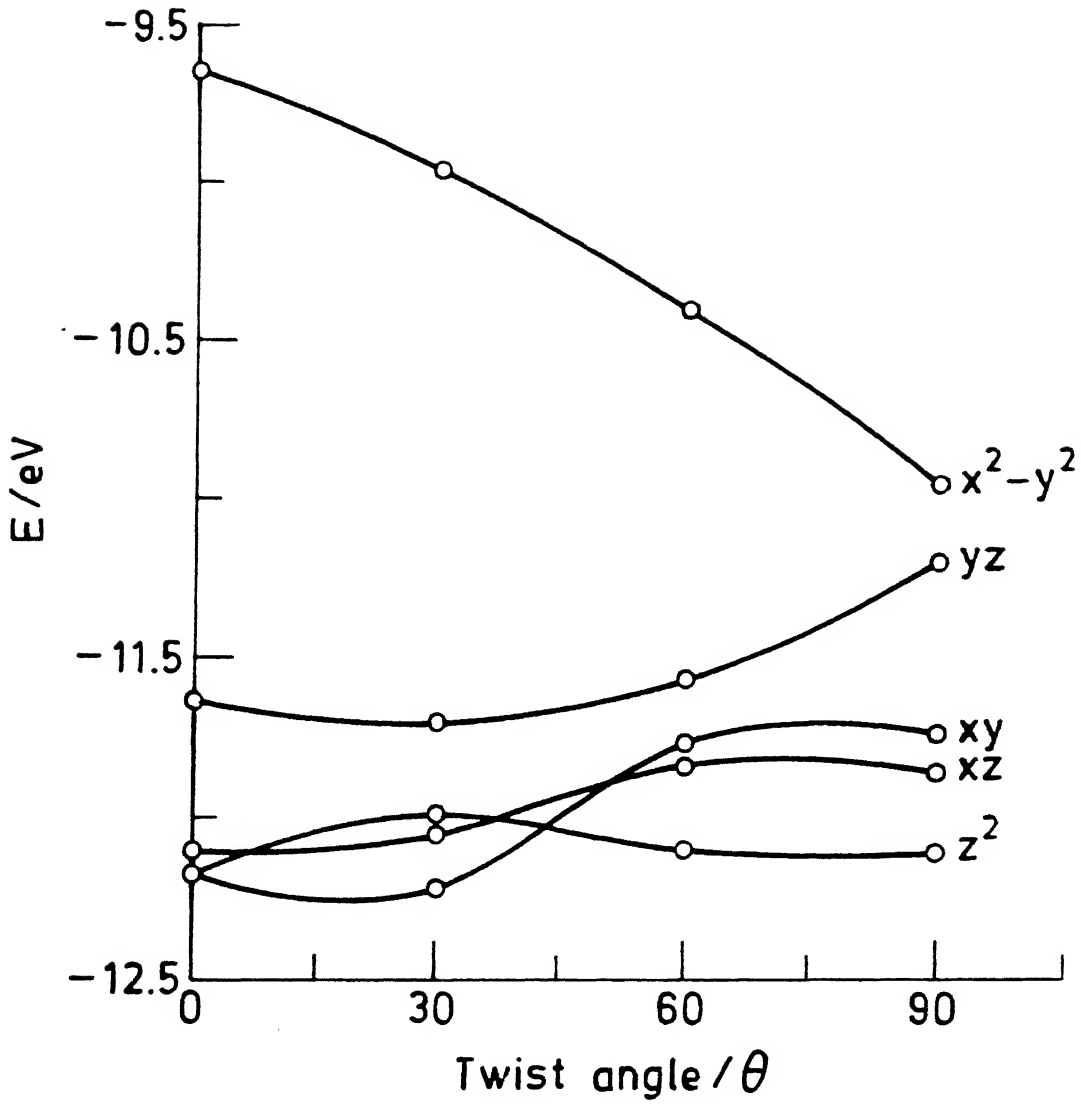

Figure 5.8 d-Orbital energy level scheme of $[Cu^{II}(NH_2)_2(NHCHO)_2]^{2-}$ as a function of dihedral angle(ω) varied between 0 and 90°.

the dihedral angle from 0° to ca. 55° is required.

We have also performed the MO calculations taking the atoms between the axes. The MO pattern remains same. However, now d_{xy} orbital become highest in energy as expected.

5.5 Conclusion

(i) This research has nicely demonstrated the fine tuning of the electronic structure of the effectively $Cu^{II}N_4$ unit using deprotonated amide ligands. From the d-d transition energies it is seen that compared to tetragonal complex [Cu(bpb).H_2O] the bis chelate complexes [Cu(pb)$_2$.H_2O] and [Cu(ptb)$_2$.H_2O] are distorted toward tetrahedral. The EPR spectral results corroborate this fact. For [Cu(pb)$_2$.H_2O] maximum distortion towards tetrahedral is seen in pyridine solution.

(ii) Cyclic voltammetric experiments neatly demonstrates how one can control the redox potentials of Cu^{II}/Cu^{I} couple of a given set of ligand donor sites by controlling the structural factors.

(iii) Extended Hückel molecular orbital calculations have been performed on model systems to show the importance of tetrahedral distortion in stabilising copper(I) state over copper(II) state.

REFERENCES

1 Sigel, H.; Martin, R. B. Chem. Rev. **1982**, 82, 385.

2 Margerum, D.W. Pure & Appl. Chem. Chem. **1983**, 55, 23.

3 Hay, R. W.; Nolan, K. B. A Specialist Periodical Report **1989**, 20, 297.

4 Kimura, E.; J. Coord. Chem. **1986**, 15, 1.

5 Levason, W.; Mcauliffe, C. A. Coord. Chem. Rev. **1974**, 12, 151.

6 Jacobs, S. A.; Margerum, D. W. Inorg. Chem. **1984**, 23, 1195.

7 Murray, C. K.; Margerum, D. W. Inorg. Chem. **1982**, 21, 3501.

8 Raycheba, J. M. T.; Margerum, D. M. Inorg. Chem. **1981**, 20, 1441.

9 Freeman, H. C.; Schoone, J. C.; Sime, J. G. Acta Cryst. **1965** 18, 381.

10 Anast, J. M.; Margerum, D. W. Inorg. Chem. **1982**, 21, 3494.

11 Bossu, F. P.; Chellappa, K. L.; Margerum, D. W. J. Am. Chem. Soc. **1977**, 99, 2195.

12 Billo, E. J. Inorg. Nucl. Chem. Lett. **1974**, 10, 613.

13 Sakurai, T.; Hongo, J. I.; Nakahara, A.; Nakao, Y. Inorg. Chim. Acta **1980**, 46, 205.

14 Koikawa, M.; Okawa, H.; Kida, S. J. Chem. Soc., Dalton Trans. **1988**, 641.

15 Koikawa, M.; Gotoh, M.; Okawa, H.; Kida, S.; Kohzuma, T. J. Chem. Soc., Dalton Trans. **1989**, 1613.

16 Koikawa, M.; Okawa, H.; Matsumoto, N.; Gotoh, M.; Kida, S. Kohzuma, T. J. Chem. Soc., Dalton Trans. **1989**, 2089.

17 Koikawa, M.; Okawa, H.; Maeda, Y.; Kida, S. Inorg. Chim. Acta **1992**, 194, 75.

18 Anson, F. C.; Christie, J. A.; Collins,T. J.; Coots, R. J.;

Furutani, T. T.; Gipson, S. L.; Keech, J. T.; Krafft, T. E.; Santarsiero, B. D.; Spies, G. H. J. Am. Chem. Soc. 1984, 106, 4460.

19 Anson, F. C.; Collins, T. J.; Coots, R. J.; Gipson, S. L.; Richmond, T. G. J. Am. Chem. Soc. 1984,. 106, 5037.

20 Anson, F. C.; Collins, T. J.; Coots, R. J.; Gipson, S. L.; Krafft, T. E.; Santarsiero, B. D.; Spies, G. H. Inorg. Chem. 1987, 26, 1161.

21 Che, C. M.; Cheng, W. K.; Leung, W. H.; Mak, T. C. W. J. Chem. Soc., Chem. Commun. 1987, 418.

22 Rheingold, A. L.; Geib, S. J.; Strong, J. B. Acta Cryst. 1992 C48, 157.

23 Collins, T. J.; Richmond, T. G.; Santarsiero, B. D.; Treco, B. G. R. T. J. Am. Chem. Soc. 1986, 108, 2088.

24 Anson, F. C.; Collins, T. J.; Richmond, T. G.; Santarsiero, B. D.; Toth, J. E.; Treco, B. G. R. T. J. Am. Chem. Soc. 1987, 109, 2974.

25 Brewer, J. C.; Collins, T. J.; Smith, M. R.; Santarsiero, B. D. J. Am. Chem. Soc. 1988, 110, 423.

26 Collins, T. J.; Gordon-Wylie, S. W. J. Am. Chem. Soc. 1989, 111, 4511.

27 Chandra, S. K.; Choudhury, S. B.; Ray, D.; Chakravorty, A. J. Chem. Soc., Chem. Commun. 1990, 474.

28 Chandra, S. K.; Chakravorty, A. Inorg. Chem. 1992, 31, 760.

29 Collins, T. J.; Slebodnick, C.; Uffelman, E. S. Inorg. Chem 1990, 29, 3433.

30 Collins, T. J.; Powell, R. D.; Slebodnick, C.; Uffelman, E. S. J. Am. Chem. Soc. 1990, 112, 899.

31 Workman, J. M.; Powell, R. D.; Procyk, A. D.; Collins, T. J.; Bocian, D. E. Inorg. Chem. 1992, 31, 1548.

32 Collins, T. J.; Powell, R. D.; Slebodnick, C.; Uffelman, E. S. J. Am. Chem. Soc. 1991, 113, 8419.

33 Collins, T. J.; Uffelman, E. S. Angew. Chem. Int. Ed. Engl. 1989, 28, 1509.

34 Collins, T. J.; Kastka, K. L.; Mnck, E.; Uffelman, E. S. J. Am. Chem. Soc. 1990, 112, 5637.

35 Rybca, J. S.; Margerum, D. W. Inorg. Chem. 1980, 19, 2784.

36 Rybca, J. S.; Margerum, D. W. Inorg. Chem. 1981, 20, 1453.

37 Yamasaki, K.; Sekizaki, M. Bull. Chem. Soc. Jpn. 1965, 38, 2206.

38 Takano, T.; Sasada, Y.; Kakudo, M. Acta. Cryst. 1966, 21, 514.

39 Masuko, A.; Nomuta, T.; Saito, Y. Bull. Chem. Soc. Jpn. 1967, 40, 511 .

40 Nawata, Y.; Iwasaki H.; Saito, Y. Bull. Chem. Soc. Jpn. 1967, 40, 515.

41 Nonoyama, M.; Yamasaki, K. Inorg. Chim. Acta 1969, 3, 585.

42 Nonoyama, M.; Yamasaki, K. Inorg. Chim. Acta 1971, 5, 124.

43 Nonoyama, M.; Yamasaki, K. Inorg. Chim. Acta 1973, 7, 373.

44 Nonoyama, M.; Yamasaki, K. Inorg. Chim. Acta 1973, 7, 676.

45 Kaden, T.; Zuberbhler, A. Helv. Chim. Acta 1971, 54, 1361.

46 Inoue, M.; Ojima, H.; Yamada, K.; Kubo, M.; Bull. Chem. Soc. Jpn. 1970, 43, 1592 .

47 Brown, S. J.; Tao, X.; Stephan, D. W.; Mascharak, P. K. Inorg. Chem. 1986, 25, 3377.

48 Tao, X.; Stephan, D. W.; Mascharak, P. K. Inorg. Chem. 1987, 26, 754.

49 Delany, K.; Arora, S. K.; Mascharak, P. K. Inorg. Chem. 1988, 27, 705.

50 Kabanos, T. A.; Keramidas, A. D.; Mentzafos, D.; Terzis, A. J. Chem. Soc., Chem. Commun. 1990, 1664.

51 Hanson, G. R.; Kabanos, T. A.; Keramidas, A. D.; Mentzafos, D.; Terzis, A. Inorg. Chem. 1992, 31, 2587.

52 Barnes, D. J.; Chapman, R. L.; Vagg, R. S.; Watton, E. C. J. Chem. Eng. Data 1978 , 23, 349.

53 Chapman, R. L.; Vagg, R. S. Inorg. Chim. Acta 1979, 33, 227.

54 Barnes, D. J.; Chapman, R. L.; Stephens, F. S.; Vagg, R. S. Inorg. Chim. Acta 1981, 51, 155.

55 Stephens, F. S.; Vagg, R. S. Inorg. Chim. Acta 1986, 120, 165.

56 Chapman, R. L.; Stephens, F. S.; Vagg, R. S. Inorg. Chim. Acta 1980, 43, 29.

57 Che, C. M.; Cheng, W. K.; Mak, T. C. W. J. Chem. Soc.,Chem. Commun. 1986, 200.

58 Che, C. M.; Cheng, W. K. J. Chem. Soc., Chem. Commun. 1986, 1443.

59 Che, C. M.; Ma, J. X.; Wong, W. T.; Lai T. F.; Poon, C. K. Inorg. Chem. 1988 , 27, 2547.

60 Mak, S. T.; Yam, V. W. W.; Che, C. M.; Mak, T. C. W. J. Chem. Soc., Dalton Trans. 1990, 2555.

61 Leung, W. H.; Ma, J. X. ; Yam, V. W. W. ; Che, C. M.; Poon, C. K. J. Chem. Soc., Dalton Trans. 1991,1071.

62 Mak, S. T.; Wong, W. T.; Yam, V. W. W.; Lai, T. F.; Che, C.

M. J. Chem. Soc., Dalton Trans. **1991**, 1915 .

63 Cheng, W. K.; Wong, K. Y.; Tong, W. F.; Lai, T. F. ; Che, C. M. J. Chem. Soc., Dalton Trans. **1992** , 91.

64 Lomis, T. J.; Martin, J.; Mccloskey, B.; Zhang, S.; Siddiqui, S.; Shepherd, R. E.; Siuda, J. F. Inorg. Chim. Acta **1989**, 157, 99.

65 Brown, S. J.; Mascharac, P. K. J. Am. Chem. Soc. **1988**, 110, 1996.

66 Brown, S. J.; Hudson, S. E.; Stephan, D. W.; Mascharak, P. K. Inorg. Chem. **1989**, 28, 468 and references therein.

67 Otsuka, M.; Yoshida, M.; Kobayashi, S.; Ohno, M. J. Am. Chem. Soc. **1981**, 103, 6986.

68 Henichart, J. P.; Houssin, R.; Bernier, J. L.; Catteau, J. P. J. Chem. Soc., Chem. Commun. **1982**, 1295.

69 Lomis, T. J.; Siuda, J. F.; Shepherd, R. E. J. Chem. Soc., Chem. Commun. **1988**, 290.

70 Lomis, T. J.; Elliott, M. G.; Siddiqui, S.; Mayer, M.; Koepsel, R. R. Inorg. Chem. **1989**, 28, 2369.

71 Motekitis, R. J.; Martell, A. E. J. Am. Chem. Soc. **1970**, 92, 4223.

72 Motekitis, R. J.; Martell, A. E. J. Am. Chem. Soc. **1982**, 104, 3782.

73 Smith, R. M.; Motekitis, R. J.; Martell, A. E. Inorg. Chem. **1985**, 24, 1132.

74 Dunford, H. B.; Stillman, J. S. Coord. Chem. Rev. **1976**, 19, 187.

75 Hewson, W. D.; Hager, L. D. Porphyrins **1979**, 7, 295.

76 Dolphin, D.; James, B. R. In `Inorganic Chemistry: Toward the 21st Century´, Chisholm, M. H. ,Ed.; ACS Symposium Series No. 211 ; American Chemical Society: Washington, D.C., **1983**, p. 99.

77 Dawson, J. H.; Sono, M. Chem. Rev. **1987**, 87, 1255.

78 Dawson, J. H. Science **1988**, 240, 433.

79 Griffin, B. W.; Peterson, J. A.; Estabrook, R. W. Porphyrins **1979**, 7, 333.

80 Alexander, L. S.; Goff, H. M. J. Chem. Educ. **1982**, 59, 179.

81 Guengerich, F. P.; Macdonald, T. L. Acc. Chem. Res. **1984**, 17, 9.

82 Mansuy, D. Pure Appl. Chem. **1987**, 59, 759.

83 Witt, S. N. ; Blair, D. F.; Chan, S. I. J. Biol. Chem. **1986**, 261, 8104.

84 Palmer, G. Pure Appl. Chem. **1987**, 59, 749.

85 Ostovic´, D.; Knobler, C. B.; Bruice, T. C. J. Am. Chem. Soc. **1987**, 109, 3444.

86 Okamoto, T.; Sasaki, K.; Oka, S. J. Am. Chem. Soc. **1988**, 110, 1187.

87 Sugimoto, H.; Tung, H. -C.; Sawyer, D. T. J. Am. Chem. Soc. **1988**, 110, 2465.

88 Gold, A.; Jayaraj, K.; Doppelt, P.; Weiss, R.; Chottard, G.; Bill, E.; Ding, X.; Trantwein, A. X. J. Am. Chem. Soc. **1988**, 110, 5756.

89 Groves, G. T.; Watanabe, Y. J. Am. Chem. Soc. **1988**, 110, 8443.

90 Arasingham, R. D.; Cornman, C. R.; Balch, A. L. J. Am. Chem. Soc. **1989**, 111, 7800.

91 Traylor, T. G.; Fann, W. -P.; Bandyopadhyay, D. J. Am. Chem.

Soc. **1989**, 111, 8009.

92 Groves, J. T.; Kruper, W. J., Jr. J. Am. Chem. Soc. **1979**, 101, 7613.

93 Yuan, L. C.; Bruice, T. C. J. Am. Chem. Soc. **1985**, 107, 512.

94 Yuan, L. C.; Bruice, T. C. J. Am. Chem. Soc. **1985**, 107, 8273.

95 Creager, S. E.; Murray, R. W. Inorg. Chem. **1985**, 24, 3824.

96 De Carvalho, M. E.; Meunier, B. Nouv. J. Chim. **1986**, 10, 223.

97 Razenberg, J. A. S. J.; Nolte, R. J. M.; Drenth, W. J. Chem. Soc., Chem. Commun. **1986**, 277.

98 Wong, W. -H.; Ostovic´, D.; Bruice, T. C. J. Am. Chem. Soc. **1987**, 109, 3428.

99 Rodgers, K. R.; Goff, H. M. J. Am. Chem. Soc. **1988**, 110, 7049.

100 Nappa, M. J.; McKinney, R. J. Inorg. Chem. **1988**, 27, 3740.

101 Groves, J. T.; Stern, M. K.; J. Am. Chem. Soc. **1988**, 110, 8628.

102 Holm, R. H. Chem. Rev. **1987**, 87, 1401.

103 Bryan, P. S.; Dabrowiak, J. C. Inorg. Chem. **1975**, 14, 296.

104 Bryan, P. S.; Dabrowiak, J. C. Inorg. Chem. **1975**, 14, 299.

105 Chan, P. K.; Poon, C. K. J. Chem. Soc., Dalton Trans. **1976**, 858.

106 Neves, D. R.; Dabrowiak, J. C. Inorg. Chem. **1976**, 15, 129.

107 Bryan, P. S.; Calvert, J. M. Inorg. Nucl. Chem. Lett. **1977**, 13, 615.

108 Herron, N.; Busch, D. H. Inorg. Chem. **1983**, 22, 3470.

109 Furniss, B. S.; Hannaford, A. J.; Rogers, V.; Smith, P. W. G.; Tatchell, A. R. " Vogel´s Textbook of Practical Organic

Chemistry" 4th edition, Longman: Beccles and London, **1978**, p. 289.

110 Bush, J. B., Jr.; Finkbeiner, H. J. Am. Chem. Soc. **1968**, 90, 5903.

111 Evans, D. F. J. Chem. Soc. **1959**, 2003.

112 van Geet, A. L. Anal. Chem. **1968**, 40, 2227.

113 Gerger, W.; Mayer, U.; Gutmann, V. Monatsh. Chem. **1977**, 108 417.

114 O'Connor, C. J. Prog. Inorg. Chem. **1982**, 29, 203.

115 Weiner, M. A.; Basu, A. Inorg. Chem. **1980**, 19, 2797.

116 Kelly, S. L.; Kadish, K. M. ibid. **1984**, 23, 679.

117 Augustinsson. K. B.; Hasselquist, H. Acta Chem Scand **1961**, 15, 817.

118 Boekelheide, V.; Linn, W. J. J Am Chem Soc **1954**, 76, 1286.

119 Takahashi, K,; Takeda, K.; Mitsuhashi, K. J Heterocyclic Chem **1978**, 15, 893.

120 Case, F. H.; Kasper, T. J. J Am Chem Soc **1956**, 78, 5842.

121 Feely, W. E.; Beavers, E. M. J Am Chem Soc **1959**,81, 4004.

122 Nakamoto, K. `Infrared Spectra of Inorganic and Co-ordination Compounds,' 2nd edition, WIley; New York, **1970**, p.187.

123 Geary, W. J. Coord. Chem. Rev. **1971**, 7, 81.

124 van den Bergen, A.; Murray, K. S.; O'Connor, M. J.; West, B. O. Aust. J. Chem. **1969**, 22, 39.

125 Boucher, L. J.; Coe, C. G. Inorg. Chem. **1976**, 15, 1334.

126 Boucher, L. J.; Day, V. W. Inorg. Chem. **1977**, 16, 1360.

127 Day, V. W.; Ray Stults, B.; Tasset, E. L.; Marianelli, R. S.; Boucher, L. J. Inorg. Nucl. Chem. Lett. **1975**, 11, 505.

128 LaMar, G. N. in `NMR of Paramagnetic Molecules´, Eds., Lamar, G. N., Horroks, W. Dew. Jr., Holm, R. H., Academic Press: New York , **1973**, p. 85-126.

129 Bertini, J.; Luchinat, C.; Messori, L. in `Metal Ions in Biological Systems. Applications of NMR to Paramagnetic Species´, Vol. 21, ed., Sigel, H. Marcel Decker: New York and Basel, **1987**; p. 47-86.

130 Que, L., Jr.; Maroney, M. J. in `Metal Ions in Biological Systems. Applications of NMR to Paramagnetic_Species´, Vol. 21, ed., Sigel, H. Marcel Decker: New York and Basel, **1984**; p. 87-120.

131 Horrocks, W. DeW, Jr. in `NMR of Paramagnetic Molecules´, Eds., La Mar, G. N., Horrocks, W. DeW, Jr., Holm, R. H. Academic Press: New York, **1973**; pp 127-177.

132 Eaton, D. R.; McClellan, W. R.; Weiher, J. F. Inorg. Chem. **1968**, 7, 2040.

133 McElroy, F. C.; Dabrowiak, J. C.; Macero, D. J. Inorg. Chem. **1977**, 16, 947.

134 Boggess, R. K.; Hughes, J. W.; Coleman, W. M.; Taylor, L. T. Inorg. Chim. Acta, **1980**, 38, 183.

135 Coleman, W. M.; Boggess, R. K.; Hughes, J. W.; Taylor, L. T. Inorg. Chem. **1981**, 20, 700

136 Coleman, W. M.; Boggess, R. K.; Hughes, J. W.; Taylor, L. T. Inorg. Chem. **1981**, 20, 1253.

137 Boucher, L. J.; Garber, H. K. Inorg. Chem. **1970**, 9, 2644.

138 Scheidt, W. R.; Reed, C. A. Chem. Rev. **1981**, 81, 543.

139 Albertini, J. P.; Garnier-Suillerot, A. Biochem. **1984**, 23, 47.

140 Hecht, S. M. Acc. Chem. Res. **1989**, 19, 383.

141 Holm, R. H.; Ibers, J. A. Science, **1980**, 209, 223.

142 Goedken, V. L.; Merrell, P. H.; Busch, D. H. J. Am. Chem. Soc. **1972**, 94, 3397.

143 Riley, D. P.; Merrell, P. H.; Stone, J. A.; Busch, D. H. Inorg. Chem. **1975**, 14, 490.

144 Dabrowiak, J. C.; Busch, D. H. Inorg. Chem. **1975**, 14, 1881.

145 Reichgott, D. W.; Rose, N. J. J. Am. Chem. Soc. **1977**, 99, 1813.

146 Maroney, M. J.; Fey, E. O.; Baldwin, D. A.; Stenkamp, R. E.; Jensen, L. H.; Rose, N. J. Inorg. Chem. **1986**, 25, 1409.

147 Stynes, D. V.; Noglik, H.; Thompson, D. W. Inorg. Chem. **1991**, 30, 4567.

148 Koch, S.; Holm, R. H.; Frankel, R. B. J. Am. Chem. Soc. **1975**, 97, 6714.

149 Nishida, Y.; Oshio,S.; Kida, S.; Maeda, Y. Inorg. Chim. Acta **1978**, 26, 207.

150 Nishida, Y.; Sumita, A.; Hayashida, K.; Ohshima, H.; Kida, S.; Maeda, Y. J. Coord. Chem. **1979**, 9, 161.

151 Sawyer, D. T.; Roberts, J. L., Jr. ` Experimental Electrochemistry for Chemists, Wiley: New York, **1974**.

152 Sugimoto, H.; Sawyer, D. T. J. Am. Chem. Soc. **1985**, 107, 5712.

153 Cromer, D. T.; Waber, J. T. `International Tables for X-ray Crystallography´; Kynoch: Birmingham, England, Table 2.2 B, **1974**; Vol.IV.

154 Ibers, J. A.; Hamilton, W. C. Acta Crystallogr. **1964**, 17,

781.

155 Reference 153, Table 2.3.1, **1974**; Vol.IV.

156 Gilmore, C. J. MITHRIL- An Integrated Direct Methods Computer Program; J. Appl. Cryst. **1984**, 17, 42; University of Glasgow, Scotland.

157 Beurskens, P. T. DIRDIF - Direct Methods for Difference Structures - An Automatic Procedure Phase Extention and Refinement of Difference Structure Factors; Technical Report 1984/1 Crystallography Laboratory, Toernooiveld, 6255 Ed, Nijmegen, Netherlands.

158 Frenz, B. A. `The Enraf-Nonius CAD-4 SDP - A real-time System for Concurent X-Ray Data Collection and Crystal Structure Determination,´ in Computing in Crystallography, Eds., Schenk, H.; Olthof-Hazelkamp, R.; van Konigsveld, H.; Bassi, G. C., Delft University Press, Delft: Holland, **1978**, pp 64-71.

159 Motherwell, S.; Clegg, W. PLUTO. Program for Plotting Molecular and Crystal Structures, University of Cambridge, England, 1978.

160 Johnson, C. K. ORTEP II. Report ONRL-5138. Oak Ridge National Laboratory, Oak Ridge, Tennessee, 1976.

161 Yang, Y; Diederich, F.; Valentine, J. S. J. Am. Chem. Soc. **1991**, 113, 7195.

162 Cotton, S. A. Coord. Chem. Rev. **1972**, 8, 185.

163 Earnshaw, A. in `Introduction to Magnetochemistry´, Academic Press: London, **1968**, p. 35.

164 Figgis, B. N.; Lewis, J. Prog. in Inorg. Chem. **1964**, 6, 37.

165 Martin, L. L.; Martin, R. L.; Muray, K. S.; Sargeson, A. M. Inorg. Chem., **1990**, 29, 1387.

166 (a) Erickson, N. E. in `The Mssbauer Effect and Its Application in Chemistry ´, Advances in Chemistry Series, Vol. 68, Series Ed. Gould, R. F., American Chemical Society; Washington, D. C., **1967**, p. 86-104. (b) Ebsworth, E. A. V.; Rankin, D. W. H.; Cradock, S. in `Structural Methods in Inorganic Chemistry´, Blackwell Scientific Publications, Osney Mead: Oxford, **1987**, p. 280-303.

167 Tang, S. C.; Koch, S.; Papaefthymiou, G. C.; foner, S.; Frankel, R. B.; Ibers, J. A.; Holm, R. H. J. Am. Chem. Soc. **1976**, 98, 2414.

168 Hseu, J. F.; Chen, J. J.; Chuang, C. C.; Wei, H. H.; Cheng, M. C.; Wang, Y.; Yao, Y. D. Inorg. Chim. Acta **1991**, 184, 1.

169 Lind, M. D.; Hoard, J. L. Inorg. Chem. **1964**, 3, 34.

170 Bohan, T. L. J. Magn. Resonance **1977**, 109.

171 Bhattacharya, S.; Chakravorty, A. Proc. Indian Acad. Sci. **1985**, 95, 159.

172 Basu, P.; Bhanja Choudhury, S.; Pal, S.; Chakravorty, A. Inorg. Chem., **1989**, 28, 2680.

173 Stynes, D. V.; Noglic, H.; Thompson, D. W. Inorg. Chem. **1991**, 30, 4567.

174 Kennedy, B. J.; Murray, K. S.; Zwack, P. R.; Homborg, H.; Kalz, W. Inorg. Chem., **1986**, 25, 2539.

175 Cotton, F. A.; Wilkinson, G. in `Advanced Inorganic Chemistry´ , 3rd Edition, Wiley Eastern Limited: New Delhi, p. 721-722.

176 Sadasivan, N.; Kernohan, J. A.; Endicott, J. F. Inorg. Chem. **1967**, 6, 770.

177 Rakowski, M. C.; Rycheck, M.; Busch, D. H. Inorg. Chem. 1975, 14, 1194.

178 Vlcek, A.A. Inorg. Chem. 1967, 6, 1425.

179 Wentworth, R. A. D.; Piper, T. S. Inorg. Chem. 1965, 4,709.

180 Tait, A. M.; Busch, D. H. Inorg. Chem. 1976, 15,197.

181 Tait, A. M.; Lovecchio, F. V.; Busch, D. H. Inorg. Chem. 1977, 16, 2206.

182 Hung, Y.; Martin, L. Y.; Jackels, S. C.; Tait, A. M.; Busch, D. H. J. Am. Chem. Soc. 1977, 99, 4029.

183 Gosta, G.; Puxeddu, A.; Tauzher, G. Inorg. Nucl. Chem. Lett. 1968, 4, 319.

184 Costa, G.; Mestroni, G.; Puxeddu, A.; Reisenhofer, E. J. Chem. Soc.(A) 1970, 2870.

185 Hohokabe, Y.; Yamezaki, N. Bull. Chem. Soc. Jpn. 1971, 44, 1563.

186 Balasubramanian, P. N.; Vijayaraghavan, V. R. Inorg. Chim. Acta. 1980, 42, 179.

187 Truxillo, L. A.; Davis, D. G. Anal. Chem. 1975, 47, 2870.

188 Walder, L.; Rytz, G.; Vogeli, U.; Scheffold, R.; Engel, P. Helv. Chim. Acta. 1984, 67, 1801.

189 Muller, E.; Bernardinelli, G.; von Zelewsky, A. Inorg. Chem. 1988, 27, 4645.

190 Finke, R. G.; Smith, B. L.; Droege, M. W.; Elliott, C. M.; Hershenhart, E. J. Organomet. Chem. 1980, 202, C25.

191 Elliott, C. M.; Hershenhart, E.; Finke, R. G.; Smith, B. L. J. Am. Chem. Soc. 1981, 103, 5558.

192 Averill, D. F.; Broman, R. F. Inorg. Chem. 1978, 17, 3389.

193 Koikawa, M.; Gotoh, M.; Okawa, H.; Kida, S. J. Chem. Soc.,

Dalton Trans. 1989, 1613.

194 Mahapatra, S.; Bhuniya, D.; Mukherjee, R. N. Polyhedron, 1992, 11, 2045.

195 Mukherjee, R. N.; Rajan, O. A.; Chakravorty, A. Inorg. Chem. 1982, 21, 785.

196 Bhattacharya, S.; Mukherjee, R. N.; Chakravorty, A. Inorg. Chem. 1986, 25, 3448.

197 Rillema, D. P.; Endicott, J. F.; Papaconstantinou, E. Inorg. Chem. 1971,10, 1739.

198 Schrauzer, G. N.; Windgassem, R. J. J. Am. Chem. Soc. 1966, 88, 3738.

199 Halpern, J.; Chan, M. S.; Hanson, J.; Roche, T. S.; Topich, J. A. J. Am. Chem. Soc. 1975, 97 , 1606.

200 Volpin, M. E.; Levitin, I. Y.; Sigan, A. L.; Nikitaev, A. T. J. Organomet. Chem. 1985, 279, 263.

201 Kitajima, N.; Fujisawa, K.; Moro-oka, Y. J. Am. Chem. Soc. 3210.

202 Knapp, S.; Keenan, T. P.; Zhang, X.; Fifar, R.; Potenza, J. A.; Schugar, H. J. J. Am. Chem. Soc. 1990, 112, 3452 and references therein.

203 Holm , R. H.; O'Connor, M. J. Prog. Inorg. Chem. 1971 , 14, 241.

204 Sugiura Y.; Takita, T.; Umezawa, H. in `Metal Ions in Biological Systems', Sigel, H. ,Ed., Marcel Dekker, Inc.: New York and Basel, 1985, Vol. 19, pp 81-108.

205 Miyoshi, K.; Tanaka, H.; Kimura, E.; Tsuboyama, S.; Murata, S.; Shimizu, H. ; Ishizu, K. Inorg. Chim. Acta 1983, 78, 23.

206 Ammeter, J. H.; Burgi, H. -B.; Thibeault, J. C.; Hoffmann, R. J. Am. Chem. Soc. 1978, 100, 3686.

207 Hay, P. J.; Thibeault, J. C.; Hoffmann, R. ibid. 1975, 97, 4884.

208 Huntress, E. H.; Walter, H. C. J. Am. Chem. Soc. 1948, 70, 3702.

209 Murakami, Y.; Matsuda, Y.; Sakata, K. Inorg. Chem. 1971, 10, 1728.

210 Sugiura, Y. Inorg. Chem. 1978, 17, 2176.

211 Yokoi, H.; Addition, A. W. Inorg. Chem. 1977, 16, 1341.

212 Gouge, E. M.; Geldard, J. F. Arch. Biochem. Biophys. 1978, 17, 270.

213 Sakaguchi, U.; Addison, A. W. J. Chem. Soc. Dalton Trans. 1979, 600.

214 Samasundaram, I.; Kommiya, M. K.; Palaniandavar, M. J. Chem. Soc.,Dalton Trans. 1991, 2083.

215 Garber, T.; Wallendael, S. V.; Rillema, D. P.; Kirk, M.; Hatfield, W. E.; Welch, J. H.; Singh, P. Inorg. Chem. 1990, 29, 2863.

216 Elias, H.; Hilms, E.; Wannowius, B.; Paulus, H. Inorg. Chim. Acta 1990, 178, 93.

217 Martin, E. M.; Bereman, R. D. Inorg. Chim. Acta 1991, 188, 233.

218 Harris, C. M.; Patil, H. R. H.; Sinn, E. Inorg. Chem. 1967, 6, 1102.

219 Herring, F. G. ; Patmore, D. J.; Storr, A. J. Chem. Soc., Dalton Trans. 1975 , 711.

220 Kivelson, D. ; Neiman, R. J. Chem. Phys. **1961**, 35, 149.

221 Ray, R. K.; Kauffman, G. B. ibid. **1990**, 174, 257 and references therein.

222 Gupta, N.; Mukherjee, S.; Mahapatra, S.; Ray, M.; Mukherjee, R. N. Inorg. Chem. **1992**, 31, 139.

223 Nicholson, R. S.; Shain, I. Anal Chem. **1964**, 36, 706.

224 Karlinm K. D.; Haka, M. S.; Cruse, R. W.; Meyer, G. J.; Farooq, A.; Gultneh, Y.; Hayes, J. C.; Zubieta, J. J. Am. Chem. Soc., **1988**, 110, 1196.

225 Patterson, G. S.; Holm, R. H. Bioinorg. Chem. **1975**, 4, 257.

226 Addition, A. W. Inorg. Chim. Acta **1989**, 162, 217.

227 Cinquantini, A.; Opromolla, G.; Zanello, P. J. Chem. Soc., Dalton Trans. **1991**, 3161 and references therein.

228 Gritzner, G. J. Phys. Chem. **1986**, 90, 5478.

229 Bottomley, L. A.; Kadish, K. M. Inorg. Chem. **1981**, 20, 1348.

230 Shriver, D. F.; Atkins, P. W.; Langford, C. H. in `Inorganic Chemistry´,; Oxford University Press: Oxford, **1990**, pp 153-154.

231 Lohr, L. L., Jr. ; Lipscomb, W. N. Inorg. Chem. **1963**, 2, 911.

232 Gouteron, J.; Jeannin, S.; Jeannin, Y.; Livage, J.; Sanchez, C. Inorg. Chem. **1984**, 23, 3387.

FUTURE SCOPE OF THE WORK

In this thesis work we have developed an extensive metal-amide chemistry with a series of novel N_4 non-porphyrin bis-amide ligands. The effect of axial ligands on the redox properties, spin-state behavior, and absorption spectral properties in a selected group of metal-amide complexes have been studied using various spectroscopic and electrochemical techniques. The effect of stereochemical dispositions of the ligands around copper(II) centers using bidentate amide ligands has also been investigated.

This is for the first time that an iron chemistry with a open-chain N_4 ligand system has been developed where, spin-state of the metal center can be manipulated solely via axial ligands similar to porphyrins and phthalocyanins. To understand the structure and bonding in different spin states, crystal structures of a sizable number of iron(III) complexes and detail studies in the solution phase would be of paramount importance. There is a possibility that suitable axial ligands might give rise to other spin states. Our future endeavor are set along these directions.

In this work we have learned the non-innocent character of the present ligand system on the redox properties of the complexes. As a result of which we were unable to isolate any complex with metal in the higher (> 3) oxidation state. Our future plan is to modify the present ligand system to prevent ligand oxidation.

LIST OF PUBLICATIONS

1. M.Ray, S. Mukerjee, and R. N. Mukherjee,

   Manganese(III) Complexes of 1,2-Bis(2-pyridinecarboxamido) benzene: Synthesis, Spectra, and Electrochemistry,
   J. Chem. Soc., Dalton Trans., 1990, 3635.

*2 N. Gupta, S. Mukerjee, S. Mahapatra, M. Ray, R. N. Mukherjee,

   Triply Bridged Diruthenium Complexes with $[Ru^{III}_2(\mu\text{-}O)(\mu\text{-}O_2CCH_3)_2]^{3+}$ and $[Ru^{IV}Ru^{III}(\mu\text{-}O)(\mu\text{-}O_2CCH_3)_2]^{3+}$ Cores: Synthesis, Spectra, and Electrochemistry,
   Inorg. Chem., 1992, 31, 139.

3 M. Ray and R. N. Mukherjee,

   Cobalt(III) Complexes Using In-plane Tetradentate Pyridine-carboxamide Ligands and Two Monodentate Axial Ligands: Spectroelectrochemical Correlation,
   Polyhedron, 1992, 11, 0000.

4 M. Ray and R. N. Mukherjee

   Spin-State Regulation of Iron(III) Centre by Axial Ligands with Tetradentate Bis(picolinamide) In-plane Ligands,
   Manuscript submitted for publication.

5 M. Ray and R. N. Mukherjee

   Stereochemical Changes of Effectively $Cu^{II}N_4$ Unit by Chemical Modification of Pyridine Amide Ligands: Absorption and EPR Spectra and Electrochemistry,
   Manuscript submitted for publication.

Several other manuscripts are under preparation.

---

* Content of this paper is not related to this thesis.

APPENDIX

Table I: Table of Bond Distances in Angstroms

Atom 1	Atom 2	Distance	Atom 1	Atom 2	Distance
Fe	O3	1.965(2)	N5	C23	1.518(6)
Fe	O5	1.979(2)	N5	C25	1.520(5)
Fe	N1	2.061(2)	N5	C27	1.515(6)
Fe	N2	2.067(2)	N5	C29	1.521(6)
Fe	N3	2.205(2)	C1	C2	1.384(4)
Fe	N4	2.199(3)	C1	C6	1.417(4)
CL1	C4	1.739(3)	C2	C3	1.391(5)
CL2	C3	1.736(3)	C3	C4	1.370(5)
CL3	C31	1.741(6)	C4	C5	1.389(5)
CL4	C31	1.722(5)	C5	C6	1.392(4)
CL5	C31	1.731(5)	C7	C8	1.505(4)
O1	C7	1.230(4)	C8	C12	1.384(4)
O2	C13	1.228(4)	C9	C10	1.379(4)
O3	C19	1.284(4)	C10	C11	1.369(6)
O4	C19	1.218(4)	C11	C12	1.384(5)
O5	C21	1.282(5)	C13	C14	1.505(5)
O6	C21	1.222(5)	C14	C18	1.380(5)
N1	C1	1.399(4)	C15	C16	1.382(5)
N1	C7	1.341(4)	C16	C17	1.371(6)
N2	C6	1.395(4)	C17	C18	1.382(6)
N2	C13	1.341(4)	C19	C20	1.502(6)
N3	C8	1.339(4)	C21	C22	1.505(4)
N3	C9	1.342(5)	C23	C24	1.501(9)
N4	C14	1.342(4)	C25	C26	1.512(7)
N4	C15	1.339(4)	C27	C28	1.520(8)
C29	C30	1.504(7)			

Numbers in parentheses are estimated standard deviations in the least significant digits.

Table II: Table of Bond Angles in Degrees

Atom 1	Atom 2	Atom 3	Angle	Atom 1	Atom 2	Atom 3	Angle
O3	Fe	O5	166.28(9)	C8	N3	C9	118.4(2)
O3	Fe	N1	94.63(9)	Fe	N4	C14	113.4(3)
O3	Fe	N2	95.85(9)	Fe	N4	C15	128.1(2)
O3	Fe	N3	84.99(8)	C14	N4	C15	118.5(3)
O3	Fe	N4	86.53(9)	C23	N5	C25	111.6(3)
O5	Fe	N1	96.03(9)	C23	N5	C27	110.7(3)
O5	Fe	N2	94.91(9)	C23	N5	C29	106.3(3)
O5	Fe	N3	89.33(9)	C25	N5	C27	105.9(3)
O5	Fe	N4	87.82(9)	C25	N5	C29	110.9(3)
N1	Fe	N2	77.20(9)	C27	N5	C29	111.8(4)
N1	Fe	N3	75.60(9)	N1	C1	C2	125.6(3)
N1	Fe	N4	153.26(9)	N1	C1	C6	114.4(3)
N2	Fe	N3	152.8(1)	C2	C1	C6	120.0(3)
N2	Fe	N4	76.12(9)	C1	C2	C3	120.2(3)
N3	Fe	N4	131.02(9)	CL2	C3	C2	117.5(2)
Fe	O3	C19	126.0(3)	CL2	C3	C4	122.5(3)
Fe	O5	C21	122.6(2)	C2	C3	C4	120.1(3)
Fe	N1	C1	116.9(2)	Cl1	C4	C3	121.6(3)
Fe	N1	C7	120.5(2)	Cl1	C4	C5	117.4(2)
C1	N1	C7	122.1(3)	C3	C4	C5	121.1(3)
Fe	N2	C6	116.7(2)	C4	C5	C6	120.0(3)
Fe	N2	C13	120.4(3)	N2	C6	C1	114.6(2)
C6	N2	C13	122.8(2)	N2	C6	C5	126.5(3)
Fe	N3	C8	113.3(2)	C1	C6	C5	118.9(3)
Fe	N3	C9	128.0(3)	O1	C7	N1	128.5(3)

Table II: Bond Angles (cont.)

Atom 1	Atom 2	Atom 3	Angle	Atom 1	Atom 2	Atom 3	Angle
O1	C7	C8	119.1(3)	C15	C16	C17	119.5(3)
N1	C7	C8	112.4(3)	C16	C17	C18	119.1(4)
N3	C8	C7	116.6(2)	C14	C18	C17	118.6(3)
N3	C8	C12	122.8(3)	O3	C19	O4	124.5(3)
C7	C8	C12	120.6(3)	O3	C19	C20	114.7(3)
N3	C9	C10	121.8(4)	O4	C19	C20	120.8(3)
C9	C10	C11	119.6(3)	O5	C21	O6	123.2(3)
C10	C11	C12	119.3(3)	O5	C21	C22	115.9(3)
C8	C12	C11	118.1(3)	O6	C21	C22	120.9(3)
O2	C13	N2	128.3(3)	N5	C23	C24	114.8(4)
O2	C13	C14	119.1(3)	N5	C25	C26	114.5(3)
N2	C13	C14	112.6(3)	N5	C27	C28	114.0(4)
N4	C14	C13	117.0(3)	N5	C29	C30	115.5(3)
N4	C14	C18	122.5(3)	CL3	C31	CL4	110.9(3)
C13	C14	C18	120.5(3)	CL3	C31	CL5	110.3(2)
N4	C15	C16	121.9(3)	CL4	C31	CL5	111.4(3)

Numbers in parentheses are estimated standard deviations in the least significant digits.

Table III:

Table of Positional Parameters and Their Estimated Standard Deviations

Atom	x	y	z	B(A2)
Fe	0.72431(3)	0.21540(2)	0.53862(2)	2.738(7)
Cl1	1.16861(7)	0.41624(5)	0.46233(6)	5.52(2)
CL2	1.25041(7)	0.25537(6)	0.44831(7)	5.78(2)
CL3	0.4277(2)	0.02299(9)	0.7134(1)	11.34(5)
CL4	0.4180(2)	0.1175(1)	0.84748(9)	13.99(6)
CL5	0.3144(2)	0.1551(1)	0.6828(1)	12.84(6)
O1	0.9563(2)	0.0834(1)	0.4597(2)	5.14(5)
O2	0.7784(2)	0.4298(1)	0.4950(2)	5.59(6)
O3	0.6359(2)	0.2062(1)	0.4261(1)	3.66(4)
O4	0.4785(2)	0.1683(1)	0.4579(2)	5.18(6)
O5	0.7807(2)	0.2161(1)	0.6597(1)	3.98(5)
O6	0.6265(2)	0.1748(1)	0.6918(2)	5.52(6)
N1	0.8693(2)	0.1801(1)	0.5067(1)	2.91(5)
N2	0.8022(2)	0.3089(1)	0.5167(1)	2.90(5)
N3	0.7125(2)	0.0986(1)	0.5427(1)	3.08(5)
N4	0.6062(2)	0.2986(1)	0.5582(1)	3.35(5)
N5	1.0312(3)	0.0557(2)	0.2387(2)	5.78(8)
C1	0.9456(2)	0.2320(2)	0.4934(2)	2.99(6)
C2	1.0511(2)	0.2191(2)	0.4787(2)	3.59(6)
C3	1.1197(3)	0.2756(2)	0.4675(2)	3.93(7)
C4	1.0834(3)	0.3441(2)	0.4715(2)	3.77(6)
C5	0.9779(3)	0.3585(2)	0.4862(2)	3.50(6)
C6	0.9081(2)	0.3028(2)	0.4982(2)	2.90(6)
C7	0.8821(2)	0.1113(2)	0.4892(2)	3.22(6)

Table of Positional Parameters and Their Estimated Standard Deviations (cont.

Atom	x	y	z	B(A2)
C8	0.7911(2)	0.0655(2)	0.5106(2)	3.05(6)
C9	0.6322(3)	0.0592(2)	0.5653(2)	3.76(7)
C10	0.6293(3)	-0.0137(2)	0.5568(2)	4.13(7)
C11	0.7087(3)	-0.0472(2)	0.5226(2)	4.40(8)
C12	0.7922(3)	-0.0073(2)	0.4990(2)	4.01(7)
C13	0.7489(3)	0.3712(2)	0.5155(2)	3.63(7)
C14	0.6402(3)	0.3645(2)	0.5444(2)	3.51(6)
C15	0.5087(3)	0.2907(2)	0.5823(2)	4.15(7)
C16	0.4440(3)	0.3484(2)	0.5946(2)	4.87(8)
C17	0.4805(3)	0.4157(2)	0.5824(2)	5.60(9)
C18	0.5802(3)	0.4243(2)	0.5564(2)	4.92(8)
C19	0.5349(3)	0.1848(2)	0.4074(2)	3.87(7)
C20	0.4888(4)	0.1807(3)	0.3161(3)	6.9(1)
C21	0.7221(3)	0.1954(2)	0.7120(2)	3.80(7)
C22	0.7774(3)	0.1995(2)	0.8018(2)	5.62(9)
C23	0.9121(4)	0.0697(3)	0.1965(3)	7.3(1)
C24	0.8367(4)	0.0922(3)	0.2537(4)	9.8(2)
C25	1.0382(4)	-0.0014(3)	0.3048(2)	6.4(1)
C26	0.9861(5)	-0.0716(3)	0.2740(3)	9.1(2)
C27	1.0821(4)	0.1218(3)	0.2831(3)	7.4(1)
C28	1.0804(6)	0.1862(3)	0.2272(4)	11.0(2)
C29	1.0920(4)	0.0328(3)	0.1707(2)	7.2(1)
C30	1.2134(5)	0.0172(3)	0.1985(3)	9.4(2)
C31	0.4244(4)	0.1114(3)	0.7440(3)	7.0(1)

Anisotropically refined atoms are given in the form of the isotropic equivalent displacement parameter

Table IV: Table of General Displacement Parameter Expressions - U's

Name	U(1,1)	U(2,2)	U(3,3)	U(1,2)	U(1,3)	U(2,3)
Fe	0.0395(2)	0.0310(2)	0.0342(2)	-0.0038(2)	0.0087(2)	-0.0000(2)
Cl1	0.0598(5)	0.0567(5)	0.0915(6)	-0.0267(4)	0.0100(4)	0.0152(5)
CL2	0.0464(4)	0.0712(6)	0.1072(7)	-0.0149(4)	0.0283(4)	-0.0049(6)
CL3	0.205(1)	0.100(1)	0.143(1)	-0.016(1)	0.0771(9)	-0.0122(9)
CL4	0.314(2)	0.141(1)	0.1009(8)	0.000(1)	0.1023(9)	0.0012(9)
CL5	0.131(1)	0.150(1)	0.194(2)	0.002(1)	-0.003(1)	0.016(1)
O1	0.060(1)	0.043(1)	0.102(2)	-0.004(1)	0.040(1)	-0.012(1)
O2	0.073(1)	0.033(1)	0.108(2)	-0.003(1)	0.022(1)	0.009(1)
O3	0.047(1)	0.049(1)	0.041(1)	-0.010(1)	0.0021(9)	-0.001(1)
O4	0.062(1)	0.055(1)	0.084(2)	-0.013(1)	0.023(1)	0.002(1)
O5	0.063(1)	0.053(1)	0.036(1)	0.003(1)	0.0120(9)	0.002(1)
O6	0.066(1)	0.080(2)	0.066(1)	-0.006(1)	0.017(1)	-0.002(1)
N1	0.040(1)	0.030(1)	0.042(1)	-0.006(1)	0.011(1)	-0.001(1)
N2	0.041(1)	0.031(1)	0.038(1)	-0.004(1)	0.007(1)	-0.002(1)
N3	0.045(1)	0.034(1)	0.039(1)	-0.006(1)	0.009(1)	0.002(1)
N4	0.046(1)	0.041(1)	0.040(1)	0.002(1)	0.008(1)	-0.002(1)
N5	0.089(2)	0.083(2)	0.042(2)	0.002(2)	-0.000(2)	0.002(2)
C1	0.042(1)	0.037(1)	0.034(1)	-0.007(1)	0.005(1)	-0.002(1)
C2	0.044(1)	0.045(2)	0.049(2)	-0.009(1)	0.011(1)	-0.001(1)
C3	0.043(2)	0.054(2)	0.053(2)	-0.011(1)	0.011(1)	0.000(2)
C4	0.048(2)	0.047(2)	0.047(2)	-0.022(1)	0.006(1)	0.003(1)
C5	0.050(2)	0.040(2)	0.040(2)	-0.012(1)	0.001(1)	0.002(1)
C6	0.045(1)	0.034(1)	0.029(1)	-0.007(1)	0.002(1)	0.001(1)
C7	0.042(1)	0.034(1)	0.046(2)	-0.002(1)	0.009(1)	-0.000(1)

Table of General Anisotropic Displacement Parameter Expressions - U's (Cc

Name	U(1,1)	U(2,2)	U(3,3)	U(1,2)	U(1,3)	U(2,3)
C8	0.043(1)	0.032(1)	0.040(1)	-0.004(1)	0.004(1)	0.000(1)
C9	0.047(2)	0.047(2)	0.050(2)	-0.011(1)	0.012(1)	0.006(1)
C10	0.053(2)	0.044(2)	0.059(2)	-0.014(1)	0.008(1)	0.008(2)
C11	0.061(2)	0.033(2)	0.070(2)	-0.009(2)	0.003(2)	0.002(2)
C12	0.053(2)	0.034(2)	0.064(2)	-0.002(1)	0.008(2)	-0.001(2)
C13	0.053(2)	0.035(2)	0.047(2)	-0.003(1)	0.003(1)	-0.003(1)
C14	0.049(2)	0.039(2)	0.042(2)	0.003(1)	0.001(1)	-0.005(1)
C15	0.051(2)	0.061(2)	0.046(2)	0.004(2)	0.011(1)	0.000(2)
C16	0.053(2)	0.077(2)	0.055(2)	0.017(2)	0.011(2)	-0.004(2)
C17	0.072(2)	0.067(2)	0.074(2)	0.023(2)	0.012(2)	-0.013(2)
C18	0.067(2)	0.047(2)	0.072(2)	0.013(2)	0.010(2)	-0.007(2)
C19	0.053(2)	0.036(1)	0.054(2)	-0.007(1)	0.001(1)	0.001(1)
C20	0.092(3)	0.095(3)	0.060(2)	-0.021(3)	-0.019(2)	-0.005(2)
C21	0.064(2)	0.042(2)	0.038(1)	0.010(1)	0.011(1)	-0.001(1)
C22	0.091(3)	0.087(3)	0.036(2)	0.014(2)	0.014(2)	-0.001(2)
C23	0.093(3)	0.106(3)	0.066(2)	0.008(3)	-0.011(2)	0.010(3)
C24	0.085(3)	0.158(5)	0.120(4)	0.039(3)	-0.009(3)	0.009(4)
C25	0.091(3)	0.093(3)	0.055(2)	0.012(3)	0.007(2)	0.012(2)
C26	0.155(5)	0.088(3)	0.098(3)	0.002(3)	0.018(3)	0.027(3)
C27	0.119(4)	0.091(3)	0.062(2)	-0.003(3)	-0.004(3)	-0.014(2)
C28	0.209(6)	0.084(3)	0.112(4)	-0.035(4)	-0.007(4)	-0.004(3)
C29	0.122(3)	0.104(3)	0.048(2)	-0.003(3)	0.017(2)	-0.007(2)
C30	0.119(4)	0.158(5)	0.087(3)	0.015(4)	0.039(2)	-0.016(3)
C31	0.097(3)	0.085(3)	0.092(3)	-0.009(3)	0.042(2)	0.005(2)

The form of the anisotropic displacement parameter is:
exp[-2PI2{h2a2U(1,1) + k2b2U(2,2) + l2c2U(3,3) + 2hkabU(1,2) + 2hlacU(1,3) + 2klbcU(2,3)}] where a,b, and c are reciprocal lattice constants.

Table V:

Table of Positional Parameters and Their Estimated Standard Deviations

Atom	x	y	z	B(A2)
H2	1.079	0.170	0.476	5.1
H5	0.953	0.407	0.487	4.4
H9	0.573	0.084	0.588	4.7
H10	0.572	-0.041	0.577	5.9
H11	0.707	-0.099	0.515	5.5
H12	0.850	-0.029	0.473	5.2
H15	0.483	0.242	0.592	5.4
H16	0.374	0.342	0.612	6.2
H17	0.437	0.458	0.592	6.8
H18	0.606	0.472	0.545	6.4
H20A	0.518	0.143	0.293	8.9
H20B	0.509	0.223	0.288	8.9
H20C	0.409	0.176	0.305	8.9
H22A	0.750	0.236	0.834	7.3
H22B	0.857	0.209	0.805	7.3
H22C	0.770	0.154	0.828	7.3
H23A	0.882	0.027	0.167	9.4
H23B	0.913	0.108	0.155	9.4
H24A	0.768	0.094	0.236	11.9

Table of Positional Parameters and Their Estimated Standard Deviations (cc

Atom	x	y	z	B(A2)
H24B	0.856	0.140	0.275	11.9
H24C	0.845	0.060	0.302	11.9
H25A	1.001	0.015	0.349	8.0
H25B	1.117	-0.009	0.330	8.0
H26A	1.000	-0.105	0.318	11.2
H26B	1.017	-0.091	0.228	11.2
H26C	0.906	-0.068	0.255	11.2
H27A	1.158	0.112	0.310	9.6
H27B	1.040	0.135	0.326	9.6
H28A	1.100	0.227	0.264	13.5
H28B	1.008	0.195	0.193	13.5
H28C	1.135	0.182	0.192	13.5
H29A	1.085	0.073	0.130	8.9
H29B	1.056	-0.008	0.144	8.9
H30A	1.250	0.000	0.152	11.7
H30B	1.228	-0.019	0.242	11.7
H30C	1.257	0.060	0.221	11.7
H31	0.494	0.135	0.736	10.3

H atoms are labelled according to the atom to which they are bonded.

Table VI: Table of Bond Distances in Angstroms

Atom 1	Atom 2	Distance	Atom 1	Atom 2	Distance
C2	H2	0.987(3)	C24	H24B	0.982(6)
C5	H5	0.964(4)	C24	H24C	0.990(6)
C9	H9	0.990(3)	C25	H25B	0.987(4)
C10	H10	0.977(3)	C25	H25A	0.978(5)
C11	H11	0.992(3)	C26	H26A	0.959(5)
C12	H12	0.987(4)	C26	H26B	0.981(6)
C15	H15	0.999(4)	C26	H26C	0.981(7)
C16	H16	0.973(4)	C27	H27B	0.978(5)
C17	H17	0.981(4)	C27	H27A	0.970(5)
C18	H18	0.980(4)	C28	H28A	0.969(6)
C20	H20A	0.913(5)	C28	H28B	0.972(7)
C20	H20B	0.978(5)	C28	H28C	0.975(7)
C20	H20C	0.967(5)	C29	H29B	0.952(5)
C22	H22A	0.971(4)	C29	H29A	0.993(5)
C22	H22B	0.986(4)	C30	H30A	1.006(6)
C22	H22C	0.969(4)	C30	H30B	0.983(6)
C23	H23A	0.966(5)	C30	H30C	0.999(6)
C23	H23B	0.991(5)	C31	H31	0.994(5)
C24	H24A	0.842(6)			

Numbers in parentheses are estimated standard deviations in the least significant digits.

Table VII: Table of Bond Angles in Degrees

Atom 1	Atom 2	Atom 3	Angle	Atom 1	Atom 2	Atom 3	Angle
C1	C2	H2	121.2(3)	H20B	C20	H20C	109.1(4)
C3	C2	H2	118.8(4)	C21	C22	H22A	115.7(3)
C4	C5	H5	119.9(4)	C21	C22	H22B	108.4(3)
C6	C5	H5	120.2(4)	C21	C22	H22C	109.2(3)
N3	C9	H9	118.7(3)	H22A	C22	H22B	106.9(4)
C10	C9	H9	119.4(3)	H22A	C22	H22C	108.3(4)
C9	C10	H10	119.6(3)	H22B	C22	H22C	108.2(4)
C11	C10	H10	120.8(3)	N5	C23	H23A	109.1(4)
C10	C11	H11	120.8(3)	N5	C23	H23B	107.8(4)
C12	C11	H11	120.0(3)	C24	C23	H23A	109.2(5)
C8	C12	H12	120.2(3)	C24	C23	H23B	107.7(5)
C11	C12	H12	121.6(4)	H23A	C23	H23B	108.0(5)
N4	C15	H15	118.7(3)	C23	C24	H24A	120.1(6)
C16	C15	H15	119.5(3)	C23	C24	H24B	110.6(5)
C15	C16	H16	121.0(4)	C23	C24	H24C	110.2(6)
C17	C16	H16	119.7(4)	H24A	C24	H24B	104.4(6)
C16	C17	H17	121.2(4)	H24A	C24	H24C	103.8(7)
C18	C17	H17	119.7(4)	H24B	C24	H24C	107.0(5)
C14	C18	H18	121.3(4)	N5	C25	H25B	109.1(4)
C17	C18	H18	120.1(4)	N5	C25	H25A	109.1(4)
C19	C20	H20A	110.8(4)	C26	C25	H25B	108.9(4)
C19	C20	H20B	110.8(4)	C26	C25	H25A	107.6(4)
C19	C20	H20C	111.4(5)	H25B	C25	H25A	107.4(4)
H20A	C20	H20B	106.9(5)	C25	C26	H26A	108.9(4)
H20A	C20	H20C	107.9(4)	C25	C26	H26B	112.1(5)

Table VII : Bond Angles (cont.)

Atom 1	Atom 2	Atom 3	Angle	Atom 1	Atom 2	Atom 3	Angle
C25	C26	H26C	112.5(5)	N5	C29	H29B	108.8(4)
H26A	C26	H26B	107.8(5)	N5	C29	H29A	106.4(4)
H26A	C26	H26C	107.8(6)	C30	C29	H29B	109.4(5)
H26B	C26	H26C	107.8(5)	C30	C29	H29A	107.6(5)
N5	C27	H27B	108.8(4)	H29B	C29	H29A	109.0(4)
N5	C27	H27A	109.7(4)	C29	C30	H30A	113.2(4)
C28	C27	H27B	106.5(5)	C29	C30	H30B	113.2(5)
C28	C27	H27A	108.8(5)	C29	C30	H30C	112.4(5)
H27B	C27	H27A	108.9(4)	H30A	C30	H30B	106.3(6)
C27	C28	H28A	106.1(6)	H30A	C30	H30C	105.2(5)
C27	C28	H28B	113.0(6)	H30B	C30	H30C	106.1(4)
C27	C28	H28C	111.4(5)	CL3	C31	H31	108.7(4)
H28A	C28	H28B	108.7(7)	CL4	C31	H31	107.3(3)
H28A	C28	H28C	108.5(7)	CL5	C31	H31	108.1(4)
H28B	C28	H28C	108.9(6)				

Numbers in parentheses are estimated standard deviations in the least significant digits.

Table VIII: Table of Least-Squares Planes

Orthonormal Equation of Plane 1

0.3338 X + -0.9410 Y + -0.0558 Z - -1.8937 = 0

0.0008 0.0003 0.0006 0.0072

Crystallographic Equation of Plane

4.1002 X + -17.7087 Y + -1.9499 Z - -1.8937 = 0

0.0098 0.0055 0.0891 0.0072

Atom	X	Y	Z	Distance	Esd
Fe	7.2041	4.0537	8.6901	-0.0012	+- 0.0004
O3	6.4721	3.8801	6.8753	0.0192	+- 0.0021
O4	4.4383	3.1682	7.3879	-0.0185	+- 0.0024
O5	7.5159	4.0661	10.6441	-0.0179	+- 0.0022
O6	5.5213	3.2892	11.1607	0.0185	+- 0.0027

Chi Squared = 268.4

----- Other Atoms -----

C19	5.2899	3.4786	6.5736	0.0192	+- 0.0031
C20	5.0108	3.4001	5.0995	0.0822	+- 0.0047
C21	6.6322	3.6777	11.4877	0.0055	+- 0.0031
C22	7.0290	3.7546	12.9364	-0.0153	+- 0.0042

Orthonormal Equation of Plane 2

-0.1913 X + -0.0134 Y + -0.9814 Z - -9.8101 = 0

0.0007 0.0009 0.0001 0.0069

Crystallographic Equation of Plane

-2.3494 X + -0.2517 Y + -15.2335 Z - -9.8101 = 0

0.0088 0.0164 0.0839 0.0069

Atom	X	Y	Z	Distance	Esd
N1	9.0855	3.3896	8.1749	0.0038	+- 0.0022
N2	8.2299	5.8129	8.3360	-0.0231	+- 0.0022
C1	10.0640	4.3658	7.9607	0.0137	+- 0.0027
C2	11.4062	4.1240	7.7228	-0.0062	+- 0.0030
C3	12.2846	5.1861	7.5423	-0.0113	+- 0.0032
C4	11.8256	6.4752	7.6068	-0.0041	+- 0.0030
C5	10.4839	6.7461	7.8437	0.0164	+- 0.0029
C6	9.5881	5.6981	8.0384	0.0108	+- 0.0026

Chi Squared = 205.3

Table of Least-Squares Planes (continued)

----- Other Atoms -----

Cl1	12.9014	7.8334	7.4591	-0.0831	+- 0.0010
CL2	13.9501	4.8058	7.2330	-0.0212	+- 0.0011

Orthonormal Equation of Plane 3

-0.3813 X + 0.1117 Y + -0.9177 Z - -10.5297 = 0

0.0009 0.0012 0.0005 0.0039

Crystallographic Equation of Plane

-4.6830 X + 2.1017 Y + -13.6079 Z - -10.5297 = 0

0.0116 0.0224 0.0967 0.0039

Atom	X	Y	Z	Distance	Esd
N3	7.0468	1.8563	8.7553	0.0157	+- 0.0023
C7	9.2970	2.0955	7.8934	-0.0245	+- 0.0029
C8	8.1128	1.2327	8.2379	0.0144	+- 0.0028
C9	5.9890	1.1147	9.1200	0.0015	+- 0.0031
C10	5.9803	-0.2573	8.9829	-0.0226	+- 0.0033
C11	7.0632	-0.8881	8.4308	0.0008	+- 0.0036
C12	8.1622	-0.1373	8.0502	0.0149	+- 0.0034

Chi Squared = 207.7

----- Other Atoms -----

O1	10.3017	1.5704	7.4169	-0.0289	+- 0.0025

Orthonormal Equation of Plane 4

-0.2999 X + -0.0474 Y + -0.9528 Z - -10.5389 = 0

0.0009 0.0014 0.0003 0.0087

Crystallographic Equation of Plane

-3.6838 X + -0.8920 Y + -14.4297 Z - -10.5389 = 0

0.0110 0.0265 0.0941 0.0087

Atom	X	Y	Z	Distance	Esd
N4	5.6919	5.6192	9.0061	-0.0154	+- 0.0023
C13	7.5788	6.9849	8.3169	0.0106	+- 0.0031
C14	6.1534	6.8595	8.7827	0.0002	+- 0.0030
C15	4.4191	5.4712	9.3946	0.0032	+- 0.0031
C16	3.5858	6.5561	9.5926	0.0129	+- 0.0034
C17	4.0715	7.8225	9.3963	-0.0057	+- 0.0039
C18	5.3781	7.9843	8.9772	-0.0059	+- 0.0038

Chi Squared = 74.5

Table of Least-Squares Planes (continued)

----- Other Atoms -----

O2	8.0051	8.0881	7.9859	0.1459	+- 0.0028

Orthonormal Equation of Plane 5

-0.2408 X + -0.0024 Y + -0.9706 Z - -10.0615 = 0

0.0006 0.0004 0.0001 0.0044

Crystallographic Equation of Plane

-2.9575 X + -0.0443 Y + -14.9026 Z - -10.0615 = 0

0.0071 0.0084 0.0756 0.0044

Atom	X	Y	Z	Distance	Esd
N1	9.0855	3.3896	8.1749	-0.0684	+- 0.0022
N2	8.2299	5.8129	8.3360	-0.0245	+- 0.0022
N3	7.0468	1.8563	8.7553	-0.1373	+- 0.0023
N4	5.6919	5.6192	9.0061	-0.0633	+- 0.0023
C1	10.0640	4.3658	7.9607	-0.0985	+- 0.0027
C6	9.5881	5.6981	8.0384	-0.0623	+- 0.0026
C7	9.2970	2.0955	7.8934	0.1570	+- 0.0029
C8	8.1128	1.2327	8.2379	0.1097	+- 0.0028
C13	7.5788	6.9849	8.3169	0.1481	+- 0.0031
C14	6.1534	6.8595	8.7827	0.0395	+- 0.0030

Chi Squared = 14121.4

----- Other Atoms -----

Fe	7.2041	4.0537	8.6901	-0.1170 +- 0.0004

Dihedral Angles Between Planes:

Plane No.	Plane No.	Dihedral Angle
1	2	89.80 +- 0.06
1	3	100.43 +- 0.08
1	4	90.13 +- 0.09
1	5	91.37 +- 0.05
2	3	13.57 +- 0.14
2	4	6.73 +- 0.20
2	5	2.97 +- 0.31
3	4	10.45 +- 0.22
3	5	10.82 +- 0.17
4	5	4.38 +- 0.31